

AD-A189 813

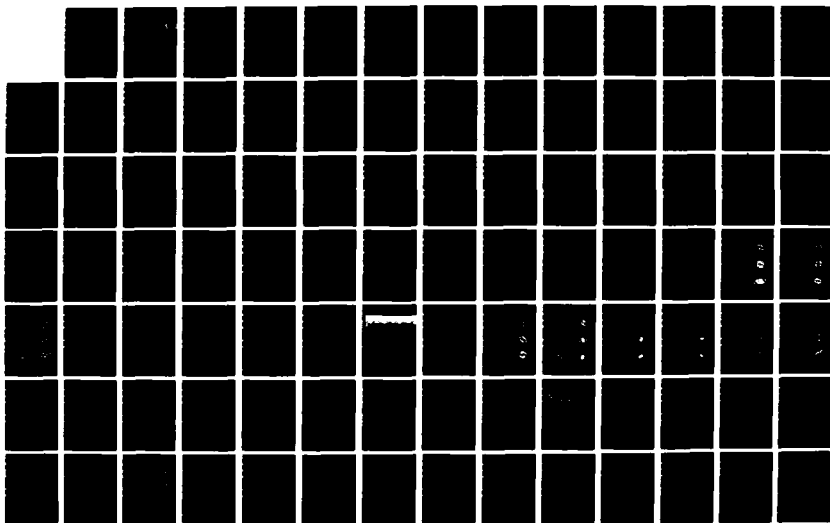
NUMERICAL SIMULATION OF TURBULENT FLAMES USING VORTEX
METHODS(U) MASSACHUSETTS INST OF TECH CAMBRIDGE
A F GHONIEM 05 OCT 87 AFOSR-TR-87-1853 AFOSR-84-0356

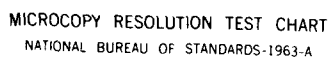
1/2

UNCLASSIFIED

F/G 21/2

NL





MICROCOPY RESOLUTION TEST CHART
NATIONAL BUREAU OF STANDARDS-1963-A

AD-A189 813

AFOSR-TR. 87-1853

THIRD ANNUAL REPORT
ON

DTIC FILE COPY

"NUMERICAL SIMULATION OF TURBULENT FLAMES USING VORTEX METHODS"

AFOSR Grant No. 84-0356

Principle Investigator:

Ahmed F. Ghoniem

Department of Mechanical Engineering
Massachusetts Institute of Technology
Cambridge, MA 02139

DTIC
ELECTE

JAN 07 1988

CH

SUMMARY

During the year of 1986-1987, we have developed the vortex element method and the transport element method, for the numerical simulation of the Navier-Stokes equations and the energy and species conservation equations, respectively. These methods are based on a Lagrangian, grid-free, time-accurate simulation of the governing equations at high Reynolds and Peclet numbers, without resorting to turbulence modelling. Finite-rate chemical reactions, finite compressibility and finite heat release rates are also considered in the formulations of the numerical schemes. To validate these methods, we are obtaining solutions for reacting shear layers, both homogeneous and heterogeneous, under various idealizations, and comparing the numerical results with experimental data. The solutions are also analyzed to investigate the mechanisms of turbulence-combustion interactions.

DISTRIBUTION STATEMENT A

Approved for public release;
Distribution Unlimited

Unclassified

SECURITY CLASSIFICATION OF THIS PAGE

REPORT DOCUMENTATION PAGE

Form Approved
OMB No. 0704-0188

1a. REPORT SECURITY CLASSIFICATION Unclassified			1b. RESTRICTIVE MARKINGS	
2a. SECURITY CLASSIFICATION AUTHORITY			3. DISTRIBUTION / AVAILABILITY OF REPORT Approved for public release; distribution is unlimited.	
2b. DECLASSIFICATION / DOWNGRADING SCHEDULE				
4. PERFORMING ORGANIZATION REPORT NUMBER(S)			5. MONITORING ORGANIZATION REPORT NUMBER(S) AFOSR-TR- 87-1853	
6a. NAME OF PERFORMING ORGANIZATION Massachusetts Institute of Tech.		6b. OFFICE SYMBOL (if applicable)	7a. NAME OF MONITORING ORGANIZATION AFOSR/NA	
6c. ADDRESS (City, State, and ZIP Code) 77 Massachusetts Ave. Cambridge, MA 02139			7b. ADDRESS (City, State, and ZIP Code) Building 410, Bolling AFB DC 20332-6448	
8a. NAME OF FUNDING / SPONSORING ORGANIZATION AFOSR/NA		8b. OFFICE SYMBOL (if applicable)	9. PROCUREMENT INSTRUMENT IDENTIFICATION NUMBER AFOSR 84-0356	
8c. ADDRESS (City, State, and ZIP Code) Building 410, Bolling AFB DC 20332-6448			10. SOURCE OF FUNDING NUMBERS	
			PROGRAM ELEMENT NO. PROJECT NO. TASK NO. WORK UNIT ACCESSION NO. 61102F 2308 A2	
11. TITLE (Include Security Classification) (U) "Numerical Simulation of Turbulent Flames Using Vortex Methods"				
12. PERSONAL AUTHOR(S) Ahmed F. Ghoniem				
13a. TYPE OF REPORT Annual Technical		13b. TIME COVERED FROM 9-1-86 TO 8-31-87	14. DATE OF REPORT (Year, Month, Day) 1987-10-5	15. PAGE COUNT 17+ four append
16. SUPPLEMENTARY NOTATION				
17. COSATI CODES			18. SUBJECT TERMS (Continue on reverse if necessary and identify by block number) Numerical Simulation, Turbulent Combustion, Vortex Methods	
FIELD	GROUP	SUB-GROUP		
19. ABSTRACT (Continue on reverse if necessary and identify by block number) During the year of 1986-1987, we have developed the vortex element method and the transport element method for the numerical simulation of the Navier-Stokes equations and the energy and species conservation equations, respectively. These methods are based on a Lagrangian, grid-free, time-accurate simulation of the governing equations at high Reynolds and Peclet numbers, without resorting to turbulence modelling. Finite-rate chemical reactions, finite compressibility and finite heat release rates are also considered in the formulations of the numerical schemes. To validate these methods, we are obtaining solutions for reacting shear layers, both homogeneous and heterogeneous, under various idealizations, and comparing the numerical results with experimental data. The solutions are also analyzed to investigate the mechanisms of turbulence-combustion interactions.				
20. DISTRIBUTION / AVAILABILITY OF ABSTRACT <input checked="" type="checkbox"/> UNCLASSIFIED/UNLIMITED <input checked="" type="checkbox"/> SAME AS RPT <input type="checkbox"/> DTIC USERS			21. ABSTRACT SECURITY CLASSIFICATION Unclassified	
22a. NAME OF RESPONSIBLE INDIVIDUAL Julian M Tishkoff			22b. TELEPHONE (Include Area Code) (202) 767-4935	22c. OFFICE SYMBOL AFOSR/NA

OBJECTIVES

The goal of this research program is to develop, test and apply methods of numerical simulation, based on vortex dynamics, to reacting flows with finite chemical reaction and heat release rates. In particular:

- I. The development of accurate and efficient numerical methods which can be utilized in the simulation of the time-dependent, multi-dimensional Navier-Stokes equations at high Reynolds number, and can be extended to solve the energy and species conservation equations in cases where the chemical reaction rates are finite and fast and when the associated heat release is large and hence dynamically important.
- II. The application of these numerical algorithms to turbulent reacting shear layers, for both homogeneous and heterogeneous reactants, to validate the numerical methods against experimental results, and to study the underlying mechanisms of entrainment and mixing and how they affect the rates of product formation.
- III. The investigation of the mechanisms of turbulence-combustion interactions based on rigorous fundamental models, and how these interactions can be manipulated to provide more efficient burning. In particular, the effect of turbulent fluctuations and flow stretch on the rate of chemical reaction, flame stability and extinction.



Accession For	
NTIS GRA&I	<input checked="" type="checkbox"/>
DTIC TAB	<input type="checkbox"/>
Unannounced	<input type="checkbox"/>
Justification	
By	
Distribution/	
Availability Codes	
Dist	Avail and/or Special
A-1	

PERSONNEL

Three graduate students have completed their master's theses under the sponsorship of this program. Their names and thesis titles are listed at the end of the report. Currently, five graduate students are continuing their doctorate work under the partial or full support of this project. Their names, listed according to seniority, are

- (1) Ghassem Heidarinejad
- (2) Omar Knio
- (3) Habib Najm
- (4) Anantha Krishnan
- (5) Luis-Fillipe Martins

EQUIPMENT

To meet the computational needs of this work, we have built the following system around a VAX 11/750:

- (1) An array processor MAP-6420.
- (2) Two MicroVAX II workstations, and a MicroVAX cpu.
- (3) A local area network with communication interface to a supercomputer.
- (4) Graphics terminals, a laser printer, and a color film recorder.

The system has been hard-wired into the Campus-wide network to allow easier access to other computational facilities available within and outside M.I.T., especially the John von Neumann supercomputer center at Princeton.

WORK STATUS

In the following, the vortex and transport element methods are briefly described and the results of their preliminary applications are discussed.

THE VORTEX ELEMENT METHOD

In this method, Lagrangian particles are treated as finite vortex elements that accurately discretize the vorticity field. We have shown that the accuracy of the method is governed by: the shape function of individual elements, the core radius and the distance between neighboring elements. To preserve the accuracy as the flow develops strong strain fields, particle distribution must change to accommodate distortions of the vorticity by the strain field, leading to a natural growth in the number of vortex elements with time as the flow develops stronger gradients, or fine scales, via stretch. We are implementing a new algorithm to limit the number of interactions between N vortex elements to $O(N)$, instead of $O(N^2)$ in direct interactions, using multipole expansion of the contribution of groups of elements.

In Appendix I, the scheme is described in detail, and results for the evolution of a temporal shear layer are analyzed. A temporal shear layer model allows one to limit the computations to a fixed number of large eddies as they evolve from a perturbation to a coherent vortex structure. The accuracy of the computations reveals the detail of the inner structure of the large eddies and the development of secondary instabilities which force the core into several rotations, as well as the severe strain which material line are exposed to within the eddy core. The application of the scheme to a spatially developing shear layer is presented in Appendix II. The improvement of the accuracy over schemes which utilize a fixed number of elements can be realized by comparing these results with results shown in

Appendix III. In the vortex element method, the number of elements grows as the strain field develops, letting one capture the areas where the strain field, and thus the large scalar gradients develop.

Extension of the vortex element method to three dimensional flow simulation has been accomplished by utilizing spherical vortex elements that discretize a three dimensional vorticity field and undergo stretching along the direction of the vorticity vector, as described in Appendix IV. The application of the scheme to study the evolution of azimuthal instabilities on vortex rings has shown that these structures are unstable to a particular wave number, causing the ring to develop into a star-like structure with lobes of vorticity extending in the radial direction of the ring. Results also show that these azimuthal instabilities can excite higher frequency modes by vortex stretching, generating a turbulent cascade of the energy into higher wave numbers. Results of the simulation compared favorably with experimental data. The computations are currently being extended to simulate the evolution of streamwise vorticity in a planar shear layer and a turbulent jet.

THE TRANSPORT ELEMENT METHOD

To achieve an efficient, self-adaptive Lagrangian algorithm for the solution of the energy and species conservation equations, scalar gradients are discretized using core functions similar to those used in the vortex element method. However, contrary to the scalar concentration, gradients are not conserved along a particle path since stretching and tilting material layers enhance the gradients and change their direction. This effect is implemented by changing the strength of the transport elements according to the variations of a small material line that coincides with the center of the transport element. Adding a chemical source term requires

changing the local gradients with time. This amounts to transporting several scalar gradients with each element and integrating the source term within each element to compute its instantaneous strength according to a given chemical kinetics scheme. At low Mach number, volumetric expansion due to heat release produces an irrotational velocity field, and generates non-baroclinic vorticity due to the interaction between the density and pressure gradients.

In Appendices I and II, the mathematical formulations of the transport element method are described for a non reacting flow and a for reacting flow, respectively. In Appendix I, the method has been applied to compute the temperature profiles in an initially-thermally stratified temporal mixing layer, showing how entrainment leads to intermittency within the eddy core and to mixing enhancement by generating large gradients as the material layers stretch. Statistics of mixing of a passive scalar in a spatial shear layer have been compared with experimental results in Appendix III, where only a simplified version of the scheme, the scalar element method, was used. The comparison is favorable, considering the fact that no turbulence modeling was implemented to obtain these results. The accuracy of the computations falls off around the boundaries of the layer due to the small number of scalar elements which were used in this simulation. The transport element method avoids this problem by transporting the gradients, instead of the scalar, and is expected to yield better predictions for the mixing statistics. This is currently being tested.

Results for the development of an eddy in a reacting shear layer are presented in Appendix II. Initially, reactants and products are on the top and bottom sides, respectively. As the eddy grows by entraining more reactants, the flame is stretched and wrinkled, leading to a rise in the

rate of product formation over that of the corresponding laminar flame. The ratio of the total amount of products formed in the two cases scales with the square of the flame length in the turbulent case.

To validate these results, computations will be performed for a spatially developing, reacting mixing layer, and statistical information derived from the simulations will be compared with experimental measurements.

TURBULENCE-COMBUSTION INTERACTIONS

Slowing down the rate of chemical reaction in the reacting mixing layer leads to local and temporary extinction, as shown in Appendix II. As the Damkohler number of the reacting mixture is lowered, the rate of product formation is decreased. Moreover, the reaction is observed to cease completely for short periods of time. The lower the Damkohler number, the earlier the reaction is temporarily extinct. Local extinction is observed around areas of largest strain field. The extinction occurs temporarily since on the other side of the layer, products at high temperature heat up the reactants and resume the reaction after a short pause. To explain why extinction is correlated with the strain field, we inspected plots of the temperature, strain rate and expansion rate along one of the layers within the flame zone. It was found that a negative correlation existed between the strain rate and expansion rate, and between the temperature and strain rate. Thus, it was concluded that as the strain lowered the temperature by enhancing the diffusion flux via strong gradients, it led to flame extinction. The temperature drop was due to the fact that chemistry was slow so that it could not make up for the increase in the diffusion fluxes with stretch.

Other parameters, e.g., the Peclet number, Lewis number and the activation energy, can affect the interaction between turbulence and combustion. Work is underway to investigate their influence on the mechanism described above.

THESES PRODUCED DURING 1984-1987:

- (1) Ng, Kenneth K., "Vortex Simulation of a Confined and Perturbed Shear Layer," M. Sc., January 1986.
- (2) Gagnon, Yves, "Numerical Investigation of Recirculating Flow at Moderate Reynolds Numbers Using Vortex Methods," M. Sc., January 1986.
- (3) Knio, Omar, "Low Mach Number Simulation of Combustion in Closed Chambers," M. Sc., January 1986.

PAPERS PUBLISHED DURING 1984-1987:

- (1) Ghoniem, A.F. and Sethian, J.A., "Dynamics of recirculation in a turbulent flow; A computational investigation," AIAA-85-0146. The AIAA 23rd Aerospace Sciences Meeting, Reno, Nevada, 1985.
- (2) Ghoniem, A.F., and Sethian, J.A., "Effect of Reynolds number on the structure of recirculating flows," AIAA Journal, 25, pp. 168-171, 1987.
- (3) Ghoniem, A.F., "Analysis of flame deformation in a turbulent field; effect of Reynolds number on the burning rate," AIAA-85-0140. The AIAA 23rd Aerospace Sciences Meeting, Reno, Nevada, 1985.
- (4) Ghoniem, A.F., "Effect of large scale structures on turbulent flame propagation," Combust. Flame, 64, pp. 321-336, 1986.
- (5) Ghoniem, A.F., "Computational methods in turbulent reacting flows," Invited three lecture series at The Seventh AMS-SIAM Summer Seminar in Applied Mathematics on Combustion and Chemical Reactors, Cornell University, July 1985. Lectures in Applied Mathematics, 24, pp. 199-265, 1986.
- (6) Ng, K.K., and Ghoniem, A.F., "Numerical simulation of a confined shear layer," The 10th International Colloquium on the Dynamics of Explosions and Reactive Systems, August 4-9, 1985, Berkeley, CA. Dynamics of Reactive Systems, Part II, ed. by Bowen et al., pp. 18-49, 1986.
- (7) Ghoniem, A.F. and Gagnon, Y., "Numerical investigation of recirculating flow at moderate Reynolds numbers" AIAA-86-0370. The AIAA 24th Aerospace Sciences Meeting, Reno, Nevada, January 1986.
- (8) Ghoniem, A.F., and Gagnon, Y. "Vortex simulation of laminar recirculating flow," J. Comput. Phys., 68, pp. 346-377, 1987.
- (9) Ghoniem, A.F., and Ng, K.K. "Effect of harmonic modulation on rates of entrainment in a confined shear layer," AIAA-86-0056. The AIAA 24th Aerospace Sciences Meeting, Reno, Nevada, January 1986.
- (10) Ghoniem, A.F., and Ng, K.K., "Numerical study of a forced shear layer," Phys. Fluids, 30, pp. 706-721, 1987.
- (11) Ghoniem, A.F., and Knio, O.M., "Numerical Simulation of Flame Propagation in Constant Volume Chambers," Presented at The 21st

Symposium (International) on Combustion, Munich, West Germany, August 1986. Proceedings to be published.

- (13) Sethian, J.A., and Ghoniem, A.F., "Validation of the vortex method," accepted for publication at J. Comput. Phys., 1987.
- (14) Ghoniem, A.F., Knio, O.M., and Aly, H.F., "Three dimensional vortex simulation with application to axisymmetric shear layers," AIAA-87-0379, the 25th Aerospace Sciences Meeting, Reno, Nevada, January 1987.
- (15) Givi, P. and Ghoniem, A.F., "Vortex Scalar-element calculations of a diffusion flame," for AIAA-87-0225, the 25th Aerospace Sciences Meeting, Reno, Nevada, January 1987, submitted for publication at the AIAA Journal.
- (16) Ghoniem, A.F., Heidarinejad, G., and Krishnan, A. "Numerical simulation of a thermally stratified shear layer using the vortex element method," submitted for publication, J. Comput. Phys. (1987).
- (17) Ghoniem, A.F., "Vortex methods for non-reacting and reacting flows," Workshop on Vortex Methods, University of California, Los Angeles, May 20-22, 1987, Proceedings to appear, January 1988.
- (18) Ghoniem, A.F., "Turbulence-Combustion interactions in a reacting shear layer," United States-France Joint Workshop on Turbulent Reactive Flows, July 6-10, 1987, Rouen, France, Proceedings to appear, January 1988.
- (19) Ghoniem, A.F., Heidarinejad, G., and Krishnan, A., "Numerical simulation of a reacting shear layer using the transport element method," The 23rd AIAA/SAE/ASME/ASEE Joint Propulsion Meeting, La Jolla, California, June 29-July 1, 1987, AIAA-87-1718.
- (20) Najm, H. and Ghoniem, A.F., "Vortex simulation of the convective instability in a dump," The 23rd AIAA/SAE/ASME/ASEE Joint Propulsion Meeting, La Jolla, California, June 29-July 1, 1987, AIAA-87-1874.

PRESENTATIONS DURING 1984-1987:

1. "Development and Applications of Vortex Methods: Aerodynamics and Combustion," NASA Lewis Research Center, Cleveland, Ohio, June 1984.
2. "Simulation of a Turbulent Flow in a Model Combustor," 1984 Technical Meeting, Eastern Section of the Combustion Institute, Clearwater Beach, FA, December 1984.
3. "Flame propagation and stability in engine chambers," Department of Energy sponsored program on "Lean Engine Efficiency," Ford Motor Company, May 1985.
4. "Numerical solution of a confined shear layer using vortex methods," The International Symposium on Computational Fluid Dynamics, Tokyo, Japan, September 1985.

5. "Vortex Simulation of Turbulent Reacting Flow," AFSOR/ONR Contractors Meeting on Turbulent Combustion, July 1985.
6. Ng, K. K. and Ghoniem, A. F., "Harmonic modulation of a confined shear layer," 1985 Technical Meeting of the Eastern Section of the Combustion Institute, Philadelphia, PA, November 1985.
7. Ghoniem, A. F. and Ng, K. K. "Numerical solution of a confined shear layer using vortex methods," The International Symposium on Computational Fluid Dynamics, Tokyo, Japan, September 1985.
8. "Application of Computational Methods in Turbulent Reacting Flow," University of North Carolina, October 1985.
8. "Vortex Simulation of Reacting Shear Flows," Army Research Office, Durham, North Carolina, October 1985.
9. The Pennsylvania State University, "Vortex Simulation of Reacting Shear Flow," November 1985.
10. Princeton University, "Vortex Simulation of Reacting Shear Flow," December 1985.
11. University of California, Berkeley, "Computing Unsteady Flow Using Vortex Methods," January 1986.
12. Department of Energy Meeting on Homogeneous Charge Engines, University of California, Berkeley, April 1986.
13. Fourth Army Conference on Applied Mathematics and Computing, Cornell University, "Computing Unsteady Reacting Flow Using Vortex Methods," May 1986.
14. SIAM National Meeting, Boston, MA, July 1986, "Computational Methods in Combustion Theory".
15. Workshop on Computational Fluid Dynamics and Turbulent Reacting Flows, Institute of Mathematics and its Application, University of Minnesota, September 1986. "Vortex Simulation of Turbulent Reacting Flow".
16. Ghoniem, A. F. and Najm, H., "Numerical study of combustion instability in a dump configuration," 1986 Fall Technical Meeting, Combustion Institute, December 15-17, 1986, San Juan, Puerto Rico.
18. Flow Research Laboratories, Kent, WA, Vortex Simulation of Turbulent Shear Flow, June 1986.
19. SIAM 1986 National Meeting, Boston, MA, Computational Methods in Combustion Theory, July 1986.
20. Workshop on Computational Fluid Dynamics and Turbulent Reacting Flows, Institute for Mathematics and its Applications, University of Minnesota, Vortex Methods in Turbulent Reacting Flows, September 1986.

21. General Motors Research Laboratory, Warren, MI, Application of Vortex Method to Turbulent Reacting Flow, November 1986.
22. University of Notre Dame, G.E. Scholar Lectureship, Vortex Simulation of Turbulent Reacting Flow, November 1986.
23. National Bureau of Standards, Gaithersburg, MD, Vortex Simulation of Turbulent Reacting Flow, February 1987.
24. SIAM Meeting on Numerical Combustion, San Francisco, CA, Lagrangian Gradient Methods in Turbulent Reacting Flow, March 1987.
25. University of Maryland, Vortex simulation of turbulent reacting flow, April 1987.
26. Workshop on Vortex Methods, Los Angeles, CA, Vortex Simulation of Turbulent Shear Flows, May 1987.
27. United States-France Joint Workshop on Turbulent Reactive Flow, Rouen, France, Turbulence-Combustion Interactions in a Reacting Shear Layer, July 1987.
28. Peugeot Motor Company, Paris, France, Recent Progress of Numerical Simulation of Turbulent Reacting Flows, July 1987.

INTERACTIONS DURING 1984-1987

1. Participated in DOD meeting on Topical Review on Mechanics, Aeronautics and Propulsion, National Academy of Sciences, February 5-6, 1985.
2. NASA Lewis Research Center, Combustion Fundamentals (Dr. C. John Marek) and Computational Fluid Mechanics (Dr. John Adamczyk), June 1984.
3. California Institute of Technology, Combustion Laboratory of Prof. E. Zukoski, to explore their experimental work on pressure oscillations in dump combustors and couple to our numerical studies, July 1985.
4. Army Research Office, Mathematical Sciences Division (Dr. J. Chandra) (to visit the Laboratory on October 4, 1985, and explore avenues for interactions).
5. Pennsylvania State University, Combustion Laboratory of Dr. Dominic Santavicca, to couple his experimental investigation on the effect of turbulence on flame propagation (supported by AFOSR) to our numerical simulation activities (to visit the Laboratory on November 6th).
6. Sandia National Laboratory, couple experimental work on flame structure (Dr. R. Green) and engine efficiency (Dr. F. Dyer) with our numerical simulation studies.
7. Columbia University, N.Y., Combustion Laboratory of Drs. R. Bill and R. Chevery, to couple their experimental work on stability of V-shaped

flames and axisymmetric shear layers to our numerical simulations (to visit during this academic year, 1985-1986).

8. AFWAL Aeropropulsion Laboratory, Wright-Patterson AFB, OH, Dr. W.M. Roquemore, structure of turbulent jet flames.

Appendix I

The paper on "Numerical simulation of a thermally stratified shear layer using the vortex element method" describes formulation the vortex element method and the transport element method for a non-reacting flow. Results for the application of the methods to a non-reacting, thermally stratified temporal shear layer are presented.

Submitted for publication at
the Journal of Computational Physics

August 1987

NUMERICAL SIMULATION OF A THERMALLY STRATIFIED SHEAR LAYER
USING THE VORTEX ELEMENT METHOD

Ahmed F. Ghoniem, Ghassem Heidarinejad, and Anantha Krishnan

Department of Mechanical Engineering
Massachusetts Institute of Technology
Cambridge, MA 02139

ABSTRACT

In computing the development of an unstable inviscid shear layer, it is found that using a fixed number of vortex elements can lead to large errors due to the strong strain field which develops and acts to distort the original vorticity contours. It is suggested that the vorticity should be redistributed among elements which are arranged in the local principal direction of strain in order to capture this distortion accurately. Mixing within an initially stratified layer, which results from the combined action of convection and diffusion, is computed using a similar scheme to integrate the energy equation. Calculations illustrate the evolution of the temperature profile during the growth of the instability.

I INTRODUCTION

I.1. BACKGROUND

Numerical simulation of inviscid two-dimensional incompressible flow using vortex discretization of the Euler equations has been discussed extensively in recent literature (Leonard [1], Beale and Majda [2], Hald [3] and Ghoniem and Ng [4]). The method is based on distributing the vorticity field among elements which carry radially-symmetric, compact supports of vorticity (Chorin [5]). By choosing the extent of the support, or the core radius of each element to be larger than the distance of separation between neighboring elements, the fields of individual elements overlap and high order discretization of the vorticity field can be achieved. Vortex elements move with the local flow velocity evaluated at their geometrical centers, which is computed as the summation over the contributions of all elements that exist in the field. The motion of a vortex element does not change its circulation and, in most applications, vortex elements possess invariable core shape and size.

The attraction of these Lagrangian, grid-free methods is that, by construction, computational vortex elements are expected to be, at all times, concentrated around zones of high velocity gradients. When properly exploited, this property endows the scheme with the resolution necessary to study interesting phenomena that arise when molecular diffusion is small relative to convective transport. For instance, at high Reynolds numbers, vorticity exists on small patches of the fluid and it suffices to distribute computational elements within these patches and hence avoid wasting labor on zones of very small vorticity. That the elements move to capture large velocity gradients is particularly important in unsteady and nonlinearly unstable flows where the evolution of the instability causes a substantial

distortion of the vorticity distribution. Moreover, using a Lagrangian formulation of the equations of motion avoids the convective non-linearity and enables the construction of computational schemes which are explicit in time. The employment of moving Lagrangian grids (Fritts and Boris [6]), or grid-free schemes such as contour dynamics (Zabuski et al. [7]), are other successful ways of accomplishing the same goal.

1.2. BRIEF REVIEW

Analysis of the convergence of inviscid vortex methods shows that three factors govern their accuracy: (1) the scheme of discretization of the initial vorticity; (2) the form of the core function; and (3) the ratio of the core radius to the separation between vortex elements (Chorin et al. [8], Del-Prete and Hald [9], Hald [3,10], and Beale and Majda [2,11,12].) Results of these analyses have been supported by numerical tests (Nakamura et al. [13], Roberts [14], and Perlman [15]). In the following, all three factors are briefly discussed.

To initialize the strength of vortex elements, Del-Prete and Hald [9] used the average vorticity within an area element around the center of the element, while Beale and Majda [2] suggested using the vorticity at the center of the element. Nakamura et al. [13] minimized the global error between the continuous and the discrete vorticity distribution to evaluate the latter. Anderson and Greengard [16] proposed the use of a non uniform mesh to discretize the vorticity field. Using the procedure in [2] or [9], one should expect almost a second-order accuracy for short time if the core function is chosen to be a second order Gaussian. A fourth order Gaussian was shown to improve the accuracy. In both cases, a critical parameter is the ratio of the core radius to the distance of separation between the

centers of the elements, which must be chosen larger than unity to preserve the accuracy for long time.

As the elements move, their separation exceeds their initial value if strong strain field arises. This, in effect, decreases the critical ratio of core/separation, leading to a deterioration of the accuracy. The fact that large strains cause deterioration in the accuracy of vortex methods has been observed explicitly in analysis, e.g., Leonard [1]. Thus, for most inviscid vortex methods, which are based on using a fixed number of vortex elements with invariant cores, the evolution of large local strains can lead to large errors. For example, a circular patch of vorticity may deform into an elliptical shape with its major axis aligned with the principal direction of strain. If a small fixed number of computational elements is used, they may not be able to accommodate these severe changes. Anderson [17] and Krasny [18], when discretizing non-smooth vorticity, employed a very large core radius so that as vortex elements moved away from each other due to stretch, reasonable overlap could still be maintained to satisfy the requirements for accuracy. One may also be forced to consider schemes of redistributing the vorticity among a different set of elements under conditions of large strain. Similar schemes have been used in methods of contour dynamics to preserve the accuracy of the integration around the vorticity contours (Zabuski and Overman [19].) Krasny [20], in an independent effort, used a similar procedure in simulating the evolution of a vortex sheet by a desingularized Biot-Savart integral.

Extension of Lagrangian element methods to integrate a scalar conservation equation has been applied to several problems in one dimension (Chorin [21], Ghoniem and Oppenheim [22,23] and Ghoniem and Sherman [24].) These schemes were based on using the scalar gradient, in analogy to

vorticity, in the transport process. Anderson [16,25] constructed a scheme to solve for a two dimensional thermal in the inviscid Boussinesq approximation by discretizing the density equation in its vortex form. This was done by casting the equation in gradient form and discretizing the density gradients among elements that could be transported. This scheme, while preserving the advantages of the vortex method, suffers from a major problem: A large strain field, while it may lead to the generation of large gradients, depletes the area of computational elements which are used to transport these gradients.

1.3. ORGANIZATION

In this paper, we apply the inviscid vortex methods to the problem of a temporal shear layer at high Reynolds number. This problem is characterized by a well-defined smooth vorticity field at time zero, and has well-documented stability properties. At later times, the shear layer develops into a complicated structure which resembles a turbulent eddy, and a very strong strain field is generated around this eddy. We use the analytical solution of a temporal shear layer to measure the accuracy of the results at the initial stages of development, and test the schemes for initializing the vortex elements. At longer times, we observe the effect of the strain field on the accuracy of the computations and suggest ways to cope with it. We then proceed to compute the temperature field as fluids with different temperatures are entrained, stretched and mixed.

In Section II, the formulation of the vortex method is described, and is extended to solve for a flow with a strong strain field. The scheme is applied to compute the evolution of a vorticity layer subject to periodic boundary conditions. The growth of the instability and its effects on the flow field are investigated. In Section III, the concepts of the vortex

method are generalized to solve the energy equation and to obtain the temperature profile across the shear layer during its development. The paper ends with conclusions in Section IV.

II INVISCID INCOMPRESSIBLE FLOW

II.1. THE VORTEX METHOD

For an inviscid incompressible flow, the vortex transport equation is:

$$\frac{\partial \omega}{\partial t} + \mathbf{u} \cdot \nabla \omega = 0 \quad (1)$$

$$\Delta \psi = -\omega \quad (2)$$

where $\mathbf{u} = (u, v)$ is the velocity, $\omega = \nabla \times \mathbf{u}$ is the vorticity, $\mathbf{x} = (x, y)$ are the streamwise and cross stream directions, respectively, t is time, $\nabla = (\partial/\partial x, \partial/\partial y)$ and $\Delta = \nabla \cdot \nabla$. Variables are normalized with respect to the appropriate combination of a characteristic velocity and length scale. ψ is the stream function defined so that $u = \partial\psi/\partial y$ and $v = -\partial\psi/\partial x$. The solution of Eq. (1) can be written as:

$$\omega(\chi(\mathbf{X}, t), t) = \omega(\mathbf{X}, 0) \quad (3)$$

while χ is governed by:

$$\frac{d\chi}{dt} = \mathbf{u}(\chi(\mathbf{X}, t), t) \quad (4)$$

where $\chi(\mathbf{X}, 0) = \mathbf{X}$. In the vortex method, the vorticity field $\omega(\mathbf{X}, 0)$ is discretized between elements centered at X_i , $i=1, \dots, N$, so that:

$$\omega(\mathbf{x}, 0) = \sum_{i=1}^N \Gamma_i f_\delta(\mathbf{x} - \mathbf{X}_i) \quad (5)$$

where $\Gamma_i = \omega_i h^2$ is the circulation of an element of strength ω_i and f_δ is the core function. $f_\delta(\mathbf{x}) = 1/\delta^2 f(r/\delta)$, where $r^2 = x^2 + y^2$, and $\int f_\delta d\mathbf{x} = 1$. δ is the core radius, and f_δ is a fast decaying function so that most of the vorticity is concentrated within $r < \delta$. To approximate the initial vorticity distribution accurately, δ should be greater than h , where h is

the initial separation between vortex centers. The core function f plays a similar role as interpolating polynomials in finite-difference schemes and base functions in finite-element formulations. By requiring f to be radially symmetric, the approximation in Eq. (5) is at least second order.

Using Eq. (3) and the incompressibility condition, the vorticity distribution at any time is given by

$$\omega(\mathbf{x}, t) = \sum_{i=1}^N \Gamma_i f_{\delta}(\mathbf{x} - \mathbf{X}_i) \quad (6)$$

where $d\mathbf{X}_i/dt = \mathbf{u}(\mathbf{X}_i, t)$ and $\mathbf{X}_i(\mathbf{X}_i, 0) = \mathbf{X}_i$.

The stream function of a single vortex element is obtained by integrating Eq. (2). Using polar coordinates, for a vortex element placed at $\mathbf{x}=0$, $\partial\psi_{\delta}/\partial r = -\kappa(r/\delta)/r$, where $\kappa(r) = \int_0^r r' f(r') dr'$. Moreover, $u_{\theta} = -\partial\psi_{\delta}/\partial r$. The velocity field induced by a distribution of vortex elements, of shape f_{δ} and strength Γ_i located at $\mathbf{X}_i(\mathbf{X}_i, t)$ is:

$$\mathbf{u}_{\omega}(\mathbf{x}, t) = \sum_{i=1}^N \Gamma_i \mathbf{K}_{\delta}(\mathbf{x} - \mathbf{X}_i) \quad (7)$$

$$\text{where } \mathbf{K}_{\delta}(\mathbf{x}) = - \frac{(\mathbf{y}, -\mathbf{x})}{r^2} \kappa\left(\frac{r}{\delta}\right) \quad (8)$$

Vortex elements move without changing their circulation (strength) or core shape, at a velocity computed from Eq. (7).

In the calculations, we used mostly a second order Gaussian core:

$$f = \frac{1}{\pi} e^{-r^2}$$

$$\kappa = \frac{1}{2\pi} (1 - e^{-r^2}) \quad (9)$$

When applying the vortex scheme to a flow field with boundary conditions other than $u(\infty, t) = 0$, a potential flow is added to satisfy these conditions. In this work, we perform computations for a periodic shear layer. The velocity field induced by vorticity outside the computational domain $0 < x < \lambda$, where λ is the longest wavelength of the perturbation, must be added to u_ω . The total velocity is:

$$u = \sum_{i=1}^N \frac{\Gamma_i}{2\pi} \left[\sum_{j=0}^{\pm 1} \frac{(y, -(x+j\lambda))}{((x+j\lambda)^2 + y^2)} \exp\left(-\frac{((x+j\lambda)^2 + y^2)}{\delta^2}\right) + \frac{\pi}{\lambda} \frac{(-\sinh(2\pi y/\lambda), \sin(2\pi x/\lambda))}{(\cosh(2\pi y/\lambda) - \cos(2\pi x/\lambda))} \right] \quad (10)$$

where N is the total number of vortex elements in the computational domain $0 < x < \lambda$. Note that since $\delta \ll \lambda$, the effect of the core was included only for the nearest sister vortices.

The initial vorticity distribution across the shear layer can be well represented by a Gaussian curve (which should not be confused with the Gaussian core of individual vortex elements) with a spread 2σ :

$$\Omega(x) = \frac{\Delta U}{\sqrt{\lambda}\sigma} \exp(-y^2/\sigma^2) \quad (11a)$$

where ΔU is the velocity difference across the layer and σ is the standard deviation of the Gaussian. The corresponding velocity distribution is:

$$U(x) = \frac{\Delta U}{2} \operatorname{erf}(y/\sigma) \quad (11b)$$

where $\operatorname{erf}(x) = 2/\sqrt{\pi} \int_0^x \exp(-r^2) dr$ is the error function. We take ΔU and σ as the characteristic velocity and length scales of the problem, respectively.

As it was pointed out in the Introduction, using either a pointwise discretization, $\omega_i = \Omega(X_i)$, or an area average value $\omega_i = \int_{h \times h} \Omega(X) dX$, where X_i , $i=1,2, \dots, N$ are the centers of a square mesh of side h , to discretize the vorticity of the shear layer among vortex elements produced a large error in the initial growth of the perturbation. Instead, the following scheme was used:

$$\Omega(X_i) = \sum_{j=1}^N \omega_j h^2 f_\delta(X_i - X_j) \quad (12)$$

for $i=1,2,\dots,N$. The error associated with this distribution was used as a measure of the accuracy of the initial discretization. In all cases, the error $|e_\omega| = \int |\Omega(X) - \omega(X,0)| dX < 10^{-5}$. The error e_ω increased rapidly as δ/h was decreased below one, which is consistent with the result of the convergence theory which shows that the overlap between neighboring elements is necessary for accurate discretization of vorticity. For $\delta/h > 1$, the error was less sensitive to its exact value, upto $\delta/h = 1.5$. In the following calculations, we used $\delta/h = 1.1 - 1.4$.

To measure the effect of the accuracy of the initial discretization of vorticity among vortex elements on the flow field for short times, we will use the rate of growth of the perturbation. The growth of the initial perturbation can be characterized by an integral parameter I as:

$$I = \int_0^\lambda \int_{-\infty}^\infty |u(x,t) - U(x)| dx \quad (13)$$

which is used in the linear theory analysis of the perturbation.

At $t = 0$, the layer was perturbed by a sinewave with amplitude ϵ , taken as 0.001λ , 0.01λ , and 0.1λ . In Fig. 1, we compare the growth of the perturbation with the prediction of the linear theory of stability (Michalke

[26].) to assess the accuracy of the vortex method for short times. For most of the computations, $\lambda = \lambda^* = 13.2 \sigma$, which corresponds to the wave with the maximum growth rate. Eq. (4) is integrated using a second order Heun's method with $\Delta t = 0.1$, and $h = \lambda / 44 = 0.3$, and $N(0) = 572$ vortex elements. The figure indicates that for $\epsilon = 0.01$ and 0.001 , the layer behaves linearly and the computed growth rate $\dot{I} = d \ln I / dt = 0.215$ agrees well with the results of the linear theory, $\dot{I} = 0.22$. The latter was computed as the eigenvalue of the linearized Euler equations (Betchov and Criminale [27].) Using $h = \lambda / 24$, i.e. $N(0) = 168$, and a second order time integration scheme, $\dot{I} = 0.23$. For $N(0) = 572$ and a first order time integration, $\dot{I} = 0.24$. Within this linear stage of development, the maximum distance between neighboring element in the direction of maximum strain $\Delta x < 1.5 h$, i.e the flow is developing mild stretch. For $\epsilon = 0.1$, the perturbation leads directly to the nonlinear range.

In Figs. 2, 3 and 4, the vortex elements and their velocity vectors are plotted for $\epsilon = 0.001 \lambda$, 0.01λ , and 0.1λ , respectively. In the first two cases, the end of the linear range corresponds to the beginning of the rollup of the interface, defined here as the line which coincides with $y = 0$ at $t = 0$, and the formation of a spiral center at the midpoint of the wavelength. Concomitantly, the interface starts to stretch near the boundaries of the domain and two saddle points are established at the beginning and end of the wavelength, $x = 0$, and λ . Beyond the linear range, the perturbation continues to grow with more layers rolling around the spiral center and stretching near the saddles. Within this nonlinear range of development, special care must be exercised or the numerical accuracy deteriorates quickly, as exhibited by the evolution of irregular motion near the saddles and the loss of organization of the evolving structure.

II.2. EFFECT OF STRETCH

The loss of organization, which is associated with the development of strong stretch, illustrates one of the fundamental problems of the vortex method. Vortex elements, which start as cores with radial symmetry, may not properly represent the vorticity field after it has developed strong local strains. As the effective distance, ΔX , between neighboring elements increases, the ratio $\delta/\Delta X$ (equivalent to δ/h) reaches levels where the vorticity discretization becomes inaccurate. One obvious remedy is to restart the calculations with smaller values of h to allow a larger number of weaker elements to represent the strong distortion. However, that only delays the onset of the crisis at the expense of using more elements at the initial stages when they are not needed. Several remedies may be suggested: (1) utilizing deformable cores; (2) employing large cores; or (3) using more elements as the distance between the original elements increases.

The first scheme, utilizing deformable cores, depends on assuming that the core structure will become elliptical as stretch develops, with the major axis of each element aligned with the local principal direction of strain. The vorticity distribution within the core must also adapt to the geometrical boundaries of the cores. If elements with constant vorticity within the cores and zero outside, i.e. Rankine vortex elements, are used then these elements will become Kirkchoff vortices which have analytical expressions for the induced velocity field. However, there is an obvious limitation on maintaining one ellipse as a single element if the ratio between its axes exceeds a reasonable value. Thus, this scheme is discarded.

The second scheme, in which one uses large cores, did not yield accurate predictions for the growth rate within the linear range, in

accordance with the results of the convergence theory. Moreover, it will fail at the point where $\delta/\Delta\chi < 1$ due to stretch. It does, however, delay the deterioration of accuracy since it maintains a reasonable overlap between neighboring elements for longer times.

The third option, redistributing the vorticity field among an increasing number of elements arranged along the direction of principal direction of strain, is employed here. One monitors the distance between neighboring elements in the direction of maximum positive stretch $\Delta\chi$. If $\Delta\chi > \beta h$, where $1 < \beta < 2$, an extra element is placed halfway between the original elements and the vorticity is redistributed to compute the share of the new element. Ideally, this redistribution should not perturb the existing vorticity field, that is

$$\omega(\mathbf{x}, t) = \sum_{i=1}^N \Gamma_i f_{\delta}(\mathbf{x} - \mathbf{X}_i) = \sum_{i=1}^{N+n} \tilde{\Gamma}_i f_{\delta}(\mathbf{x} - \tilde{\mathbf{X}}_i) \quad (14)$$

where n is the number of new particles, and a \sim indicates the new value of the strength and location of the vortex elements. Unfortunately, this is a large dense system of linear equations to be solved every time step. Therefore, its benefit does not warrant the added cost.

A more economical scheme is based on equally interpolating the strength of the two original elements among the three elements, i.e. assuming uniform stretch between the two original elements. This amounts to splitting the original vortex dumbbell formed of two vortex discs into three discs when the distance between the centers of the two discs exceeds a threshold, as shown in Fig. 5. To minimize the interpolation errors, the maximum interdistance between neighboring elements is taken as $1.5 h$. This will also keep the ratio $\delta/\Delta\chi$ within reasonable limits.

To illustrate the degree of stretch experienced by this flow, we plot the growth of the length of the interface, and the total number of vortex elements, $N(t)$, used to capture this stretch for three perturbations $\epsilon = 0.001\lambda$, 0.01λ , and 0.1λ in Figs. 6, 7, respectively. Within the linear range the layer is subjected to mild stretch and N remains almost constant. Beyond that, the length of the line grows linearly and N multiplies accordingly. From the plots of the location of vortex elements, we noticed that most of the stretch is concentrated around the spiral center and the saddles at the boundaries of the domain.

II.3. SHEAR LAYER DYNAMICS

Figures 1, 2, 3 and 4 reveal that the growth of the perturbation and the development of the eddy structure can be divided into four stages: (1) linear growth; (2) rise to a maximum amplitude; (3) decay to a constant amplitude; and, (4) very slow decrease of amplitude. The first stage has been discussed. The strongest stretch and fastest multiplication of the vortex elements occur during the second stage where an eddy is forming in the middle of the wavelength and two braids are evolving between each two neighboring eddies. During this stage, the core maintains almost a circular configuration and the stretch is concentrated within the braids.

In the third stage, the eddy deforms into an elliptical structure, while the size of the perturbation decreases from its maximum value. This is accompanied by more stretch along the braids and within the core, and a slowdown of the eddy rotation. By the end of this stage, the thickness of the braids at the saddle points has become extremely small. At the final stage, the envelope of the core reaches a dynamic equilibrium, i.e., it does not rotate any more, while its boundaries keep on stretching as the fluid within the eddy starts to move in the main directions of the streams.

Although there are signs of that, it is difficult to confirm that the flow has reached a steady state.

The kinetic energy of perturbation u' . $u'/2$, where $u' = u - U$, and the total kinetic energy in the flow within the computational domain, $u.u/2$, are plotted in Figs. 8a and 8b. The first quantity rises with the growth of the perturbation and the formation of the eddy, then falls with the collapse of the eddy and the return of the fluid to the main streams (Corcos and Sherman [28]). The total kinetic energy is conserved since the flow is inviscid.

Using larger values for h while keeping δ/h the same caused a slight fattening of the core at latter times, while the main features of the flow were reproduced almost exactly. A similar modification of the structure is observed when using a first order time integration scheme, or increasing the time step. It was concluded that the errors introduced by using a small number of elements or a low order time integration scheme were numerical-diffusion-like errors. We also found that the dependence on the value of h , or the initial number of elements, becomes much less pronounced when the scheme of increasing the number of elements with stretch is employed. Figure 9 shows a qualitative comparison between the experimental results of Roberts et al. [29] and the computational results. Here we use a Galilean transformation to compare the experimental results of the spatially-developing layer and the computational results of the temporal layer.

The physical parameters that govern the flow field are λ and ϵ . Results for the rollup of a layer with $\lambda = 10.5 < \lambda^*$ are presented in Figs. 10 and 11, showing the growth of the perturbation and the vorticity field. λ^* is the wavelength of the most unstable perturbation. The computed growth rate $\dot{\Gamma} = 0.214$ while the analytical value is 0.208. More vorticity remains

in the braids between the eddies which are not strong enough to accomplish the same stretch as in the case of λ^* .

Figures 12 and 13 show results for $\lambda = 2 \lambda^*$, with $\epsilon = 0.01\lambda$ and 0.1λ , respectively. In the first case, $\dot{i} = 0.18$ while the analytical result is 0.173. The core is smaller and weaker than for the case of λ^* and hence the braids are thicker and maintain more of the original vorticity. At later times, a small scale rollup is observed near the boundary of the domain due to the instability of the vorticity layer that forms the braids. This rollup occurs only at the fourth stage of development when the midsection of the braids becomes almost stationary, i.e. when the motion produced by the braids is neutralized. Comparing Figs. 12 and 13, we see that contrary to the most unstable case, the effect of the initial perturbation is more pronounced here in terms of the size and shape of the eddy and the braids. Higher amplitudes of perturbation tend to form a larger core and thinner braids. The ratio between the major and minor axes of the elliptical core increases with ϵ and small amplitude waves start to appear on the braids.

Figures 14 and 15 show results for $\lambda = 3 \lambda^*$ with amplitudes $\epsilon = 0.01\lambda$, and 0.1λ , respectively. The effect of the amplitude is emphasized further since at larger ϵ , the core splits into two eddies. This bifurcation phenomenon was observed before by Pozrikidis and Higdon [30]. The braid instability is manifested here by the long waves that appear at the later stages of development of the layer.

With the presence of two perturbation wavelengths, a new process is observed. Figures 16 and 17 depict results for a layer subject to two perturbations superimposed at $t = 0$, at λ^* and $2\lambda^*$ with $\epsilon = 0.1\lambda^*$ for both perturbations. The results show that when the amplitude of the two perturbations are equal, pairing starts at the end of the second stage and

before any substantial elongation of the eddies. The growth of the subharmonic perturbation closely resembles that of the fundamental, as shown in Fig. 17. The eddies continue to deform while they pair until the "vortex fluid" contained within each structure start to rotate around a common center and their original boundaries become indistinguishable. Similar qualitative observations were shown in the computations of Corcos and Sherman [28] and Riley and Metcalfe [31].

III THE TEMPERATURE DISTRIBUTION

III.1. THE TRANSPORT ELEMENT METHOD

In an inviscid incompressible flow, the temperature distribution evolves according to the following form of the conservation of energy:

$$\frac{\partial T}{\partial t} + \mathbf{u} \cdot \nabla T = 0 \quad (15)$$

where T is temperature. This is equivalent to the statement that $T(\chi(\mathbf{X}, t), t) = T(\mathbf{X}, 0)$, where $\chi(\mathbf{X}, 0) = \mathbf{X}$ and $d\chi/dt = \mathbf{u}(\chi, t)$. To solve this equation using a Lagrangian element scheme, we start by introducing the temperature gradient $\mathbf{q} = \nabla T$, where $\mathbf{q} = (p, q)$ is a vector proportional but opposite to the heat flux vector $-k \mathbf{q}$, k being the thermal conductivity. The transport equation of \mathbf{q} is obtained by taking the gradient of Eq. (15) and rearranging:

$$\frac{\partial \mathbf{q}}{\partial t} + \mathbf{u} \cdot \nabla \mathbf{q} = - \mathbf{q} \cdot \nabla \mathbf{u} - \mathbf{q} \times \boldsymbol{\omega} \quad (16)$$

where $\boldsymbol{\omega} = \omega \mathbf{e}_z$ and \mathbf{e}_z is the unit vector normal to the (x, y) plane. Thus, along a particle path $\chi(\mathbf{X}, t)$, the temperature gradient changes according to the local strain field and turns with the local rotation of the fluid element. Using the vortex method described in the previous section, the velocity gradient may be computed directly from the vorticity distribution as: $\nabla \mathbf{u} = \sum \Gamma_i \nabla \mathbf{K}_\delta(\mathbf{x} - \mathbf{x}_i) + \nabla \mathbf{u}_p$, where \mathbf{u}_p is the irrotational component of the velocity.

The scheme proceeds in the same way as the vortex algorithm. The initial temperature gradient is discretized among a number of elements located at the centers of a square mesh of side h so that:

$$q(x,0) = \sum_{i=1}^N q_i h^2 f_{\delta}(x-x_i) \quad (17)$$

where $q(x,0)$ is the initial distribution of the temperature gradient, $q = \nabla T(x,0)$. To initialize q_i , a similar procedure to that used in computing the strength of the vortex elements is employed here, i.e. Eq. (12) with q instead of ω , is solved to find $q_i(0)$. To update $q_i(t)$, Eq. (16) is solved in two fractional steps: in the first step, the elements are transported without changing their strength or their core shape or size. In the second step, the strength of the elements is updated according to:

$$\frac{dq_i}{dt} = -q_i \cdot \nabla u_i - q_i \times \omega_i \quad (18)$$

Thus, a system of ordinary differential equations must be integrated to update the strength of the gradient elements as they move along particle paths. The local gradient at time t is computed from:

$$q(x,t) = \sum_{i=1}^N q_i(t) h^2 f_{\delta}(x-x_i) \quad (19)$$

The core function f_{δ} may be different for the vortex elements and the gradient transport elements. In this work, we use the same form for both. The temperature can be calculated by direct integration of the gradient along a determined path. As pointed out by Anderson [17], a convenient expression can be obtained by expressing the temperature as a Poisson integral in the temperature gradient, $T = \int \nabla G(x-x') \cdot \nabla T(x-x') dx'$. Using Eq. (19) for q_i , we get:

$$T(x,t) = \sum_{i=1}^N q_i(t) \cdot \nabla G_{\delta}(x-x_i) \quad (20)$$

where

$$w_{\delta} = \frac{(x,y)}{r^2} \kappa\left(\frac{r}{\delta}\right)$$

while the relationship between f and κ is as before. This expression is convenient when used in connection with the vortex method since all the functions involved in the summation must be computed for the transport of the vortex elements and with simple programming tricks, the increase in cost can be minimized.

Results obtained for the temperature distribution in the shear layer of Figs. 2, 3 and 4 are shown in Figs. 18, 19 and 20, respectively. At $t = 0$, the temperature distribution is described by an error function, with $T(x,0) = 0.5 (1 + \text{erf}(Y))$. This choice is motivated by the fact that this is the fundamental solution of the diffusion equation. Therefore, an initial discontinuity in temperature would develop into an error function before the perturbation grows and convection effects become important. The layer is first perturbed by a sinewave by displacing the elements according to $Y = \tilde{Y}(X)$, and then the temperature gradient $Q(X)$ is computed. The discrete values $q_i(0)$ are obtained as follows: Since the temperature is constant along the streamlines after the perturbation $Y = \tilde{Y}(X)$, then $T(X,0) = \Theta(X) = 0.5(1 + \text{erf}(Y - \tilde{Y}(X)))$. From this equation we can recover the initial distribution of $P(X,0)$, and $Q(X,0)$ as follows:

$$\begin{aligned} P(X) &= \frac{\partial \Theta}{\partial X} = -\text{Gau}(Y - \tilde{Y}(X)) \frac{d\tilde{Y}}{dX} \\ Q(X) &= \frac{\partial \Theta}{\partial Y} = \text{Gau}(Y - \tilde{Y}(X)) \end{aligned} \quad (21)$$

where Gau is a Gaussian similar to Eq. (11a). These expressions are then used in Eq. (17) to compute q_i . The values of $q_i(0)$ were initialized one column at a time, i.e. for fixed values of X , to avoid solving N^2 simultaneous equations, and instead solve N_X of N_Y simultaneous equations. The error associated with this approximation was very small since the perturbation was kept at a low value.

In the computations, we used the same particles to transport vortex elements and elements of the temperature gradient. This represents a substantial saving since the kernel functions appearing in the expressions of the velocity, velocity gradients, and temperature can be computed all at once and the velocity is computed only for one set of elements.

III.2. ENTRAINMENT IN A SHEAR LAYER

To quantify the overall change in the temperature distribution, we define a quantity T , similar to the growth I , as;

$$T = \int_0^\lambda \int_{-\infty}^{\infty} |T(x,t) - \Theta(x)| \quad (22)$$

T can be regarded as an average thermal thickness of the shear layer. Within the linear range, the temperature distribution remains essentially the same, except for getting shifted up or down depending on the local sign of the perturbation. In Fig. 21, the natural logarithm of $T(t)$ is shown for three values of the initial amplitude of the perturbation. The accuracy of the calculation of the temperature profiles depends on the initialization of the vorticity and temperature gradient, and on the value of δ/h .

During the second stage, and with the rollup of the interface and the establishment of a spiral center at the midpoint of the wavelength, a complex temperature gradient develops as a result of the motion of the cold fluid upwards and the hot fluid downwards around the spiral center. Within

this stage, if the number of transport elements remained the same, i.e. stretch was not accommodated by introducing elements where the local strain is large, the temperature distribution would collapse very quickly. In the problem of periodic shear layer, this collapse leads to values of $T(x, +\infty, t) < 1$ and $T(x, -\infty, t) > 0$. The reason of the loss of accuracy is clear from Eq. (16). When the elements move apart, the accuracy of computing the velocity gradient ∇u deteriorates, and hence the new values of q_i accumulate large errors. Thus, while the calculation of the velocity field at the early stages of strong stretch using a fixed number of vortex elements may be acceptable for a short period of time, the calculations of the velocity gradient and the evolution of a passive scalar will show unacceptable errors.

To continue beyond the linear stage, the distance between neighboring elements in the principal direction of strain, Δx , must to be monitored. If $\Delta x > \beta h$, where $\beta > 1$, one extra element is added between the two original elements and the total value of q_i is redistributed equally between the three elements. In the calculations, we used $\beta = 1.5$. Numerical convergence, in which one systematically refines the numerical parameters until no more changes are observed, was used to obtain these results.

The effect of the shear layer rollup on the temperature distribution is seen in Figs. 18 and 19. Immediately after the interface reaches a vertical position, an S-shape starts to form indicating that cold fluid has been transported from the lower stream into the upper stream and vice versa. This phenomenon, known physically as engulfment or entrainment, relies solely on convective transport and is observed when molecular diffusion, which acts to dissipate the sharp gradients, is small. Fast entrainment with small diffusion leads to "unmixedness" of hot and cold fluids within

the eddy core. With more fluid being transported to the opposite stream the S-shape grows, reaching a maximum amplitude when the interface becomes horizontal. At this moment, fluid with the maximum and the minimum temperature has been entrained into the core, i.e. entrainment has reached all the way to the free streams to bring fluid into the core of the eddy. This is the stage of maximum entrainment when the core size reaches its largest size and cannot accommodate any more fluid. In the case of $\epsilon = 0.1\lambda$, it corresponds to $t = 8.0$, which is at the end of the second stage of development. To make the correspondence between the temperature profiles and the evolution of the interface of the layer clear, we plot the latter in Fig. 22, showing the actual vortex elements that were used in the computations of the interface. At this time, the interface has rotated 180° around the spiral center. This is the first step in the process of homogenization of the core.

As the core rotates further into the third stage, the inner part of the interface develops a secondary instability that rolls up in a very similar manner to the primary instability. This secondary instability is in phase with the primary instability and can be envisioned by zooming in on the intersection between the interface and the horizontal centerline of the layer. Due to the elongation of the outside envelope of the core, the wavelength of the secondary instability grows with time, as seen from Fig. 22. However, the amount of fluid within the elliptical envelope remains constant, or decreases slowly as seen from Fig. 21 for the temperature thickness of the layer. The growth of the secondary instability provides a mechanism of internal entrainment within the core. During the growth of the secondary instability, an inverted S-shape, or a Z-shape, forms in the middle of the temperature profile, Figs. 18-20. The entrainment associated

with this instability turns the fluid in a clockwise fashion, making the inside of the core more uniform. This is seen from the decay of the peaks in the temperature profile as this Z-shape grows.

With another 180° turn of the interface at the spiral center, a smaller S-shape forms in the middle of the profile due to the onset of an even shorter wavelength instability that is in-phase with the primary instability. While the existence of the secondary instability was not observed before in numerical simulations, its presence is clearly seen in the experimental results in Fig. 9.

The onset and subsequent growth of successively shorter wavelength instabilities continues, leading to a more uniform temperature distribution within the eddy core. An asymptotic limit to this process can be foreseen: it is the formation of a temperature profile with the following shape: $T = T_\infty$ at $y > \Delta/2$; $T = T_{-\infty}$ at $y < -\Delta/2$, and $T = (T_\infty + T_{-\infty})/2$ in between, where Δ is the minor axis of the elliptical envelope at $x = \lambda/2$. This shape has been measured experimentally by Konrad [32], (see also Broadwell and Breidenthal [33],) for mixing layer flows at high Reynolds numbers. This is, to our knowledge, the first time it has been computed numerically.

By the end of the third stage, the layer cannot absorb any more energy and a relaxation process occurs, during which the kinetic and thermal energy are fed back into the main flow streams. This reverse action is accompanied by the fluid leaving the core and moving back into the main streams at a very slow rate.

III.3. EFFECT OF MOLECULAR DIFFUSION

The generation of large temperature gradients within the core as successive instabilities evolve gives rise to large molecular diffusion fluxes which act to smooth out some of these gradients. While for most

cases of interest the diffusion transport is very small relative to the convective transport, i.e. the Reynolds number is high, diffusion plays an important role since mixing at the molecular scales can only be accomplished via molecular diffusion. Thus, the combined action of convective entrainment and molecular diffusion leads to the homogenization of the temperature within the eddy core. To simulate the effect of diffusion for small values of α in the current model of a shear layer, Eqs. (15) and (16) are modified by adding a diffusion term:

$$\frac{\partial T}{\partial t} + \mathbf{u} \cdot \nabla T = \alpha \nabla^2 T \quad (23)$$

and

$$\frac{\partial \mathbf{q}}{\partial t} + \mathbf{u} \cdot \nabla \mathbf{q} = - \mathbf{q} \cdot \nabla \mathbf{u} - \mathbf{q} \times \boldsymbol{\omega} + \alpha \nabla^2 \mathbf{q} \quad (24)$$

where α is the non dimensional molecular diffusivity, or the inverse of the Peclet number. At high speed flow, the Peclet number is typically 10^3 - 10^5 . To solve Eq. (24) using the scheme that we have developed, a third fractional step must be added, in which the value of \mathbf{q} is updated according to:

$$\frac{\partial \mathbf{q}_i}{\partial t} = \alpha \nabla^2 \mathbf{q}_i \quad (25)$$

without changing the shape of the core function or the value of \mathbf{q}_i . By taking $\delta = \delta(t)$, and substituting Eq. (19) into Eq. (25), we find that $d\delta^2/dt = 4\alpha$. Thus, the core radius must change according to:

$$\delta^2 = \delta_0^2 + 4 \alpha t \quad (26)$$

where δ_0 is the core radius at $t = 0$ (for more discussion, see Leonard [1], Ashurst [34].) The cores of the vortex elements and of the temperature gradient elements become different with time.

Results in Fig. 23 show the temperature profile at $T = 20$ for the case of λ^* and $\varepsilon = 0.1\lambda^*$, evaluated for $\alpha = 0.0, 0.00001, 0.0001, 0.001, 0.01$ and 0.1 . Note that the temperature profiles of the first two cases are almost identical, indicating that the effective diffusivity of the inviscid calculation is of the order of 10^{-5} . In the last case, the temperature profile is similar to the case of pure diffusion, indicating that diffusion proceeds at a rate faster than the instability. It is also noticed that for moderate values of α , $0.0001 < \alpha < 0.01$, diffusion only affects the core of the eddies, making them achieve a homogeneous state faster.

Greengard [35], in his analysis of the core-spreading vortex method in which a fixed number of elements are used to perform the convective transport and their cores are expanded to account for the effect of diffusion, showed that the scheme does not converge to the correct equation of motion except when the flow field outside the region $|\omega| > 0$ is uniform. We have used a core spreading scheme to simulate the effect of diffusion in the energy equation with two modifications: (1) the number of transport elements which discretize the gradient field is increasing with time; and (2) α is kept small. Utilizing an increasing number of elements to perform the convective transport is essential since it is important to determine the gradient field accurately, in terms of the location and strength of the elements, before the diffusion effect can be added. In essence, adding transport elements at areas of high strain allows the computational elements to capture all the vorticity, and temperature gradient carrying fluid at all times, even after the vorticity has been fragmented by the action of the

strain field. Without this step, strain will create areas which are void of elements, thus, diffusion cannot be represented.

In the particular application of a shear layer at high Reynolds number, the flow field is uniform outside the area where $|\omega| > 0$, and this area expands slowly by diffusion if $\alpha < 1$. Limiting the simulations to small values of α : (1) reduces the errors associated with the fractional step scheme used to solve Eq. (24) (Beale and Majda [36]); and (2) reduces the errors concomitant with convecting an element with the velocity evaluated at its center while its core radius is growing. To accommodate this growth, which causes the spread of vorticity in the direction normal to the streamlines, one may be forced to add elements in the direction normal to the maximum principal strain direction, and then redistribute the vorticity. It is, therefore, clear that the scheme is only applicable when $\alpha < 1$ and for short time, i.e., $\alpha t < 1$. If these two conditions are not satisfied, one must divide each element whose core radius is larger than a critical value into a number of separate elements so that the convective transport can be performed accurately. Since most interest in shear layer flows is at high Reynolds number, or $\alpha < 1$, and within the short time of development of the convective instability, we feel that the current scheme is sufficient for this application.

To define a quantitative measure of mixing in a single phase fluid with thermal stratification, we observe first that mixing is only achieved by molecular diffusion. Large entrainment fluxes bring the unmixed fluid layers in contact along a larger interface; however, molecular diffusion across this interface is what accomplishes the actual mixing. A measure of mixing can be defined as:

$$M(t, \alpha, \varepsilon) = \int_0^\lambda \int_{-\infty}^{\infty} |T(x, t, \alpha, \varepsilon) - T(x, t, 0, \varepsilon)| dx$$

Note that $M(t, 0, \varepsilon) = 0$, while $M(t, \alpha, 0)$ is due to diffusion only. In Fig. 24 $M(t, \alpha, 0.1)$ is plotted for various values of α and for λ^* . It represents mixing due to the combined action of entrainment and diffusion. At very small values of α , mixing is limited by the amount of diffusion across the fluid layers which have been entrained into the eddy core. Since for these values of α the convective transport is faster than the diffusive transport, mixing increases approximately as $\sqrt{\alpha}$. However, as α increases, and at longer times, mixing proceeds at a slower rate since it becomes bounded by entrainment of unmixed fluid into the eddy core which almost ceases by the end of the second stage of rollup.

IV CONCLUSIONS

In this work, the vortex element method is used to compute both the early and late stages of development of an inviscid temporal mixing layer. In this method, the vorticity is initially discretized among overlapping element of radially symmetric cores. We find that using a scheme which depends on equating the vorticity at the centers of the elements with the accumulative value induced by all elements is necessary to obtain accurate results for initial vorticity discretization. We also find that to ensure the accuracy of the solution for short times, the ratio of the core/separation should be larger than one. Very large cores introduce a strong perturbation in the vorticity field, while smaller cores cause a fast deterioration of accuracy. Using fourth order Gaussian cores results in better accuracy over second order Gaussian cores. However, we feel that the improvement in accuracy does not warrant the added cost.

As time proceeds, the distance between neighboring elements exceeds its initial values due to the generation of strong stretch. This leads to the computation of inaccurate velocities and is manifested by the irregular motion of the vortex elements. To overcome this problem, the vorticity is constantly redistributed among elements inserted along the principal direction of strain to capture the local deformation of the vorticity field and to improve the resolution of the calculations. This is achieved by an insertion-and-interpolation process, which is applied where the distance between the neighboring centers along the principal direction of strain exceeds a threshold value. We show, using solutions for a shear layer perturbed at different wavelengths and amplitudes, that this process yields accurate solutions for the vorticity distribution at long times and after strong strain fields have caused a severe distortion of the streamlines.

This scheme enables one to accurately compute the local velocity gradient which, while it is not required in connection with vorticity convection, is necessary for the accurate evaluation of the convection of a passive scalar.

The temperature gradient, distributed over transport elements which resemble in their structures the vortex elements, are used to compute the temperature distribution as the rollup evolves. Contrary to vorticity, scalar gradients are not conserved along particale paths, thus, the strength of these transport elements is changed according to the straining and rotation of the material elements. The scheme is capable of capturing very sharp gradients that develop within the core since the elements migrate towards these zones by convection. The multiplication of these elements via stretch, which inadvertently mimics the physical process by which large scalar gradients are generated, provides a naturally adaptive grid to compute these gradients. By expanding the cores of the transport elements, the effect of small diffusivities can be simulated as a small perturbation to the convection field. Diffusion, even at high Peclet number, is responsible for generating areas of uniform temperature inside the eddy since it acts to smooth out the sharp gradient created by convection.

The application of vortex methods to problems in which the no-slip boundary condition along solid walls must be satisfied can be accomplished using the random vortex method (Chorin [37], and Sethian and Ghoniem [38].) In this method, extra vortex elements are generated along the solid walls to cancel the slip velocity, and the diffusion of vorticity is simulated by the random walk of the vortex elements. At high Reynolds number, a strong strain field is expected to cause similar problems as described in this work, i.e., areas of large stretch will be depleted from vortex elements and accurate resolution of the vorticity field may be lost around these areas. Extending

the insertion-and-interpolation scheme described in this work to the random vortex method requires: (1) adding a third fractional step, which must be performed after the convection and before the diffusion steps, for the redistribution of the vorticity field among elements arranged in the direction of principal strain; and (2) computing the strain field at the center of the vortex elements in a Lagrangian form since, due to random walk, neighboring vortex elements and neighboring material elements change as time evolves. The implementation of these two steps must be preceded by careful formulation, and will require lengthy computation.

REFERENCES

1. Leonard, A., J. Comput. Phys., 37, 289 (1980).
2. Beale, J.T. and Majda, A., J. Comput. Phys., 58, 188 (1985).
3. Hald, O.H., "Convergence of vortex methods fro Euler's equations, III," SIAM J. Num. Anal., 1987 (to appear).
4. Ghoniem, A.F. and Ng, K.K., Phys. Fluids, 30, 706 (1987).
5. Chorin, A.J., J. Fluid Mech., 57, 785 (1973).
6. Fritts, M.J., and Boris, J.P., J. Comput. Phys., 31, 173 (1979).
7. Zabuski, N.J., Hughes, M.H. and Roberts, K.V., J. Comput. Phys., 30, 96 (1979).
8. Chorin, A.J., Hughes, T.J.R., McCracken, M.F., Marsden, J.E., Commun. Pure and Applied Math., 41, 205 (1978).
9. Del-Prete, V.M. and, Hald, O., Math. Comput., 32, 791 (1978).
10. Hald, O.H., SIAM J. Num. Anal., 16, 726 (1979).
11. Beale, T.J. and Majda, A., Math. Comput., 39, 1 (1982).
12. Beale, T.J. and Majda, A., Math. Comput., 39, 29 (1982).
13. Nakamura Y., Leonard, A. and Spalart, P., Proceedings of the AIAA/ASME Third Joint Thermophysics, Fluids, Plasma and Heat Transfer Conference, AIAA Paper No. 82-0948.
14. Roberts, S., J. Comput Phys., 58, 29 (1985).
15. Perlman, M., J. Comput. Phys., 59, 200 (1985).
16. Anderson, C. and Greengard, C., SIAM J. Numer. Anal., 22, 413 (1985).
17. Anderson, C., J. Comput. Phys., 61, 417 (1985).
18. Krasny, R., " J. Comput. Phys., 65, 292 (1986).
19. Zabuski, N.J., and Overman, E.A., J. Comput. Phys., 52, 35 (1983).
20. Krasny, R., "Computation of vortex sheet rollup in the Trefftz plane", submitted for publication.
21. Chorin, A.J., in Computing Methods in Applied Sciences and Engineering, R. Glowinski and J.L. Lions, ed., North-Holland, INRIA, p. 229 (1980).

22. Ghoniem, A.F. and Oppenheim, A.K., in Proc. 8th Int. Conf. Num. Meth. Fluid Dynamics, E. Krause, Ed., Springer-Verlag, New York, p. 224 (1982).
23. Ghoniem, A.F. and Oppenheim, A.K., AIAA J., 22, 1429 (1983).
24. Ghoniem, A.F. and Sherman, F.S., J. Comput. Phys., 61 1, (1985).
25. Anderson, C., "Vortex method for variable density flows", Ph.D. dissertation, Department of Mathematics, U.C. Berkeley, 1983, (unpublished).
26. Michalke, A., J. Fluid Mech., 19, 543 (1964).
27. Betchov, R. and Criminale, Jr., N.O., Stability of Parallel Flows, Academic Press, New York, 330 p., 1967.
28. Corcos, G.M. and Sherman, F.S., J. Fluid Mech., 73, 29 (1976).
29. Roberts, F.A., Dimotakis, P.E., Roshko, A., "Kelvin-Helmholtz in instability of superposed streams," In Album of Fluid Motion, ed. M. Van Dyke, p. 85, Stanford, CA, Parabolic Press.
30. Pozrikidis, C. and Higdon, J.J.L., J. Fluid Mech., 157, 225 (1985).
31. Riley, J.J. and Metcalfe, R.W., Proceedings of the AIAA 19th Aerospace Sciences Meeting, AIAA Paper No. 80-0274.
32. Konrad, J.H., "An experimental investigation of mixing in two-dimensional shear flows with application to diffusion limited chemical reactions, Project SQUID Tech. Rep. CIT-8-PUI, 1976.
33. Broadwell, J.E., and Breidenthal, R.E., J. Fluid Mech., 125, 397 (1982).
34. Ashurst, W.T., in Proceeding of the 1st Symposium on Turbulent Shear flow, Durst et al., ed., p. 402, Springer-Verlag, Berlin, 1979.
35. Greengard, C., J. Comput. Phys., 61, 345 (1985).
36. Beale, J.T., and Majda, A., Math. Comput., 37, 243 (1981).
37. Chorin, A.J., SIAM J. Sci Statist Comput., 1, 1 (1980).
38. Sethian, J.A., and Ghoniem, A.F. "Validation of the vortex method," accepted for publication at J. Comput. Phys., 1987.

FIGURE CAPTION

- Figure 1. The growth of the perturbation amplitude I with time for the most unstable case, λ^* , for three values of the initial perturbation $\epsilon/\lambda = 0.001, 0.01$ and 0.1 , showing the linear range and the saturation of the perturbation. Each curve is normalized with respect to the corresponding value of I at $t = 0$.
- Figure 2. The location and velocity of the vortex elements during the rollup of a temporal shear. $\lambda = \lambda^*$, with $\epsilon/\lambda = 0.001$. $N(0) = 572$, $h = 0.3$, $\delta = 0.375$, and $\Delta t = 0.1$.
- Figure 3. The location and velocity of the vortex elements. Wavelength is λ^* , and $\epsilon/\lambda = 0.01$. At $t = 0$, $N = 440$, $h = 0.33$, $\delta = 0.4$ and $\Delta t = 0.1$.
- Figure 4. The location and velocity of the vortex elements for $\lambda = \lambda^*$, and $\epsilon/\lambda = 0.1$. All the numerical parameters are the same as in Fig. 3.
- Figure 5. Schematic diagram showing how the vorticity is redistributed among three elements when the distance between two neighboring elements exceeds a pre-specified value. (x_n, y_n) are the coordinates of the new elements.
- Figure 6. The total length of the interface, originally at $y = 0$, with time for the cases presented in Figs. 2, 3, and 4, normalized with respect to its length at $t = 0$.
- Figure 7. The number of vortex elements used to represent the vorticity field during rollup for three initial perturbations, normalized with respect to the corresponding value at $t = 0$.
- Figure 8. (a) The total kinetic energy of the perturbation based on the perturbation velocity, $(U(x) - u(x, t))^2$, and (b) The total kinetic energy of the flow, u^2 , for $\epsilon/\lambda = 0.001, 0.01, 0.1$.

Figure 9. The evolution of the vorticity field with time, compared with the experimental results of Roberts et al. [29] for the spatial development of a small perturbation of a shear layer.

Figure 10. The growth of the perturbation amplitude for $\lambda = 10.5$, $\epsilon/\lambda = 0.01$. $N(0) = 455$, $h = 0.3$, $\delta = 0.375$ and $\Delta t = 0.1$.

Figure 11. The location and velocity of the vortex elements used in the calculations of the case shown Fig. 10.

Figure 12. The vorticity field for $\lambda = 2 \lambda^*$, $\epsilon/\lambda = 0.01$. $N(0) = 540$, $h = 0.44$, $\delta = 0.5$, $\Delta t = 0.1$.

Figure 13. The vorticity field for $\lambda = 2 \lambda^*$, $\epsilon/\lambda = 0.1$, using the same numerical parameters as in Fig. 12.

Figure 14. The vorticity field for $\lambda = 3 \lambda^*$, $\epsilon/\lambda = 0.01$. $N(0) = 818$ and the values of h , δ , and Δt are the same as in Fig. 12.

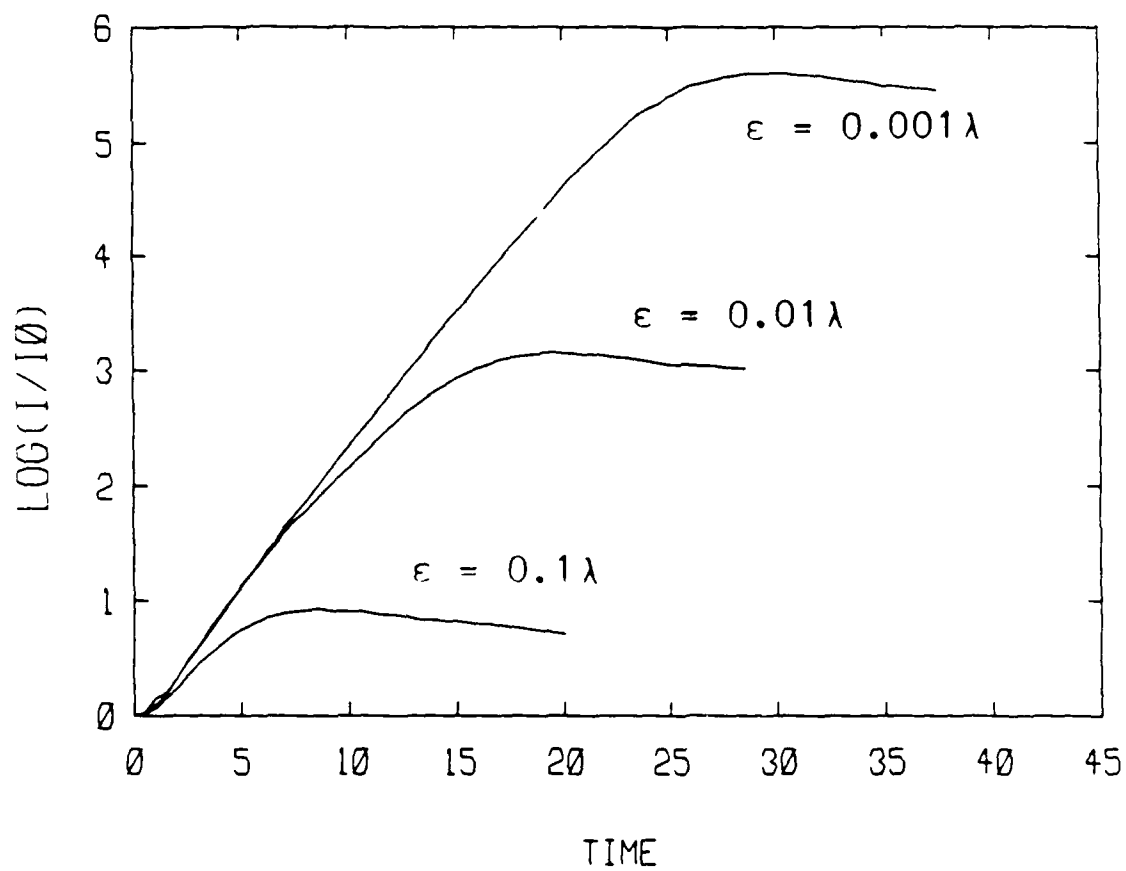
Figure 15. The vorticity field for $\lambda = 3 \lambda^*$, $\epsilon/\lambda = 0.1$, using the same numerical parameters as in Fig 14.

Figure 16. The location and velocity of the vortex elements for two perturbations, $\lambda_1 = \lambda^*$ and $\lambda_2 = 2 \lambda^*$, with $\epsilon = 0.1 \lambda^*$ for both perturbations. $N(0) = 336$, $h = 0.55$, $\delta = 0.6$ and $\Delta t = 0.5$. A fourth order time integration scheme is used to transport the elements.

Figure 17. The total amplitude of the perturbation of the case in Fig. 16.

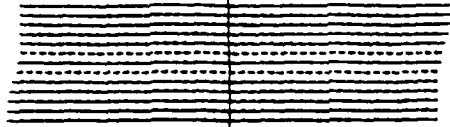
Figure 18. The temperature distribution across the layer at the center of the core, for λ^* and $\epsilon/\lambda = 0.001$. The numerical parameters are the same as in Fig. 2.

- Figure 19. The temperature distribution across the layer at the center of the domain for λ^* and $\epsilon/\lambda = 0.01$. The numerical parameters are the same as in Fig. 3.
- Figure 20. The temperature distribution across the layer at the center of the core for λ^* and $\epsilon/\lambda = 0.1$. The numerical parameters are the same as in Fig. 4.
- Figure 21. The variation of the logarithm of the temperature thickness T with time for the cases in Figs. 2, 3, and 4.
- Figure 22. The rollup of the interface, defined by the layer which coincides with $y = 0$ at $t = 0$ for the case shown in Fig. 4.
- Figure 23. The effect of thermal diffusion on the temperature distribution across the layer. Temperature is shown at $t = 20$ for the case shown in Fig. 4.
- Figure 24. Total mixing, $M(t, \alpha, 0.1)$ due to the combined action of entrainment and diffusion, evaluated for different values of α .

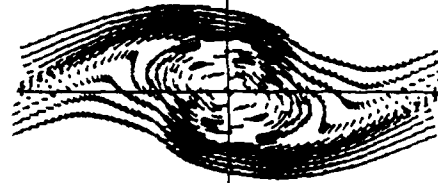


Growth Rate for the Most Unstable Mode

Fig. 1



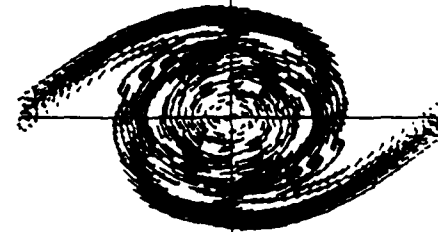
TIME = 0.00 ELEMENTS = 572



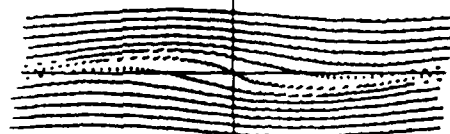
TIME = 24.00 ELEMENTS = 891



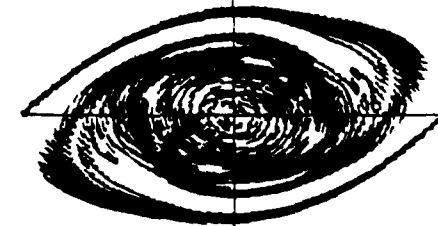
TIME = 8.00 ELEMENTS = 572



TIME = 30.0 ELEMENTS = 1623



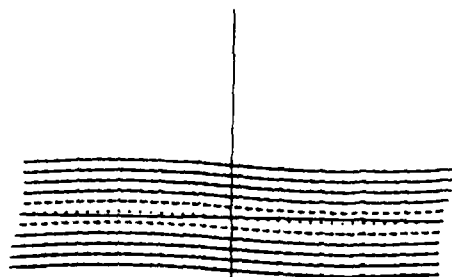
TIME = 16.00 ELEMENTS = 595



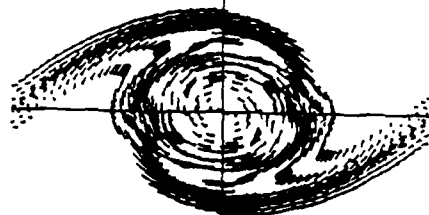
TIME = 37.50 ELEMENTS = 3257

ORDER OF INTEGRATION=2 ORDER OF CORE=2

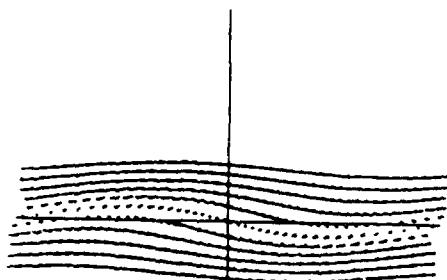
LAYER=13 BLOB/LAYER=44 SIOB=0.375 THICKNESS=3.600 AMPL.=0.0010 U LENGTH=13.20



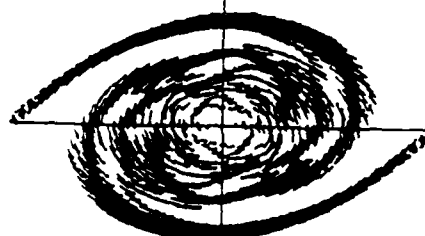
TIME = 0.00 ELEMENTS = 440



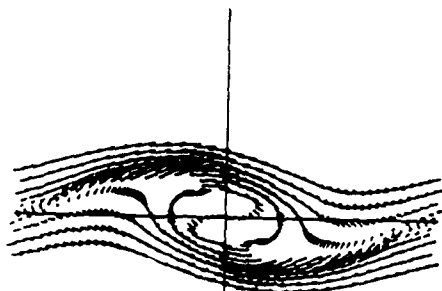
TIME = 18.00 ELEMENTS = 980



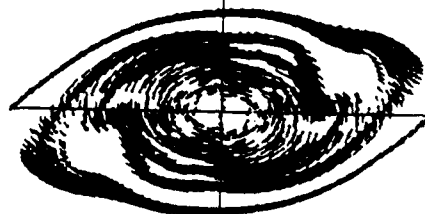
TIME = 6.00 ELEMENTS = 440



TIME = 24.00 ELEMENTS = 1778



TIME = 12.00 ELEMENTS = 574



TIME = 28.5 ELEMENTS = 2747

ORDER OF INTEGRATION=2

ORDER OF CORE=2

MESH=21x21

STATION=22

LAYER=11

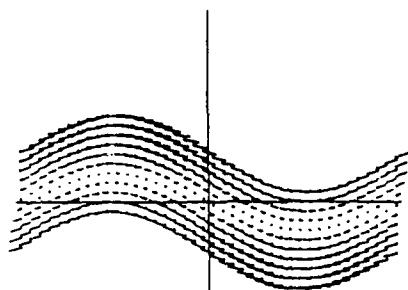
BLOB/LAYER=40

SCOB=0.400

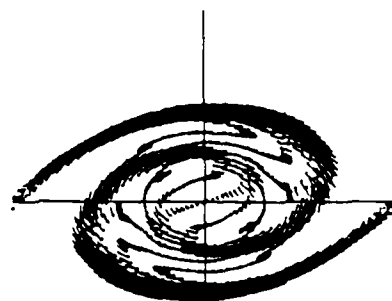
THICKNESS=3.300

AMPL.=0.0100

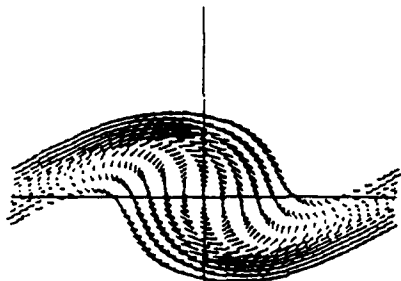
W LENGTH=13.20



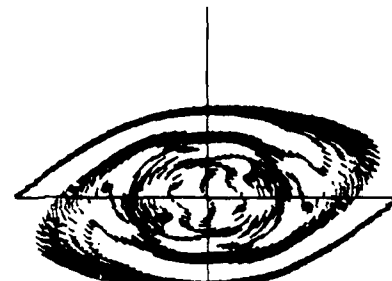
TIME = 0.00 ELEMENTS = 440



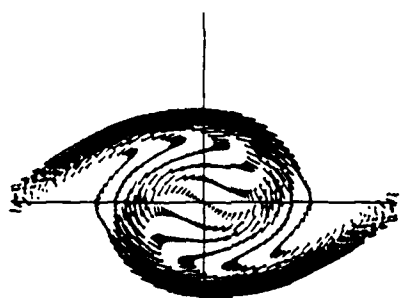
TIME = 12.00 ELEMENTS = 1252



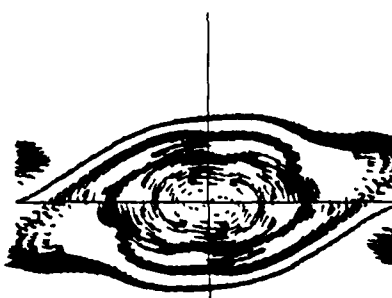
TIME = 4.00 ELEMENTS = 586



TIME = 16.00 ELEMENTS = 1782



TIME = 8.00 ELEMENTS = 858



TIME = 20.00 ELEMENTS = 2458

ORDER OF INTEGRATION=2

ORDER OF CORE=2

MESH=21x21

STATION=22

LAYER=11

BLOB/LAYER=40

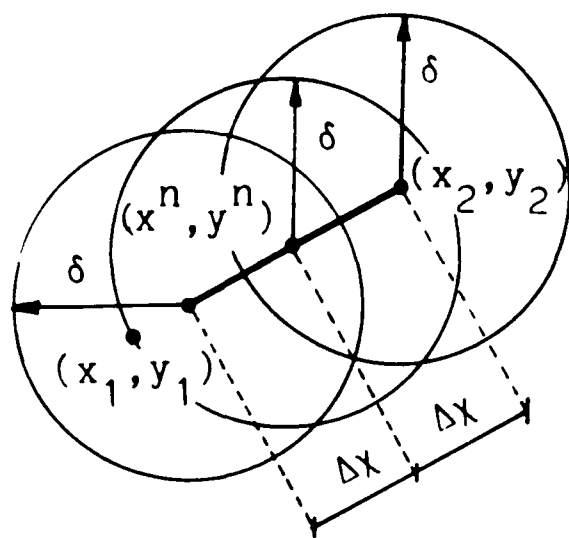
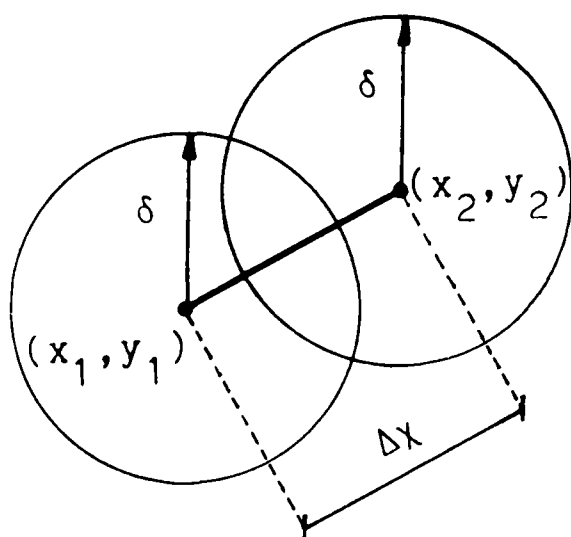
SIGB=0.400

THICKNESS=3.300

AMPL.=0.1000

U.LENGTH=13.20

Fig 4



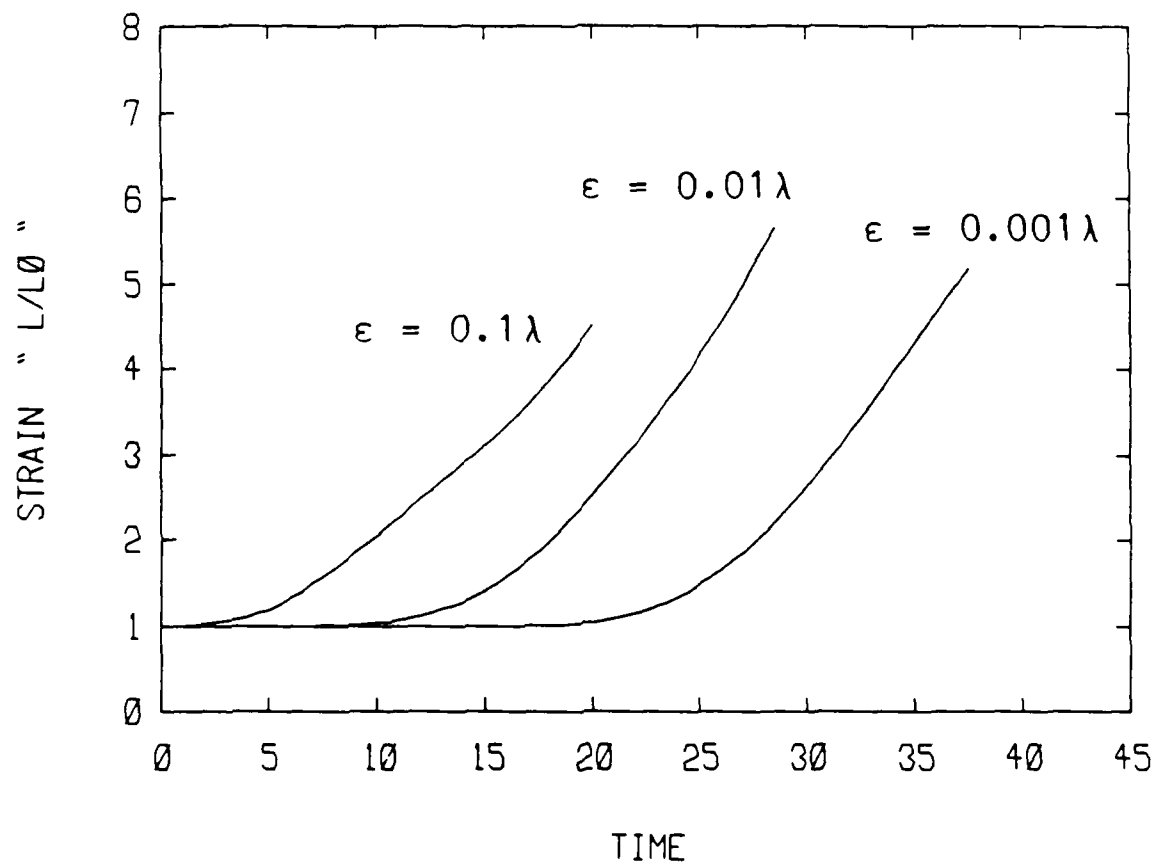


Fig 6

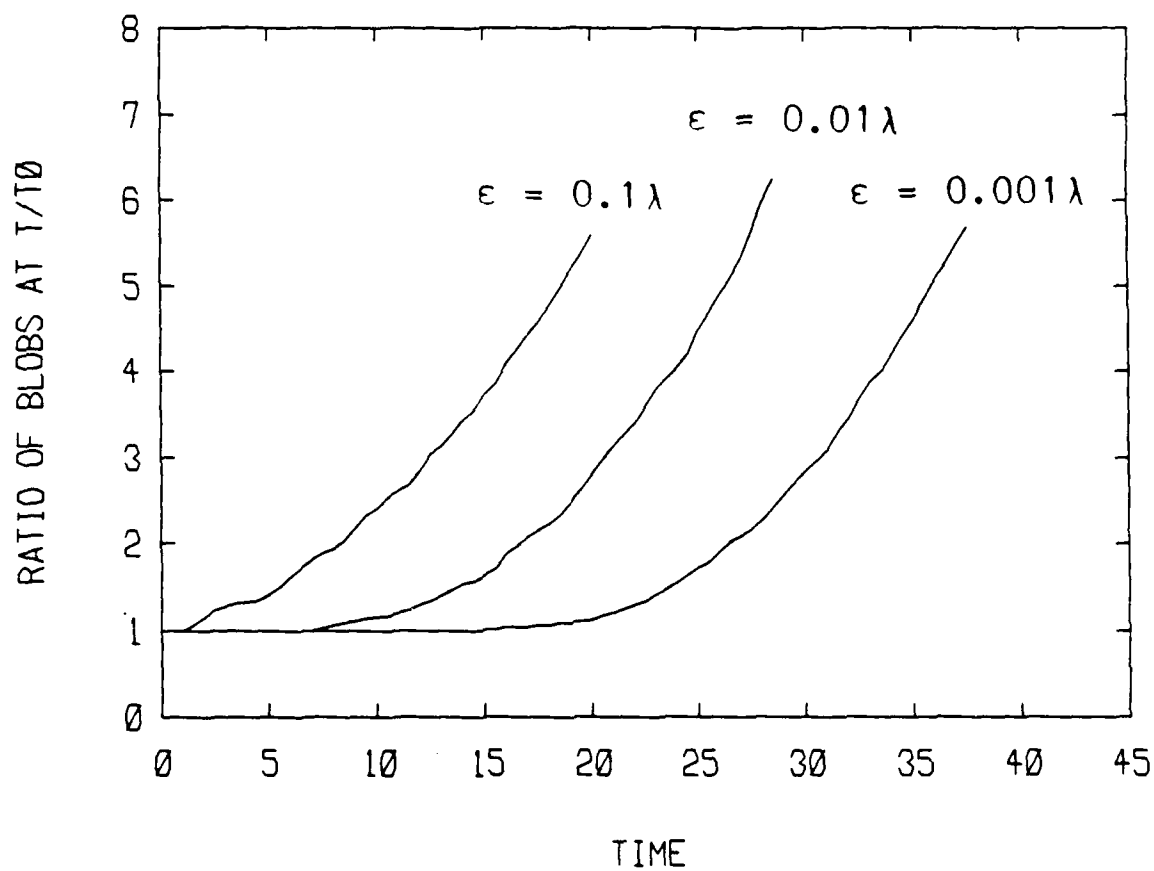


Fig. 1

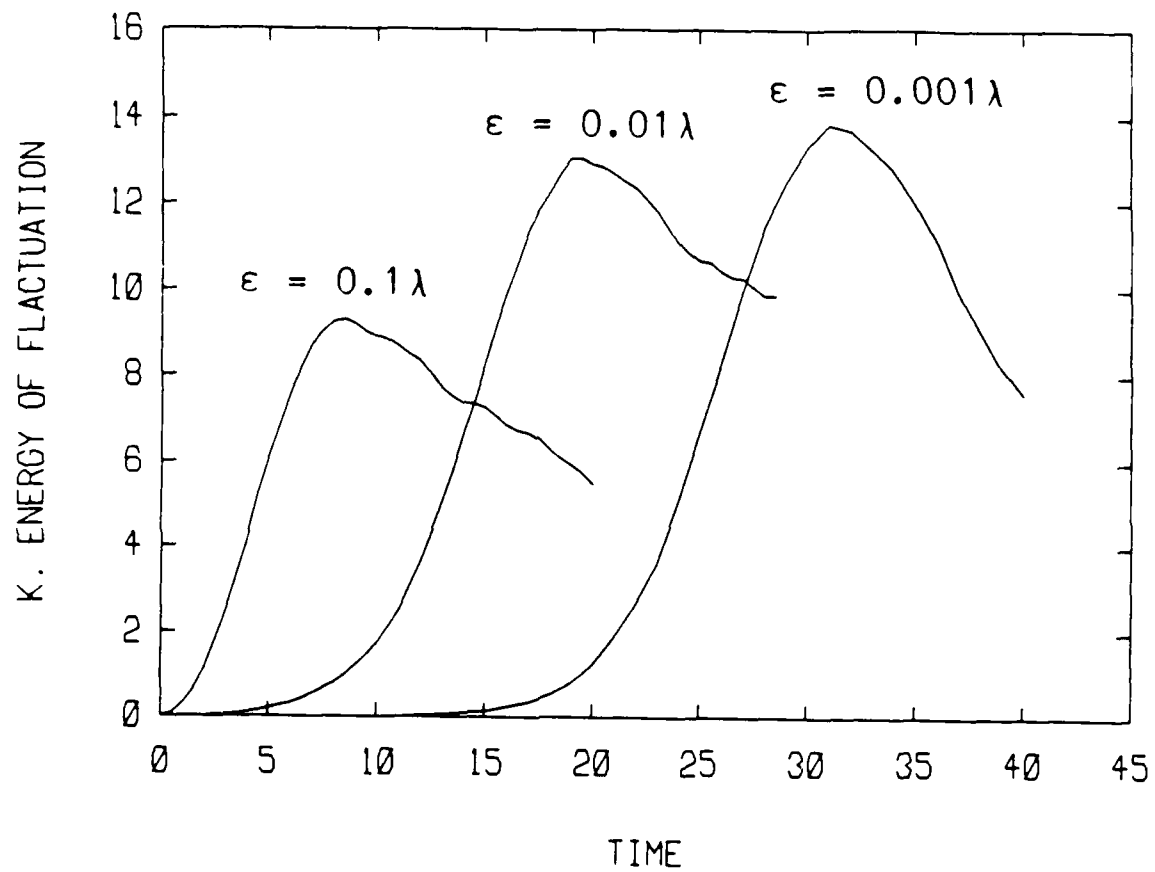


Fig. 12

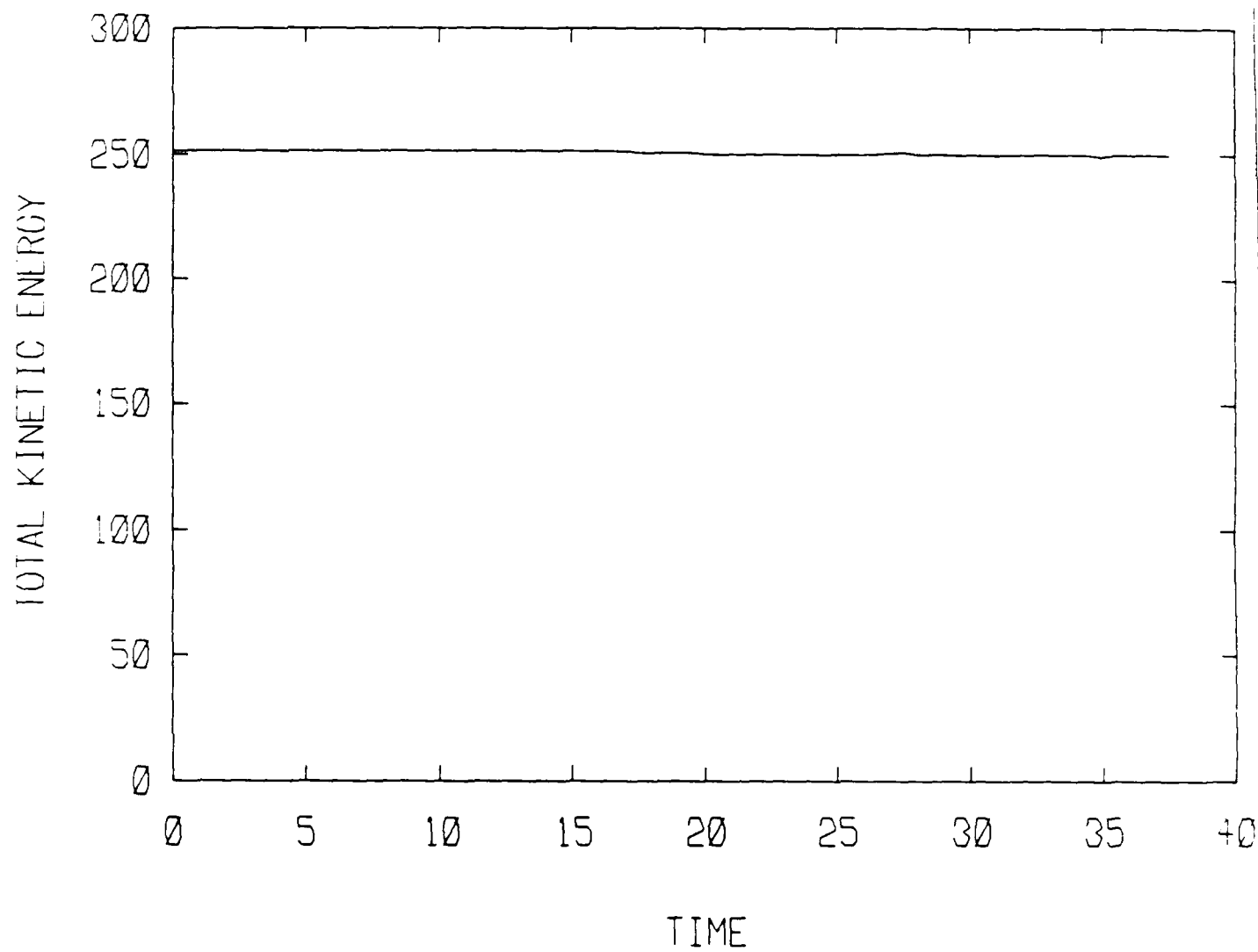


Fig. 10



$t = 8$ $t = 12$ $t = 16$ $t = 20$

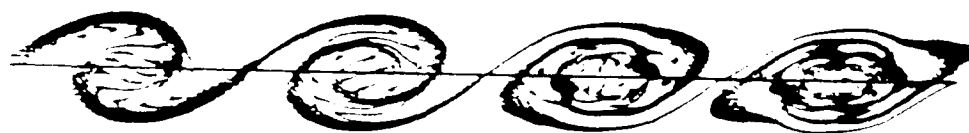


Figure 1. Evolution of the vortex tube structure over
time (multiple view)

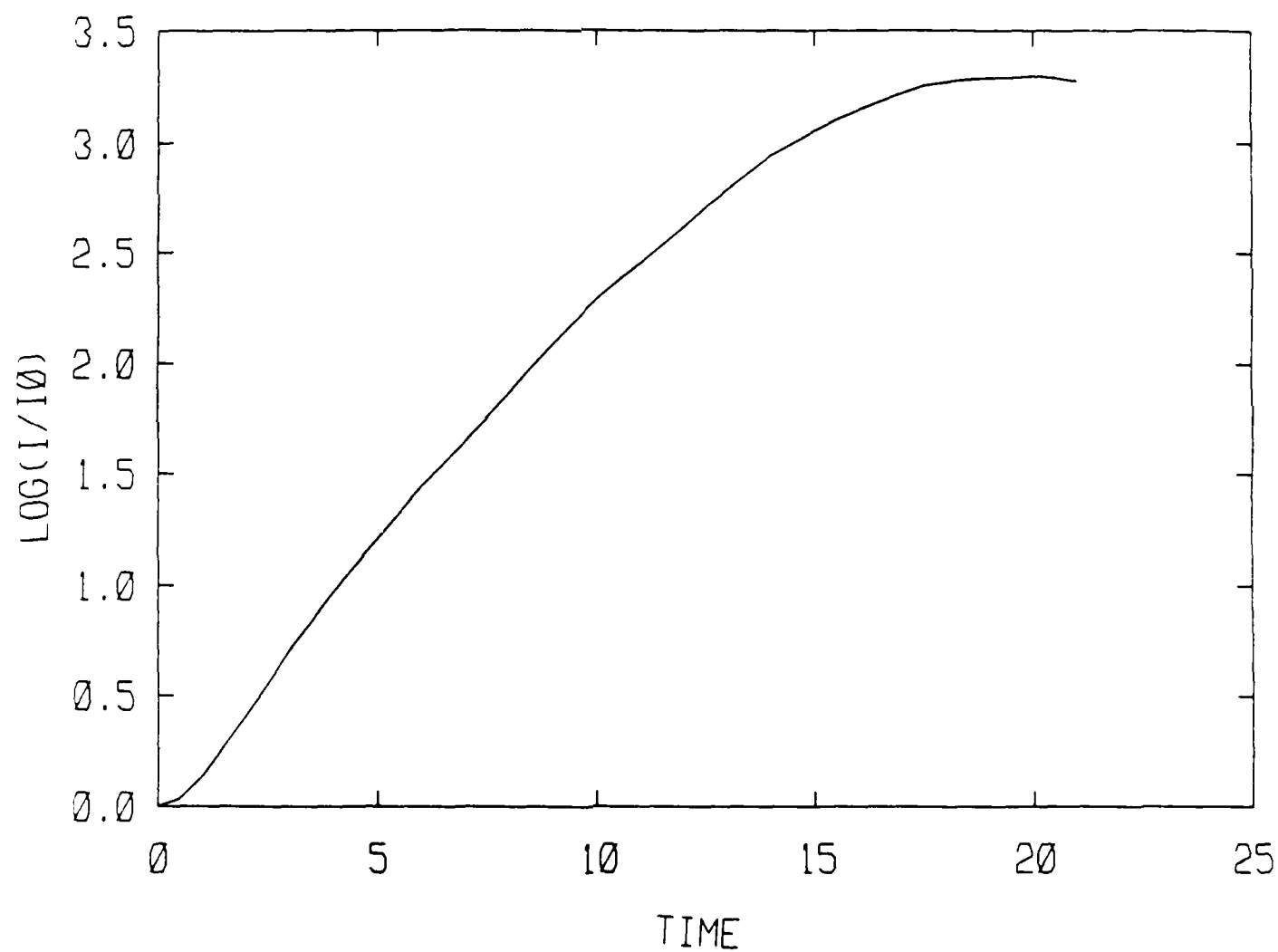
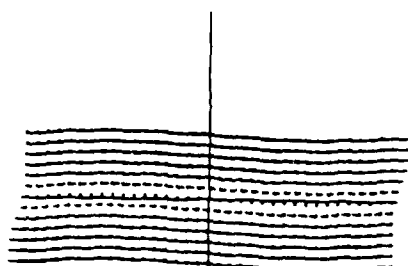
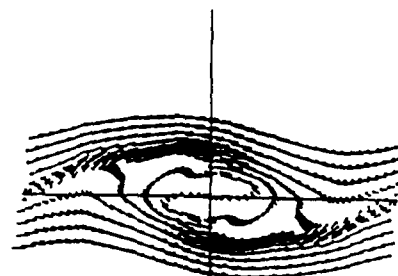


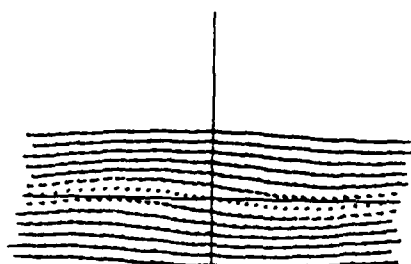
Fig. 1



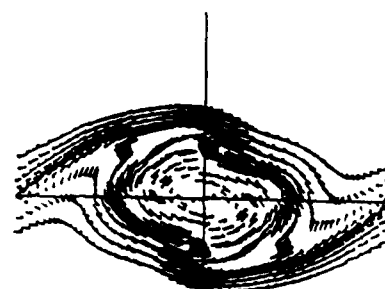
TIME = 0.00 | ELEMENTS = 455



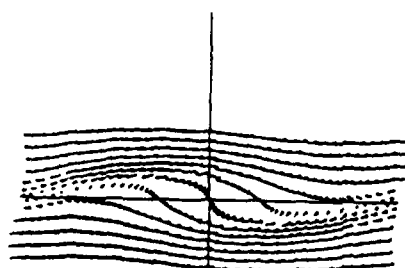
TIME = 12.00 | ELEMENTS = 593



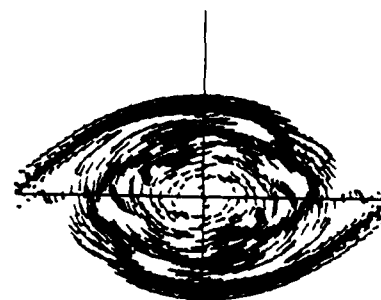
TIME = 4.00 | ELEMENTS = 455



TIME = 16.00 | ELEMENTS = 893



TIME = 8.00 | ELEMENTS = 501



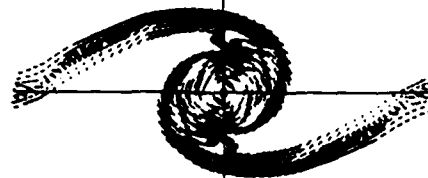
TIME = 20.00 | ELEMENTS = 1315

ORDER OF INTEGRATION=2 ORDER OF CORE=2

LAYER=13 BLOB/LAYER=35 SIGB=0.375 THICKNESS=3.600 AMPL.=0.0100 U.LENGTH=10.50



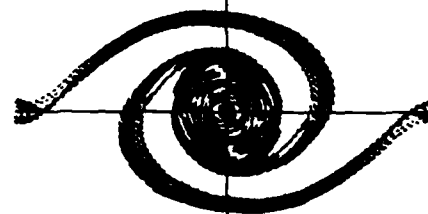
TIME = 0.00 ELEMENTS = 540



TIME = 24.00 ELEMENTS = 1172



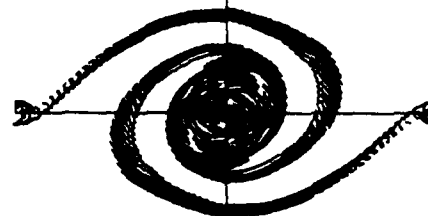
TIME = 8.00 ELEMENTS = 540



TIME = 32.00 ELEMENTS = 2352



TIME = 16.00 ELEMENTS = 682

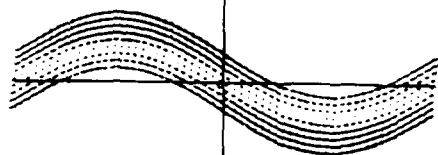


TIME = 34.00 ELEMENTS = 2718

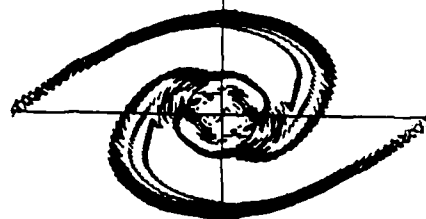
ORDER OF INTEGRATION=2 ORDER OF CORE=2

LAYER= 9 BLOB/LAYER=00 SLOB=0.500 THICKNESS=3.520 AMPL.=0.0100 U.LENGTH=25.40

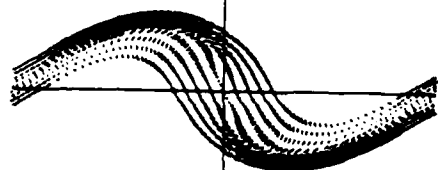
Fig. 1



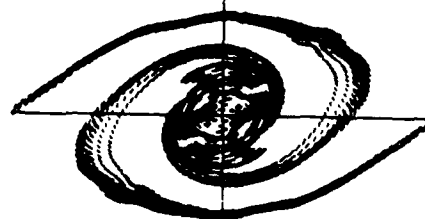
TIME = 0.00 ELEMENTS = 540



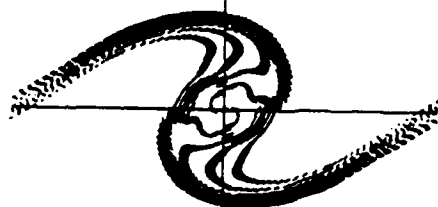
TIME = 18.00 ELEMENTS = 1620



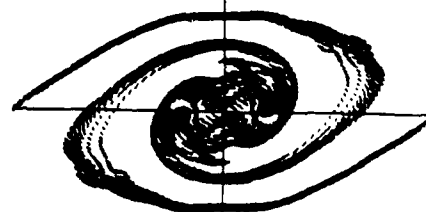
TIME = 8.00 ELEMENTS = 732



TIME = 24.00 ELEMENTS = 2649



TIME = 12.00 ELEMENTS = 1072



TIME = 26.00 ELEMENTS = 3150

ORDER OF INTEGRATION=2 ORDER OF CORE=2

LAYER= 9 BLOB/LAYER=60 SIG=0.500 THICKNESS=3.520 AMPL.=0.1000 W.LENGTH=26.40



TIME = 0.00 ELEMENTS = 810



TIME = 24.00 ELEMENTS = 1123



TIME = 8.00 ELEMENTS = 810



TIME = 32.00 ELEMENTS = 2143



TIME = 16.00 ELEMENTS = 810

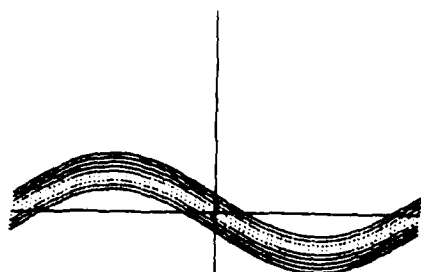


TIME = 34.00 ELEMENTS = 2556

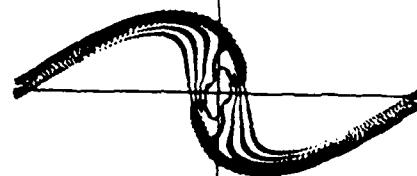
ORDER OF INTEGRATION=2 ORDER OF CORE=2

LAYER= 9 BLOB/LAYER=90 SIGB=0.500 THICKNESS=3.520 AMPL.=0.0100 W. LENGTH=39.60

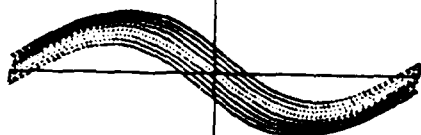
Fig. 17



TIME = 0.00 ELEMENTS = 810



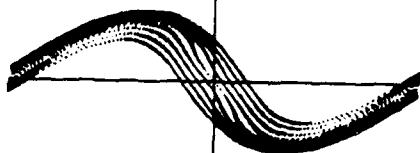
TIME = 12.00 ELEMENTS = 1268



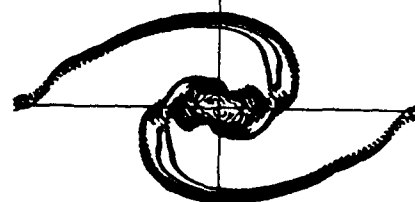
TIME = 4.00 ELEMENTS = 878



TIME = 16.00 ELEMENTS = 1636



TIME = 8.00 ELEMENTS = 1092

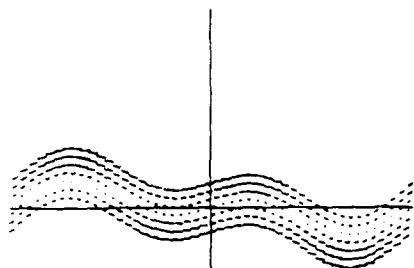


TIME = 20.00 ELEMENTS = 2172

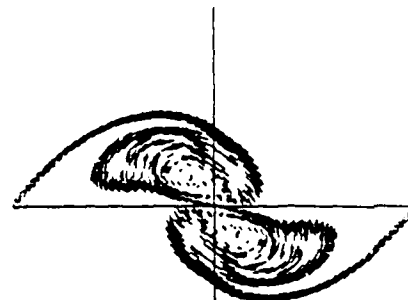
ORDER OF INTEGRATION=2 ORDER OF CORE=2

LAYER= 9 BLOB/LAYER=90 SLOB=0.500 THICKNESS=3.520 AMPL.=0.1000 W.LENGTH=39.60

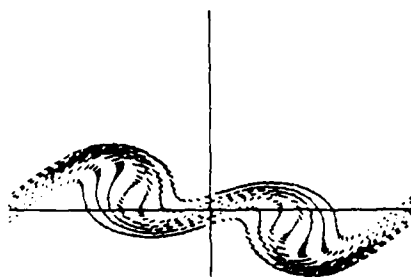
Fig. 15



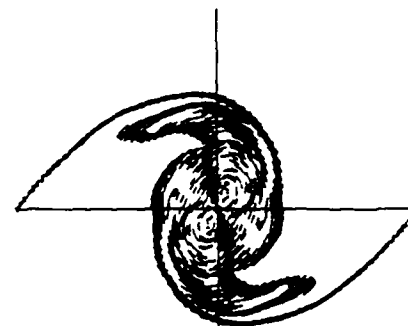
TIME = 0.00 ELEMENTS = 336



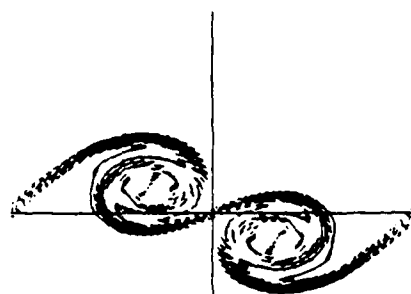
TIME = 15.00 ELEMENTS = 1237



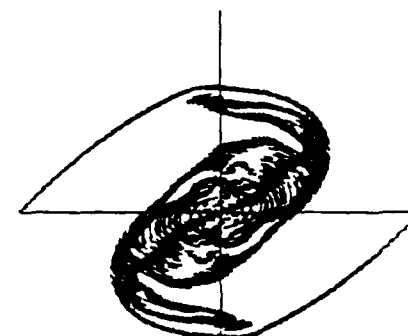
TIME = 5.00 ELEMENTS = 483



TIME = 20.00 ELEMENTS = 1891



TIME = 10.00 ELEMENTS = 796



TIME = 25.00 ELEMENTS = 2914

ORDER OF INTEGRATION=4 ORDER OF CORE=2

LAYER= 7 BLOB/LAYER=48 SLOB=0.000 THICKNESS=3.300 AMPL.=0.1000 W.LENGTH=13.20

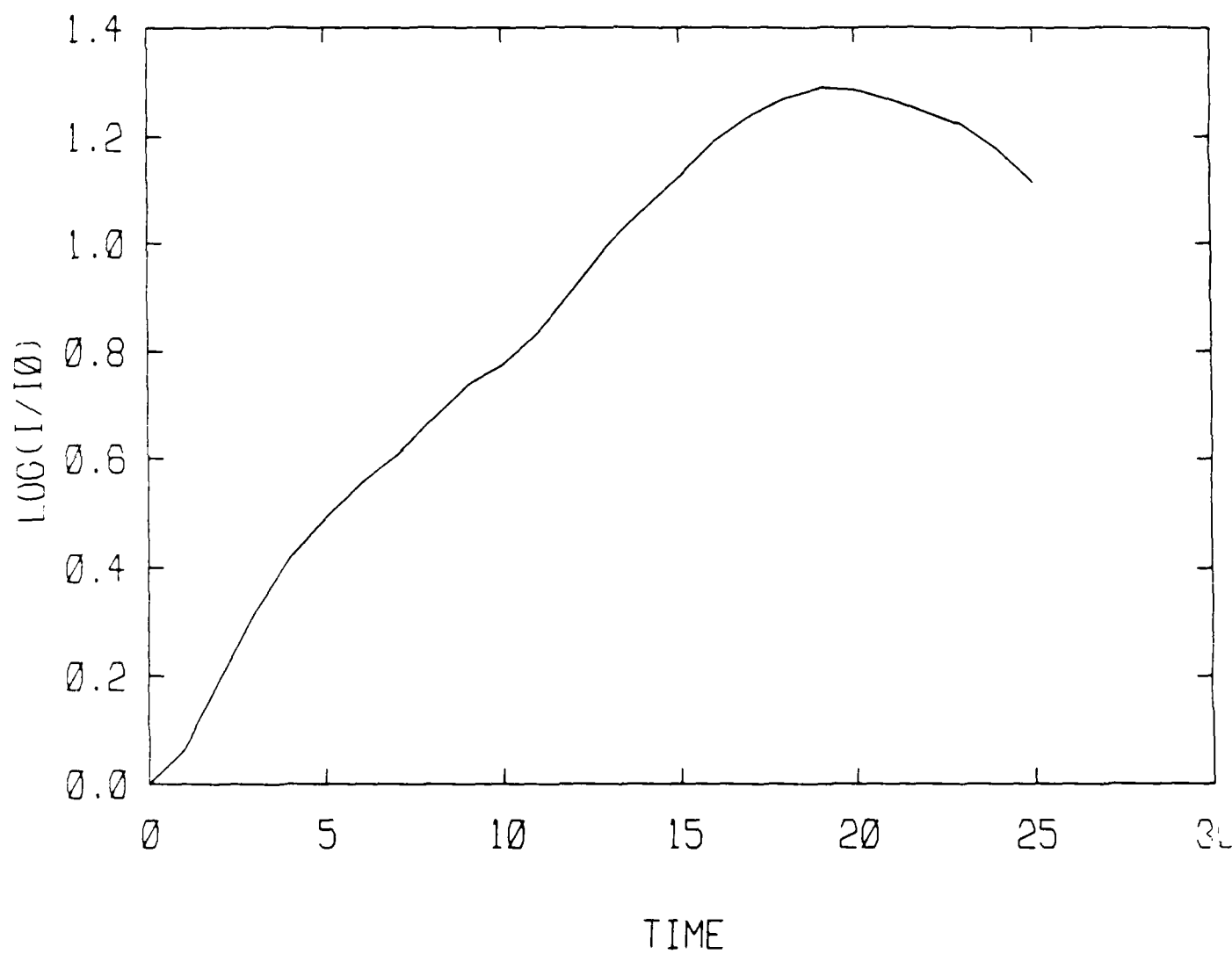
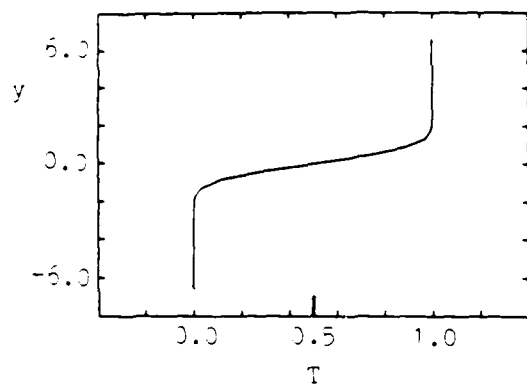
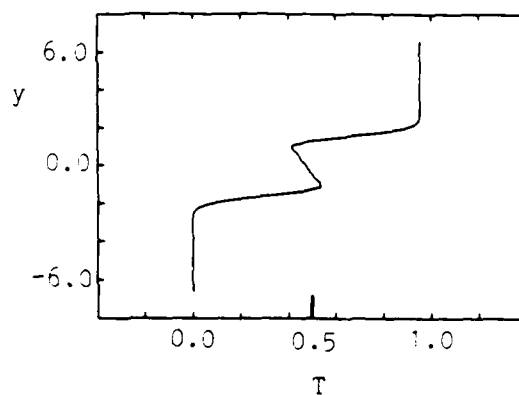


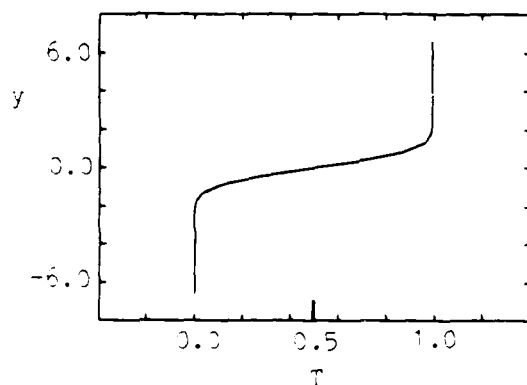
Fig. 1 -



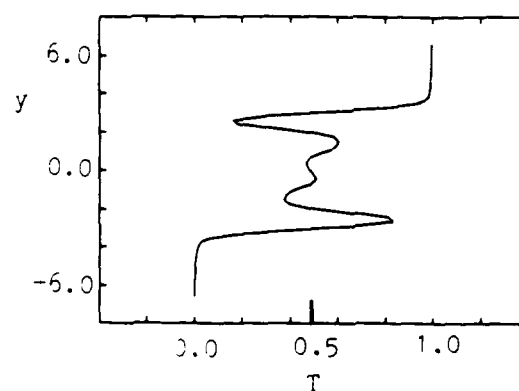
TIME = 0.0000



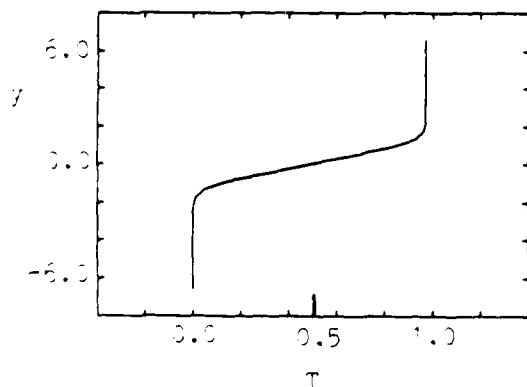
TIME = 24.0001



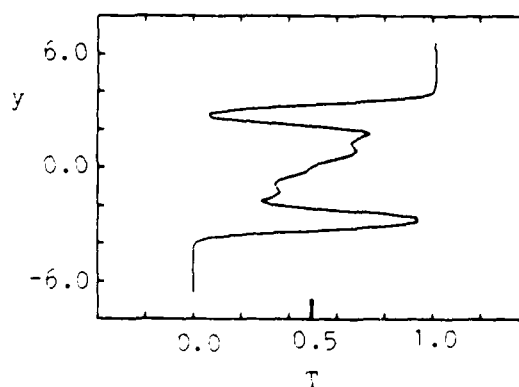
TIME = 8.0000



TIME = 32.0001



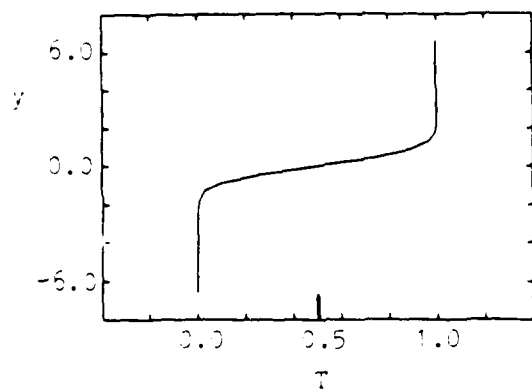
TIME = 16.0000



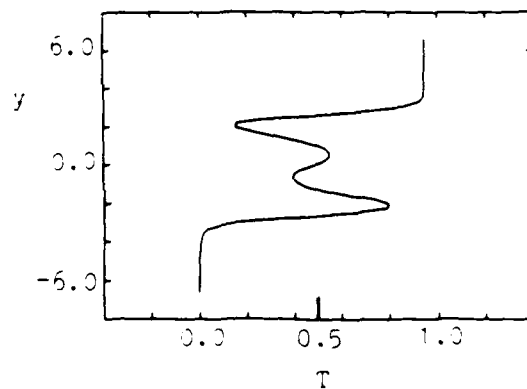
TIME = 35.0000

ORDER OF INTEGRATION=1 ORDER OF CORE=2

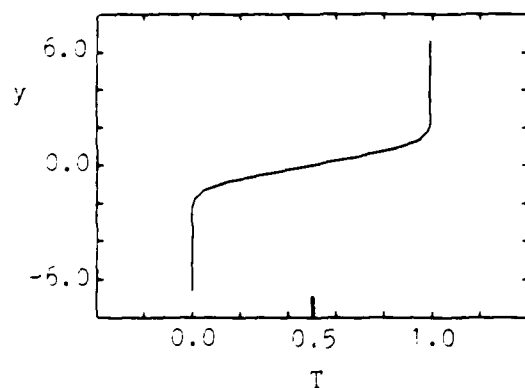
LAYER=13 BLOB/LAYER=44 SIGB=0.375 THICKNESS=3.000 AMPL.=0.0010 W.LENGTH=13.20



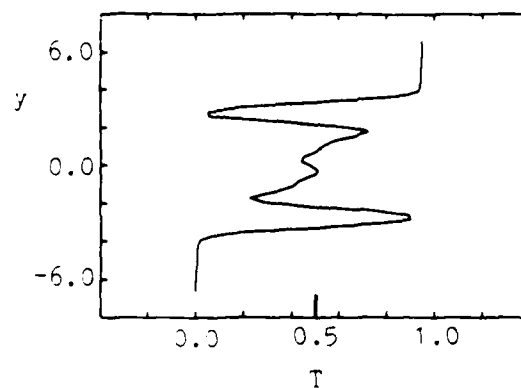
TIME = 0.0000



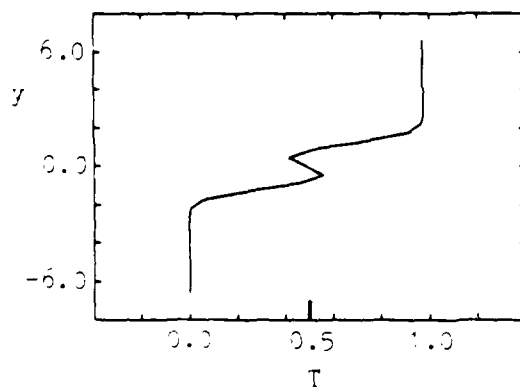
TIME = 18.0000



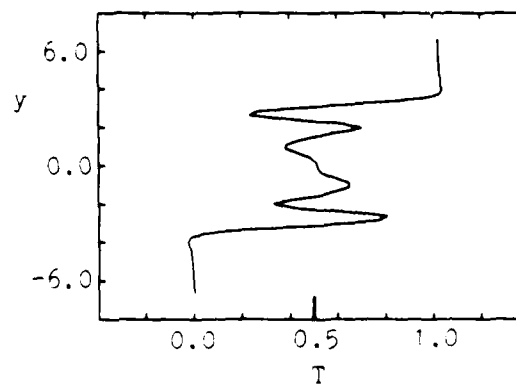
TIME = 6.0000



TIME = 24.0001



TIME = 12.0000

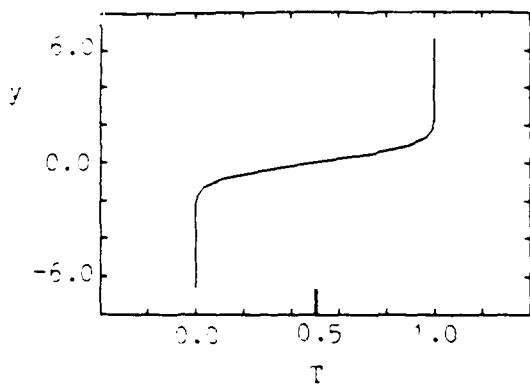


TIME = 28.5001

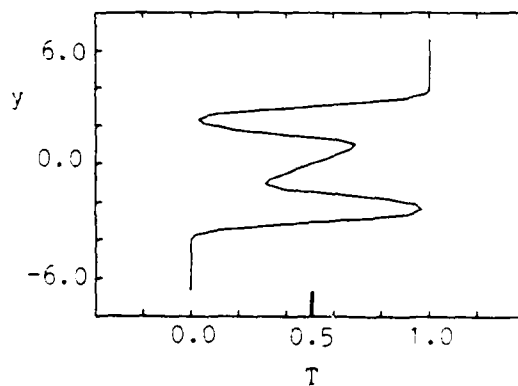
ORDER OF INTEGRATION=2 ORDER OF CORE=2

LAYER=11 BLOB/LAYER=40 SIGB=0.400 THICKNESS=3.300 AMPL.=0.0100 U.LENGTH=13.20

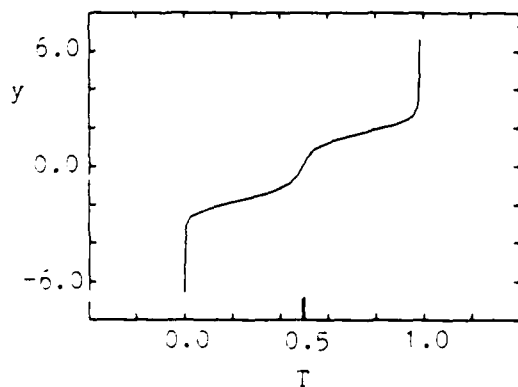
Fig. 1



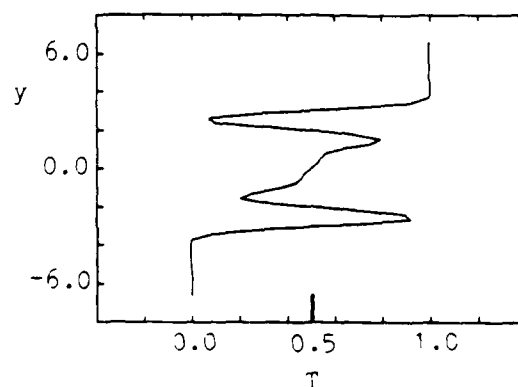
TIME = 0.0000



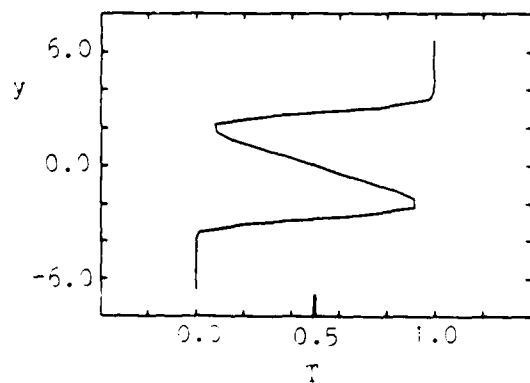
TIME = 12.0000



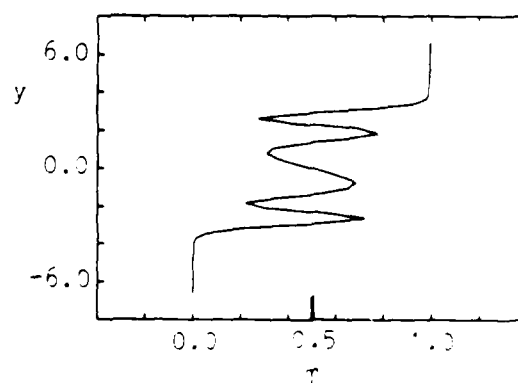
TIME = 4.0000



TIME = 16.0000



TIME = 8.0000



TIME = 20.0000

ORDER OF INTEGRATION=2

ORDER OF CORE=2

MESH=21x21

STATION=22

LAYER=11

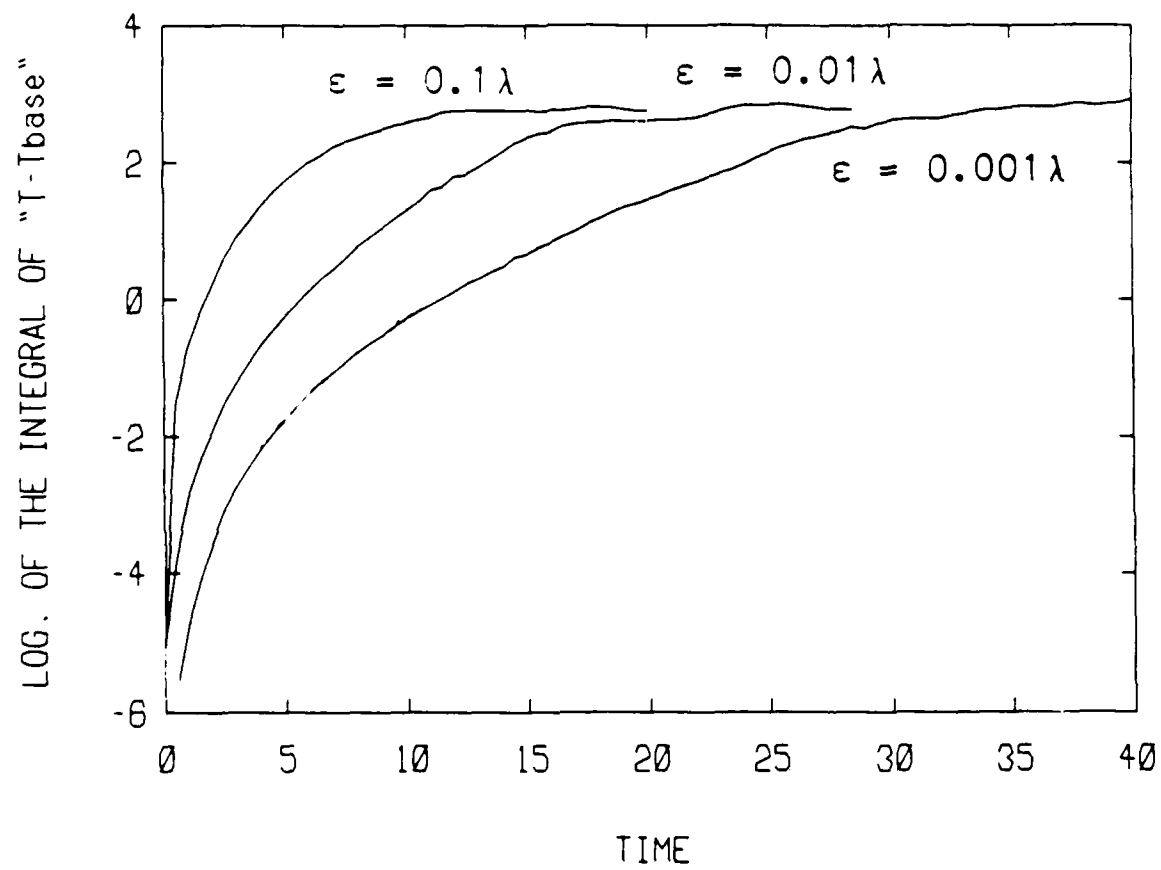
BLOB/LAYER=40

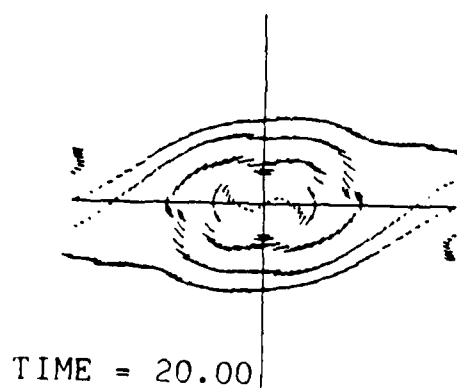
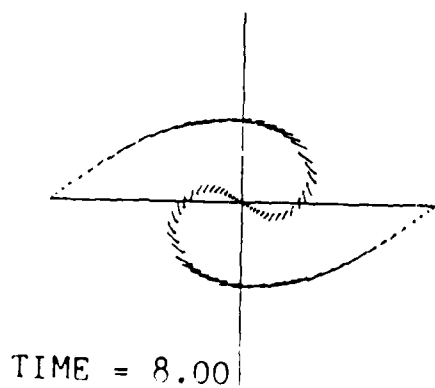
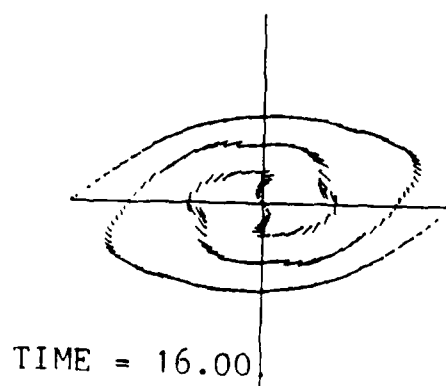
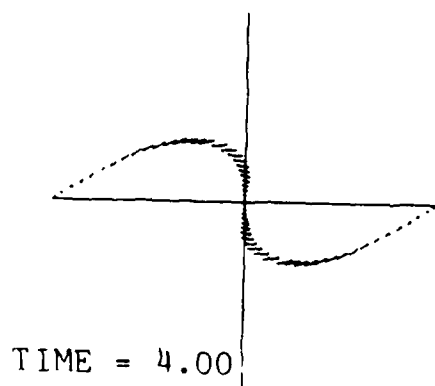
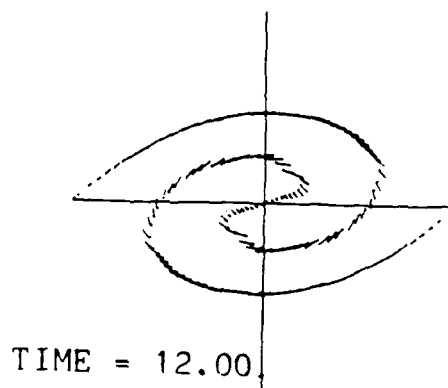
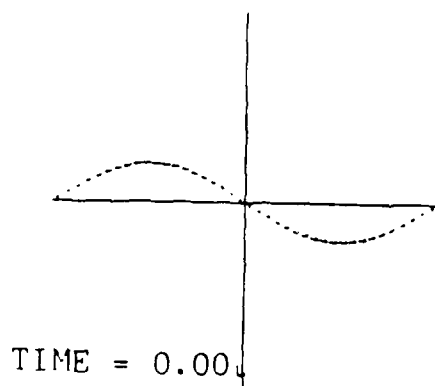
SIGB=0.400

THICKNESS=3.300

AMPL.=0.1000

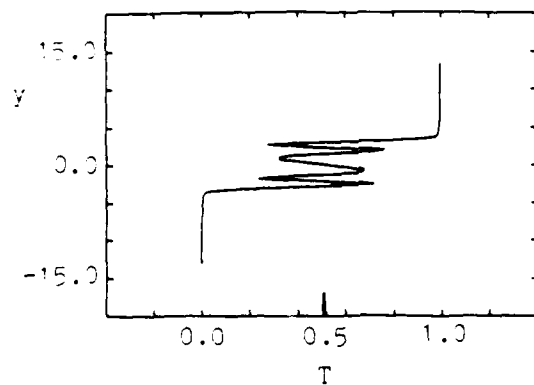
W.LENGTH=13.20



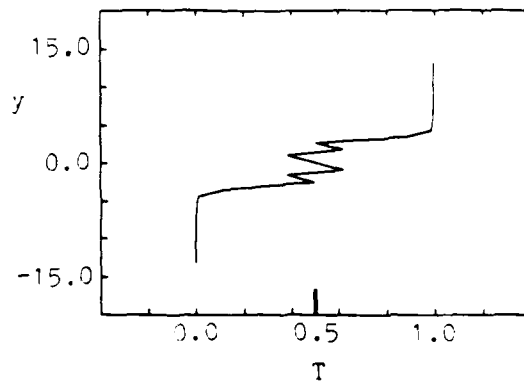


ORDER OF INTEGRATION=2 ORDER OF CORE=2 MESH=21x21 STATION=22
 LAYER=11 BLOB/LAYER=40 SIG=0.400 THICKNESS=3.300 AMPL.=0.1000 W. LENGTH=13.20

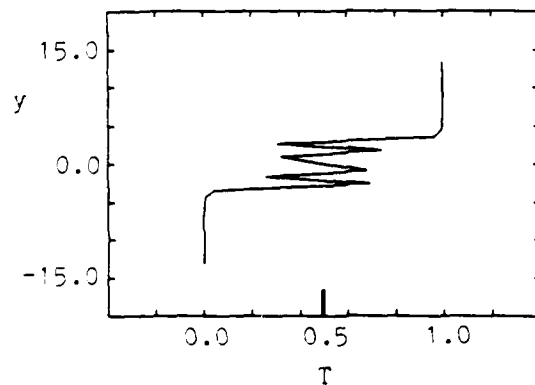
Fig. 11



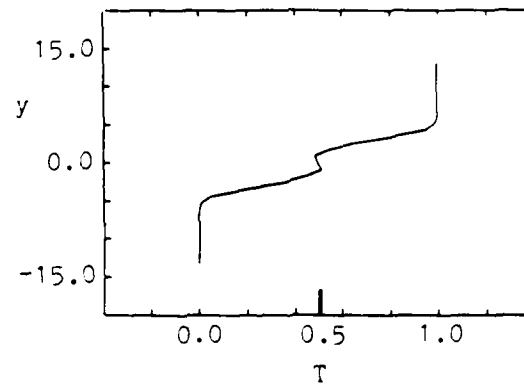
$\alpha = 0.00000$



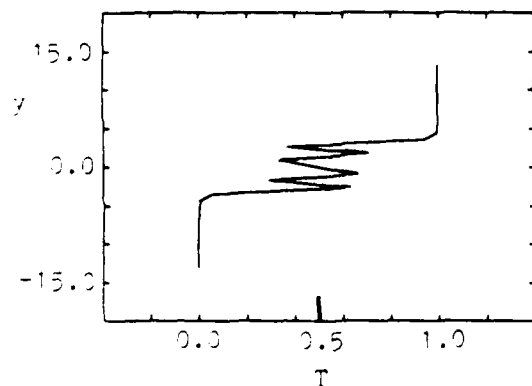
$\alpha = 0.00100$



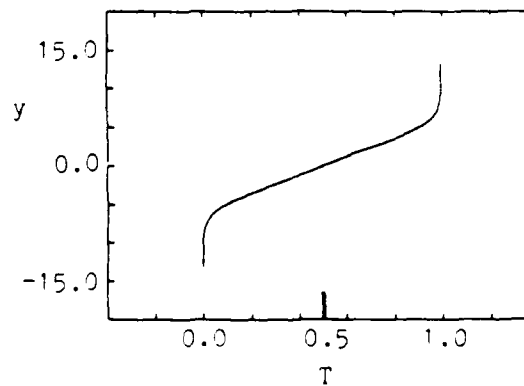
$\alpha = 0.00001$



$\alpha = 0.01000$



$\alpha = 0.00010$



$\alpha = 0.10000$

ORDER OF INTEGRATION=2 ORDER OF CORE=2

LAYER=11 BLOB/LAYER=40 SIGB=0.400 THICKNESS=3.300 AMPL.=0.1000 W.LENGTH=13.20

Figure 11

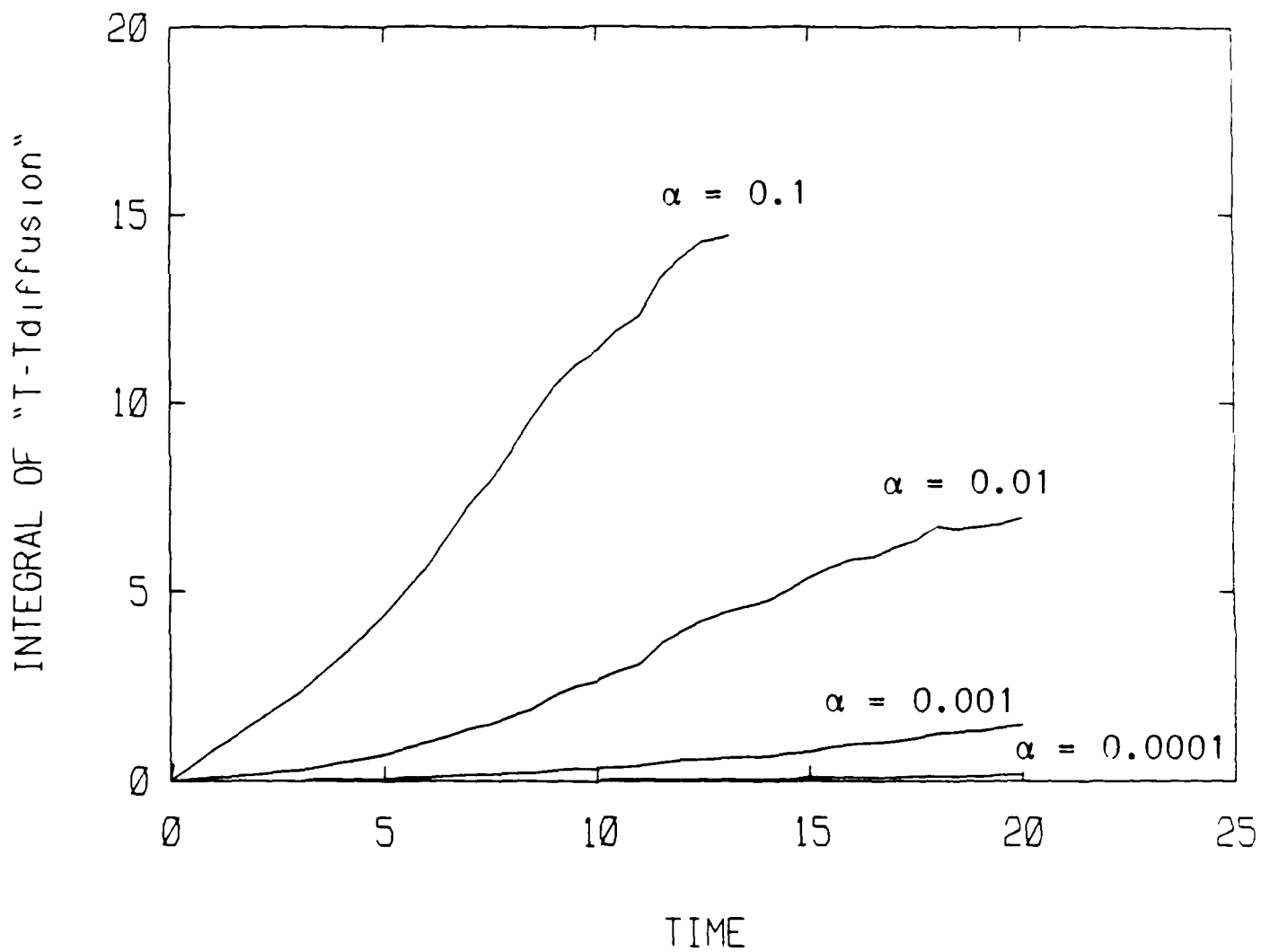


Fig. 2

Appendix II

The paper on "Numerical simulation of a reacting shear layer using the transport element method" describes the formulation of the vortex element method and the transport element method for a chemically reacting flow with finite rate of heat release governed by Arrhenius chemical kinetics. The application of the method to a non-reacting spatially developing shear layer and a reacting temporally evolving shear layer are presented.

AIAA'87

AIAA-87-1718

**Numerical Simulation of a Reacting
Shear Layer Using the
Transport Element Method**

**A.F. Ghoniem, G. Heidarinejad, A. Krishnan
Massachusetts Institute of Technology
Cambridge, MA 02139**

**AIAA/SAE/ASME/ASEE 23rd Joint
Propulsion Conference**

June 29-July 2, 1987/San Diego, California

**For permission to copy or republish, contact the American Institute of Aeronautics and Astronautics
1633 Broadway, New York, NY 10019**

COMBUSTION SIMULATION OF A REACTING SHEAR LAYER USING
THE TRANSPORT ELEMENT METHOD

Ahmed F. Ghoniem*, Ghassan Hejrannejad**, and Anantha Krishnan***

Department of Mechanical Engineering
Massachusetts Institute of Technology
Cambridge, MA 02139

ABSTRACT

The transport element method, a numerical scheme that combines the vortex method with the Lagrangian transport of scalar gradients, is used to study the evolution of combustion in a reacting shear layer. The scheme is based on the accurate discretization of the vorticity and the scalar gradient distributions into a number of Lagrangian finite elements. The elements move along material lines, and change their shape or configuration to accommodate the distortions induced by the strain field. Their source strengths vary with the chemical reaction rate.

Premixed combustion at finite activation energy, moderate chemical kinetic rates and finite diffusivities is considered. Processes that lead to burning enhancement or flame extinction are analyzed. It is found that stretch can accelerate burning when chemistry is fast by enlarging the reaction surface and increasing the mass diffusion fluxes into the burning zone, resulting in burning rates which are proportional to the square of the strain rate. However, at slower chemistry, stretch leads to flame blowout when chemical heat release cannot compensate for the heat flux out of the reaction zone and mass flux into the reaction zone.

1. INTRODUCTION

Turbulent combustion is governed by the complex interaction between convective and diffusive transport processes, chemical reaction and heat release. Chemical reactions are strong nonlinear functions of temperature and species concentrations, and thus their rates are critically dependent on transport fluxes. Meanwhile, rates and magnitudes of heat release, associated with the chemical oxidation of practical fuels, are large enough to affect the transport phenomena. Understanding the outcome of these interactions is important to achieve better control of burning processes in combustion systems. It is the objective of this work to: (i) develop numerical models capable of predicting turbulent combustion processes; (ii) identify the most important modes of turbulent combustion

interactions; and (iii) elucidate the surface nature of some of these interactions. We confine our attention to shear layers since they are relatively simple to analyze, and since they represent a generic model for many reacting flows.

Turbulent combustion has been the subject of extensive experimental, theoretical, and numerical investigations over the years¹. However, many of its fundamental processes remain unclear. On the one hand, progress in phenomenological turbulent combustion models, based on the closure of a system of averaged transport equations which describe the statistical behavior of the aerothermodynamic variables, has made it possible to produce results which agree with experimental measurements. On the other hand, since most of the interesting dynamics of turbulence-combustion interactions are modeled *a priori* in these models, solutions do not provide a better understanding of the phenomena and are limited to producing results for particular systems.

Two problems have been identified as most challenging in the study of turbulence in reacting flow: (i) the source of the statistical correlations between fluctuating quantities; and (ii) the nature of the source terms in the energy and species conservation equations. In turbulent shear layers, the first problem is complicated by the presence of large scale structures that cannot be modeled by gradient-diffusion type terms. The second problem stems from the fact that chemical reactions are strongly affected by fluctuations in local variables in a highly nonlinear way, especially the most common Arrhenius type. In the following, the two issues are discussed in more detail.

Time-resolved flow visualization and instantaneous point measurements in nonreacting and reacting shear layers have revealed the existence of large scale periodic turbulent structures for a long distance downstream the separation point^{3,4,5,6}. It has been shown experimentally, and supported by numerical studies, that these structures appear via the Kelvin-Helmholtz instability of the vorticity layer which forms between two initially-separated streams⁷. By a different mechanism, the subharmonic instability, these structures persist through successive pairings, thus maintaining the periodicity downstream though at different frequencies. Qualitatively, it is known that the role these structures play in the mixing process is to engulf, then stretch layers of fluid to scales where molecular diffusion is effective. The two processes, which have been called entrainment, may be the bottleneck to mixing if the rate of molecular diffusion is high due to

Copy rights © by A. F. Ghoniem. Published by the American Institute of Aeronautics and Astronautics with permission.

* Associate Professor, Aeronautics and Astronautics.
** Research Assistant.
*** Research Assistant.

small scale turbulence². However, available results that support or repudiate these effects are not yet available.

The importance of these results in the context of investigating turbulence-combustion interactions is now the existence of different scales can be properly represented. Even though gradient diffusion models, which assume that only local conditions can affect turbulence, may provide an adequate description of the small diffusive scales, they do not contain enough information to identify the large convective scales. The latter is a feature of the unsteady flow field and depends strongly on the initial and boundary conditions. Thus, it must be resolved by solving the unsteady unaveraged equations using accurate schemes, while the effect of the small scales, for the sake of economy, may be modelled based on an understanding of the "substructural phenomena."

Since chemical reaction depends on the rate of molecular mixing which, as previously described, is a consequence of entrainment by the large scales and diffusion at the small scales, it is important that these two processes be represented accurately. Overestimating the rate of mixing by using a turbulence model in the work of Walker resulted in erroneously predicting the temperature by 100% in the diffusion flame of C_2H_2 . This could have been prevented if the appropriate rate of entrainment had been allowed to control the rate of mixing. More recently studies have confirmed these findings^{11,12}. The solution algorithm must, therefore, recognize the presence of large scale convective structures as well as small scale diffusive eddies. It should also give careful consideration to their continuous interactions. Since a typical size of a large scale eddy is on the order of magnitude of the thin, but finite vorticity layers, they can only be resolved if the unsteady unaveraged equations are integrated using accurate numerical methods. These methods must be non-diffusive, i.e., they should not dissipate the flow energy by distributing it on large cells.

Resolving the unsteadiness of the flows is particularly important in combustion modelling since chemical source terms are strong nonlinear functions of the instantaneous values of the temperature and species concentrations, as exemplified by the Arrhenius form, and their values depend on the fluctuations of the aerothermodynamic variables and to a less extent, on the mean values. Moreover, since chemical reactions occur on the molecular levels and are time-dependent processes, using averaged modelled equations in which mixing is described by inaccurate mean fluctuations is not expected to retain much of their physics. A very important aspect of combustion is that the chemistry is a Lagrangian process which proceeds as fluid elements move. Averaging this intrinsically unsteady process removes information that cannot be recovered using mean values and a few moments.

Clearly, a better description of chemical reaction in an unsteady flow field could be based on the Lagrangian formulation of the conservation equations since it preserves its nature. A numerical scheme which is based on the Lagrangian description of the flow field should then lead to more accurate results if fine resolution is achieved. The work which is described here is based on numerical simulation of the conservation

equations in Lagrangian form. The numerical algorithms have been conceived from a physical perspective. However, mathematically the algorithms have been constructed to address issues of accuracy and convergence to the Navier-Stokes equations which more is underway^{13,14,15}.

Numerical simulation of turbulent combustion attempts to minimize the use of phenomenological modelling. Thus, the solution can tell us and understand some of the important mechanisms of turbulence-chemistry interactions. Furthermore, since the instantaneous behavior of the variables are known at all points and at all times, accurate simulations offer a method of probing the flow when experimental techniques are not available. Ultimately, after validating and verifying the results against experimental measurements, initial predictions will be possible. Finally,

difference methods^{14,15}, spectral methods¹⁶, and vortex methods¹⁷ have been utilized in numerical simulation of nonreacting shear layers. Some have

also been extended to reacting shear layers^{18,19}. The first two methods are based on the Eulerian description of the flow field using grids to discretize the derivatives of the aerothermodynamic variables, or to expand these variables in harmonic functions, respectively.

Vortex methods, which have been grid free, Lagrangian schemes, are used to obtain solutions at high Reynolds number for spatial layers and recirculating flows. These methods optimize the computational efforts by distributing computational elements around regions of high vorticity^{20,21}.

However, five factors limited their utilization to study combustion problems: (1) Eulerian methods were used to solve the energy and species conservation equations which seemed, in some sense, to defeat the purpose of using vortex methods to simulate the hydrodynamic

field²²; (2) the limit of fast chemistry did not allow realistic finite rate chemical kinetics to be part of the model²³; (3) vortex methods, while maintaining reasonable accuracy in the majority of the field, lost resolution within the part of the field where the strain field is very strong²⁴; (4) vortex methods were limited to handling incompressible flows, thus the models neglected the distributed expansion and the non-baroclinic torque generated during combustion; and (5) three-dimensional effects were not included and appropriate representation of small scales were not implemented^{28,29}.

In this article, we will introduce the transport element method. When applied to obtain a solution of the vorticity transport equation, the method becomes the vortex element method, in which particles are treated as finite elements that accurately discretize the vorticity field and change their shape or configuration to accommodate distortions of the vorticity distribution caused by the development of strong strain fields. The transport element method extends the concepts of the vortex element method to obtain solutions of a reacting scalar conservation equation in terms of moving Lagrangian gradients. Both schemes are formulated to preserve the effect of compressibility at low Mach number. The transport element method is then applied to study the evolution of combustion in a reacting shear layer in premixed gases. Results are used to

investigate different modes of turbulent combustion interactions in a shear layer, and to study the outcome of these interactions in different regimes of the governing parameters. Processes of burning enhancement and flame extinction via the effect of stretch are analyzed in detail in light of the numerical results.

II. FORMULATION

The non-dimensional form of the conservation equations governing a two-dimensional, unsteady reacting flow is summarized in Table I. We assume that initially, and at all times at the inlet section, a premixed reactant R and a product P are present at given concentrations c_{R0} and c_{P0} in the top high speed and bottom low speed streams, U_1 and U_2 , respectively. For computational simplicity, chemistry is assumed to be governed by a single step irreversible Arrhenius reaction of order n . Adding more steps to the chemical kinetics scheme will require integrating more species conservation equations. The Mach number is assumed to be small, which leads to the following simplifications in the governing equations: (1) pressure variation due to the flow field is small compared with the total pressure, and hence neglected in the equation of state; and (2) spatial variations of pressure and energy dissipation due to viscosity are neglected in the energy equation. This isobaric approximation allows partial decoupling of continuity, momentum and energy equations so that they can be integrated sequentially instead of simultaneously.^{32,33} Meanwhile, acoustic interactions are removed. We assume that the reactant and products behave as perfect gases with equal molecular weights and specific heats, and that thermal and mass diffusivities are constants, but not necessarily equal. Moreover, the Reynolds number is high and the effect of viscosity is neglected.

TABLE I GOVERNING EQUATIONS

REACTION	$R \xrightarrow{k} P$	(1)
VELOCITY	$\mathbf{u} = \mathbf{V}_t + \nabla \psi + \mathbf{u}_p$	(2)
EXPANSION	$\nabla^2 \psi = \frac{1}{\rho} \frac{\partial \rho}{\partial t}$	(3)
ROTATION	$\nabla^2 \zeta = -\omega \times \mathbf{u}$	(4)
VORTICITY	$\frac{d\zeta}{dt} + \frac{1}{\rho} \nabla \rho \cdot \nabla \zeta = -\frac{1}{\rho} \nabla \rho \cdot \nabla \zeta + \frac{du}{dt}$	(5)
ENERGY	$\frac{dT}{dt} = \frac{1}{F_e} \nabla^2 T + A_f Q \kappa$	(6)
REACTANTS	$\frac{dc}{dt} = \frac{1}{F_e L_e} \nabla^2 c - A_f \kappa$	(7)

$$\text{Eq. (1)} \quad \frac{dc}{dt} = \frac{1}{F_e L_e} \nabla^2 c - A_f \kappa$$

$$\text{Eq. (2)} \quad \mathbf{u} = \frac{1}{\rho} \nabla \psi + \mathbf{u}_p$$

where $d/dt = \partial/\partial t + \mathbf{u} \cdot \nabla$ is the Lagrangian derivative along a particle path. The definition of symbols is as follows: $\mathbf{u} = (u, v)$ is velocity, $\mathbf{x} = (x, y)$ and x and y are the streamwise and the cross-stream directions, respectively, ψ is the velocity potential, $\zeta = \zeta(x, y, t)$ is the vorticity, $\nabla = (\partial/\partial x, \partial/\partial y)$ is the gradient function defined such that $\mathbf{u} = \nabla \times \psi = (-\partial\psi/\partial y, \partial\psi/\partial x)$, and $\mathbf{u}_p = \nabla \times \mathbf{u}_p$ is the potential velocity, $\nabla \cdot \mathbf{u}_p = 0$, added to satisfy the normal boundary condition across the boundary of the domain. c is the concentration per unit mass, T is temperature, ∇ and ∇^2 are the gradient and Laplacian operators, respectively, $A_f \kappa$ is the rate of formation of products per unit mass per unit time. Variables are non-dimensionalized with respect to the appropriate combination of the velocity of the high speed stream U_1 , the stream height h , the free stream concentration of R , c_{R0} , and the free stream temperature of the reactants at $x = 0$, T_{R0} . E_a is the activation energy, non-dimensionalized with respect to $R_g T_{R0}$, R_g being the gas constant. Q is the enthalpy of reaction, non-dimensionalized with respect to $C_p T_{R0}$, where C_p is the specific heat at constant pressure, $Pe = U_1 h / \alpha$ is the heat Peclet number, where $\alpha = \kappa / C_p$ is the thermal diffusivity, taken as a constant, $A_f = A_f c_{R0} h U_1$ is the non-dimensional frequency factor of the chemical reaction rate constant. The Damköhler number $Da = A_f \kappa / c_{R0} U_1$, c_{R0} and T_{R0} corresponding to conditions of maximum reaction rate, is the ratio of flow time to chemical time. $Le = \alpha / D$ is the Lewis number, $Pe = U_1 h / D$ is the mass Peclet number, and D is the mass diffusivity. n is the order of the reaction. Equation (2) is the decomposition of the velocity field into an irrotational and a solenoidal component. Eq. (3) is obtained by substituting \mathbf{u} into the continuity equation and using $\rho = \rho(T) = \text{constant}$ since the flow is unconfined and is at low Mach number. Equation (5) is obtained by taking the curl of the momentum equation of an inviscid flow and using $\nabla \rho = -\rho \nabla \ln T$ to substitute for the pressure gradient. This allows the integration of the equations without explicitly computing the pressure distribution. Equations (6)-(8) are the conservation of energy and species, respectively, for a reacting mixture at finite thermal and mass diffusivities. The equations form a five-parameter system Pe, Le, Da, Q and T_{R0} . The properties of the solution and the characteristics of the interaction between the flow field and the chemical reaction depend on the values, or the combination of values, of the individual parameters. If the system is not adiabatic, i.e.,

$T_p = T_c$ while $T_p = T_c = 1$, one more parameter, such as T_p/T_c , must be specified in the formulation. The equations identify four different processes of turbulence-combustion interactions: (1) the generation of an irrotational velocity due to volumetric expansion as the temperature rises during heat release, $\nabla \cdot \mathbf{u}$, in Eqs. (2,3); (2) the generation of non-baroclinic vorticity due to pressure-density interactions during heat release, $\nabla p \times \nabla \rho$ in Eq. (5); (3) the advection and straining of the flame structure in Eqs. (6,7) and (5); and, (4) the inhomogeneity in the diffusive fluxes due to non-unity Lewis number in Eqs. (6) and (7).

111. NUMERICAL METHOD

111.1. THE VORTEX ELEMENT METHOD

An important step in improving the accuracy and extending the application of vortex schemes to flow fields that develop large strain rates, such as shear layers, is the vortex element method²⁷. In this method, the vorticity field is accurately discretized among finite elements that move along particle paths, or particles that transport finite elements of vorticity. The strain field is used to redistribute the vorticity among the computational elements as time progresses so that small scales generated by planar stretch can be captured by the computations. This allows accurate long-time computations after the strain field has developed. Capturing the strain field accurately is very important in turbulent flame computations since (1) it governs the mixing process, which occurs after the original fluid layers have been stretched to very small scales; and (2) it may lead to flame quenching, or to burning enhancement, due to the generation of strong gradients as will be shown in the results. In the following, we summarize the method and show how it can be extended to compute a compressible non-barotropic flow at low Mach number.

The vorticity field is initially discretized among vortex elements of finite structure. The distribution of vorticity associated with each element is described by a radially symmetric function, f_i , with a characteristic radius, δ_i , such that most, or all, of the vorticity is concentrated within $r < \delta_i$, where $r^2 = x^2 + y^2$. Vortex elements are initially distributed in the area where $|\omega| > 1$ such that the distance between neighboring elements is h in the two principal directions. The accuracy of the discretization depends on the choice of f_i , the value of h , and the ratio δ/h . The strength of the vortex element located at \mathbf{X}_i , denoted by ω_i , is obtained from the solution of the system of equations:

$$\omega(\mathbf{X}_i, 0) = \sum_{j=1}^N \omega_j \int_{\Omega} f_j(\mathbf{X}_i - \mathbf{X}_j) d\mathbf{X}_j \quad (10)$$

where $\omega(\mathbf{X}, 0)$ is the vorticity distribution at $t = 0$. Being a Taylor series expansion, it can be shown that $f_i(r) = \exp(-r^2/\delta^2)$ leads to a second-order discretization. We found that for accurate representation of the vorticity distribution, δ must be slightly larger than h , i.e., $\delta/h = 1.1$, and that h must be varied until

$|\Gamma - \Gamma_0| < \epsilon$ and $|\mathbf{u}(\mathbf{X}, t) - \mathbf{u}(\mathbf{X}, 0)| < \epsilon$, where Γ is the total circulation of the vorticity field, $\Gamma_i = \omega_i \pi \delta_i^2$ is the circulation of each individual vortex element, $|\cdot|$ denotes the second norm and ϵ is a small number.

For an incompressible flow, Eq. (10) leads to the Helmholtz theorem, which states that vorticity is constant along particle paths, i.e.,

$$\omega(\mathbf{X}, t) = \sum_{j=1}^N \Gamma_j f_j(\mathbf{X} - \mathbf{X}_j(t)) \quad (11)$$

and

$$\frac{d\mathbf{X}_i}{dt} = \mathbf{u}(\mathbf{X}_i, t), \quad (12)$$

where $\mathbf{X}_i(\mathbf{X}_i, 0) = \mathbf{X}_i$. To obtain the velocity field of a collection of vortex elements in the form of Eq. (11), we note that the stream function of a single vortex element is obtained by integrating Eq. (4). Using polar coordinates to integrate this equation for a vortex element placed at $\mathbf{x} = \mathbf{X}_i$, $\partial \psi_i / \partial r = -\kappa_i r / \delta_i^2$, where $\kappa_i = \Gamma_i / \delta_i^2$ for $r < \delta_i$. The velocity field of a single element is thus radially symmetric and $u_i = -\partial \psi_i / \partial y$. The velocity field induced by a distribution of finite-size vortex elements, of shape f_j and strength Γ_j , located at $\mathbf{X}_j, \mathbf{X}_j(t)$ is:

$$\mathbf{u}(\mathbf{x}, t) = \sum_{j=1}^N \Gamma_j \mathbf{K}_j(\mathbf{x} - \mathbf{X}_j(t)) \quad (13)$$

where $\mathbf{K}_j(\mathbf{x}) = -\frac{(\mathbf{y}_j - \mathbf{x})}{r^2} \times \frac{\mathbf{r}}{r}$ and

According to Eq. (13), vortex elements move at the local velocity at their centers. As time progresses, the distance between neighboring elements increases in the direction of maximum strain rate such that $\Delta_1 > h$, where Δ_1 is the distance in the direction of maximum strain defined as $\Delta_1 = (\Delta \mathbf{u} \cdot \mathbf{z}) / |\Delta \mathbf{u}|$ and \mathbf{z} is the difference operator between neighboring elements. This leads to a deterioration of the discretization accuracy since accurate discretization requires that $\delta > \Delta_1$. Thus, an algorithm must be used such that when $\Delta_1 > \delta$, where $\delta = 1.5$, a computational element is inserted at the midpoint between the original elements. The circulation of the new element, and that of the original two neighboring elements, is one third the sum of the circulation of the original two elements²⁷.

For compressible baroclinic flow, Eq. (10) shows that $d\omega/dt \neq 0$. Moreover, $\Gamma = \int \omega dA$, where A is the area, while $\int \rho dA = \text{constant}$. Thus, the circulation is constant along a particle path -- Kelvin theorem -- and Eqs. (11)-(14) can be used to compute the evolution of the vorticity and velocity field provided that Eq. (13) is used to compute the irrotational component of the velocity due to volumetric expansion, as will be shown in the next section. When $\nabla p \times \nabla \rho \neq 0$, the circulation of each vortex element must be updated each time step. Using the definition of the circulation in Eq. (5), we get:

$$\frac{d\mathbf{f}}{dt} = -\frac{1}{\rho} \nabla \cdot \mathbf{f} \times \frac{d\mathbf{u}}{dt} \quad (10)$$

Since $\mathbf{f} = \sum_{i=1}^N \mathbf{f}_i \delta(\mathbf{x} - \mathbf{x}_i)$ and, and $\mathbf{V}_i = \sum_{j=1}^N \mathbf{V}_j \delta(\mathbf{x} - \mathbf{x}_j)$ as will be shown in the next section, Eq. (10) can be written as:

$$\frac{d\mathbf{f}_i}{dt} = \frac{\mathbf{V}_i}{\rho_i} \times \frac{d\mathbf{u}_i}{dt} \quad (11)$$

where, according to the low Mach number approximation, $\mathbf{V}_i = -\nabla T_i$, while $\mathbf{V}_i = \sum_{j=1}^N \mathbf{V}_j \delta(\mathbf{x} - \mathbf{x}_j)$. In the next section, we will show how to compute \mathbf{V}_i , ρ_i , \mathbf{V}_i and T_i . Moreover, $(d\mathbf{u}_i/dt)$ is computed by numerically

differentiating the velocity of the vortex element using a high order formula. Equations (11) and (12) are integrated using a fourth order Runge-Kutta-Merson method with variable time step for error control.

3.1.1. THE TRANSPORT ELEMENT METHOD

Another important development in the application of particle methods to reacting flows is the formulation of the transport element method to compute the temperature and species concentration distributions in a Lagrangian

form. In this scheme, the gradient of the scalar field is discretized into a number of finite elements using Eq. (10) with w replaced by $\mathbf{g} = \nabla s$, where s is a generalized scalar, being either T or c . Like vortex elements, transport elements are distributed where $\nabla s > 0$ and are moved with the local velocity field with time. Thus, particles are used to transport scalar gradients. However, contrary to vorticity, scalar gradients are not conserved along particle paths, and should be modified according to the local strain and tilting of the material elements. The extension of this method to reacting flow will require changing the gradient transported by each element according to the reaction source term in Eqs. (6,7,8) in a way similar to changing the circulation with the non-baroclinic torque. Thus, the evolution of the chemical reaction with time will be computed in a Lagrangian frame of reference as the interacting species flow. In the following, we describe the conservative form of the transport element scheme and its extension to solve Eqs. (6,7,8).

Initially, the scalar gradient \mathbf{g} is discretized according to

$$\mathbf{g}(\mathbf{x}_j, t) = \sum_{i=1}^N \mathbf{g}_i(t) h_i^2 f_\delta(\mathbf{x}_j - \mathbf{x}_i) \quad (17)$$

where f_δ , δ and h have the same definitions as before, and should be chosen to satisfy the same requirements. To see how to transport the scalar gradient in a Lagrangian form, we start by the non-diffusive case. If s is a passive, non-diffusive scalar, the conservation equations for s and $\mathbf{g} = \nabla s$ are:

$$\frac{ds}{dt} = 0 \quad (18)$$

$$\frac{d\mathbf{g}}{dt} = \mathbf{g} \cdot \nabla \mathbf{u} - \mathbf{g} \times \omega$$

where $\omega = \nabla \times \mathbf{u}$. Thus, s remains constant along a particle path, while \mathbf{g} changes due to the stretching, tilting and rotation of the material line. While the scalar is conserved, the gradient is not, and care must be exercised in its transport. Clearly, if the material is experiencing a strong strain in the direction normal to the gradient, the value of \mathbf{g} must increase by the same amount as the stretch in the material element. This can be seen by writing the differential equation governing the evolution of a small material line $\delta \mathbf{l}$, centered around the point \mathbf{x} , and the equation governing the motion of a material point \mathbf{x} :

$$\frac{d}{dt} \delta \mathbf{l} = \delta \mathbf{l} \cdot \nabla \mathbf{u} \quad (19)$$

$$\frac{d\mathbf{x}}{dt} = \mathbf{u}(\mathbf{x}(t), t) \quad (20)$$

From Eqs. (19) and (20), it can be shown that $d\mathbf{g}/dt = \delta \mathbf{l} \cdot \nabla \mathbf{g} / \delta \mathbf{l} \cdot \delta \mathbf{l}$, where $\mathbf{g} = |\mathbf{g}|$. Thus, the gradient transported by an element that follows a particle path can be written as: $\mathbf{g}_i(t) = \delta \mathbf{s}_i / \delta \mathbf{l}_i(t) \cdot \mathbf{n}_i(t) h_i^2$, while $\mathbf{g} \cdot \mathbf{g} = n$ is the vector normal to $\delta \mathbf{l}$ (in a chemically reacting flow, it may also be $\delta s / \delta t$). For a graphical representation of this concept, see Fig. 1.

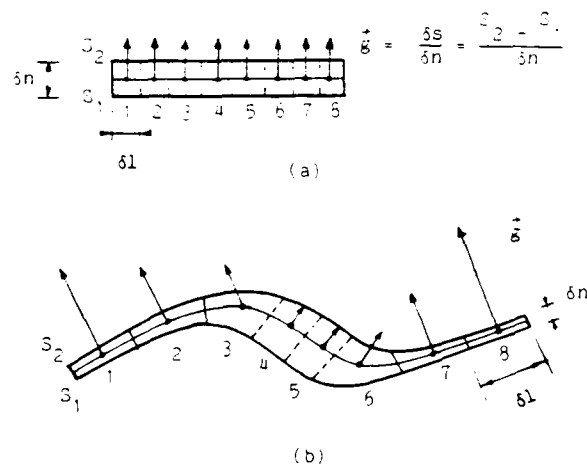


Figure 1. Schematic sketch showing the evolution of a material layer separating two values of the conserved scalar, s , and the associated scalar gradient, \mathbf{g} , under the effect of stretch.

Furthermore, the flux initialized by Eq. (17) becomes:

$$\mathbf{g}(\mathbf{x}, t) = \sum_{i=1}^N \mathbf{g}_i(t) h_i^2 f_\delta(\mathbf{x} - \mathbf{x}_i(t)) \quad (21)$$

where

$$\mathbf{g}_i(t) = \frac{\delta s_i}{\delta n_i} \frac{\delta \mathbf{l}_i(t)}{h_i^2} \cdot \mathbf{n}_i(t) \quad (22)$$

while

$$\frac{dx_i}{dt} = u_i x_i(t), \quad (14)$$

where $x_i, X_{i+1} = X_i$. δl_i is updated according to Eq. (10) and $n_i = \delta l_i / \delta l_{i-1} = 0$. Equation (13) is equivalent to updating g_i according to Eq. (12). However, the expression in Eq. (12) conserves the value of δs_i . Moreover, instead of integrating Eq. (21) to update δl_i , one can save computational effort by recalling that $\delta l_i(t) = (X_{i+1}(t) - X_{i-1}(t)) / 2$. Thus, it suffices to move the centers of the transport elements, while remembering the neighboring elements, to update δl_i . In this case, these elements are assumed to remain as straight lines.

Given the location and strength of the transport elements, the scalar concentration can be computed as follows. Since $\nabla s = g$, thus by taking the gradient $\nabla s = \nabla \cdot g$. The solution of this equation in an infinite domain can be written as: $s = \int \nabla \cdot g G dx$, where $G = -1/4\pi r$ in r is the Green function of the Poisson equation. This last equation shows that the transport elements act as sources of strength equal to the divergence of the scalar flux, $\nabla \cdot g$. Integrating by parts, one gets $s = \int g \cdot \nabla G dx$. Using Eqs. (12) and (13) for g , we get:

$$s(x, t) = \sum_{i=1}^N g_i(t) \cdot \nabla G_i(x - x_i(t)) / \kappa^2 \quad (14)$$

where

$$\nabla G_i = \frac{\partial G_i}{\partial x} = \frac{\partial}{\partial x} \left(\frac{1}{r} \right) = -\frac{x}{r^3} \quad (15)$$

where $\kappa = 1/\nu$ for $\nu = 1$, as defined before. If the distance between neighboring elements in the direction of principle strains exceeds a maximum distance δh , one element is inserted half-way between the two elements and the value of δl is adjusted for the three elements. A recombination procedure can also be implemented to curb the growth in the number of computational elements. The need for this insertion procedure is more apparent here since the magnitude of the gradient increases where the strain field is high; and to maintain the accuracy, more elements must be used to transport this gradient.

With finite diffusivity, the first term on the right hand side of Eqs. (6-8) should be simulated in the solution. In gradient form, the conservation equation can be written as:

$$\frac{dg_i}{dt} = -g_i \cdot \nabla u + \frac{1}{\kappa^2} \nabla^2 g_i \quad (16)$$

where κ is the molecular diffusivity, or the inverse of the Peclet number. At high speed flow, this is typically 10^{-3} - 10^{-5} . To solve Eq. (26) using the scheme that we have developed so far, each element g_i must be updated according to the diffusion equation:

$$\frac{dg_i}{dt} = \frac{1}{\kappa^2} \nabla^2 g_i \quad (17)$$

without changing the shape of the core function of the value of g_i . Taking $t = \delta t$, and substituting Eq. (17) into Eq. (12), we obtain $\delta l_i(t) = \delta l_i$. Thus, to simulate the effect of diffusion, the core radius must grow according to:

$$r_i^2 = r_{i0}^2 + 4 \delta t \quad (18)$$

where r_{i0} is the core radius at $t = 0$. The cores of the vortex elements and of different scalar transport elements become different as time progresses. At high diffusivities, or small Peclet numbers, the cores of the elements will experience rapid growth and $\delta \gg \delta h$. In this case, transport elements must be subdivided into elements with smaller cores while preserving their total strength. However, this will not be used here since we are interested in cases where the Peclet number is large. For example, if $r_{i0} = 1 = 0.3$, $t_{max} = 1$, and $\kappa = 0.001$, then $\delta_{max} = 0.4$. These values are typical of what will be used in this study.

If the source term is non-zero, then Eq. (14) is modified to become:

$$\frac{dg_i}{dt} = -g_i \cdot \nabla u + \frac{1}{\kappa^2} \nabla^2 g_i + \sum_{j=1}^K \frac{dW_j}{ds_j} g_{ij} \quad (19)$$

where K is the number of species. Using the definitions of g , the strength of the gradient must be modified according to:

$$\frac{d}{dt} \delta s_i = \sum_{j=1}^K \frac{dW_j}{ds_j} \delta s_{ij} \quad (20)$$

which can be written as a quadrature $\text{dln}(s)/dt = dW/ds$.

The algorithm of the transport element method proceeds as follows: (1) update the locations of the elements x_i according to the velocity at their centers using Eq. (11); (2) update the values of δl_i and n_i either according to the integration of Eq. (10) or by keeping track of the neighboring elements; (3) update the core radii of different elements according to the corresponding Peclet number using Eq. (25); and (4) compute the concentrations of all the scalars using Eq. (24) and (5) update the value of δs_i according to Eq. (20). In most cases, it is possible to use the same set of particles to transport elements of different scalars, as well as the vortex elements, resulting in substantial savings in the transport step.

The transport elements generate an expansion field as their temperature changes, according to Eq. (3). The velocity field associated with this expansion at the low Mach number limit can be obtained written as:

$$\nabla^2 \phi_i = \frac{1}{T_i} \left(\frac{dT_i}{dt} \right) \quad (21)$$

The total velocity produced by the expansion field is:

$$\nabla \phi(x, t) = \sum_{i=1}^N \frac{1}{T_i} \left(\frac{dT_i}{dt} \right) \nabla G_i(x - x_i(t)) \quad (22)$$

where ∇G_i is given by Eq. (25).

IV. THE SPATIALLY-DEVELOPING, NON-REACTING SHEAR LAYER

The vortex element scheme and the transport element scheme were applied to simulate the initial stages of development of a spatially-developing two-stream shear layer. On the left boundary of the domain, it is assumed that the wake region behind the splitter plate, where the two incoming boundary layers merge to form the shear layer, is very small. Thus, at $x = 0$, for $y > \Delta_g$, $U \rightarrow 1$, $T \rightarrow 1$, and for $y < -\Delta_g$, $U \rightarrow 0.355$, and $T \rightarrow 0$, where \rightarrow means "approaches asymptotically". Here, the normalized temperature is defined as $T^* = (T - T_0) / (T_1 - T_0)$, $\Delta_g = 2\sigma^2$, while σ is the standard deviation of the Gaussian distribution that describes the vorticity and the scalar gradients, and $2\Delta_g$ is the nominal shear layer thickness. For the results in Figure 2, $\Delta_g = 1/26.4$, leading to a most unstable wavelength, as predicted by the linear theory, of 1.2. Within the shear layer, the velocity and temperature distributions are error functions.

The rate at which vorticity is convected into the upstream side of computational domain, at $x = 0$, is $\Delta U U_m$. At each time step, five elements arranged vertically are used to

discretize this vorticity using Eq. (10). The potential velocity component, u_p , is computed by adding two source flows at $x = -\infty$ and $y = +\infty$ and $y = -\infty$ to the velocity field in Eq. (2) to satisfy the boundary condition at $x = 0$. The no-flow boundary condition across the solid walls is implemented by using conformal mapping and image vortices⁷. At the downstream side of the computational window, at $x = 6$, vortex elements are deleted. This induces a strong perturbation which ensures that the rollup and first pairing will always take place within the computational window. Since this perturbation is not applied in an organized manner, the resulting shear layer will be considered as an unforced layer.

Figure 2 shows the location and velocity of all vortex elements used in the computations for five time steps. The time step of the computations is $\Delta t = 0.15$. The plots exhibit a very clear and accurate portrait of the rollup. During rollup, the vorticity within the shear layer is attracted towards the center of a large eddy, entraining fluid from both sides, and forming what appears to be a moving focal point of a spiral. Between neighboring large eddies, a zone of strong strain is developing where the vorticity is depleted and the gradients are growing. This "braids" zone can be described as a moving saddle point where locally the fluid flow experiences a separation into two streams; one moving towards the left and the other moving towards the right with respect to the saddle stagnation point. Downstream, the process of rollup continues until a stronger perturbation forces two neighboring eddies to interact in a pairing process. It is important to stress that the algorithm of inserting elements as the strain field develops is responsible for maintaining the organization of the calculation for a long time.

STEP= 42 TIME= 6.38 ELEMENTS= 3634 3987



STEP= 44 TIME= 6.68 ELEMENTS= 4348 4672



STEP= 46 TIME= 6.98 ELEMENTS= 5061 5386



STEP= 48 TIME= 7.28 ELEMENTS= 6073 6356



STEP= 50 TIME= 7.58 ELEMENTS= 7177 7387



Figure 2. The development of large scale vortex structures in a spatial shear layer. Each point in the figure represents a vortex element, and the line is the velocity vector.

Quantitatively, the natural frequency of shedding, is defined as $f_n = U_m / \lambda$, where $U_m = (U_1 + U_2) / 2$, and λ is the wavelength of the large eddy. The corresponding Strouhal number is $St = 1 / f_n = 0.033$. This is the same value as the frequency of the most unstable mode computed from the linear stability theory of a spatially developing shear layer under the conditions described above. Preliminary results for the growth rate, average velocity and turbulent statistics were presented in study of Ghoniem and Ng⁷ for the forced shear layer.

The high resolution of the transport element method demands the use of a large number of transport elements. Moreover, the number of elements grows rapidly with time due to the severe stretch produced in the shear layer. This makes the computation of a wide window which contains a number of successive eddies expensive. In the next section, we direct attention towards a model of this problem that requires less effort computationally while essentially preserving all the physical processes involved in the spatially developing layer. This is the temporal shear layer model in which a computational window that moves at the average speed of the flow is imposed on a single wavelength while the eddy is growing.

V. TEMPORALLY-DEVELOPING, REACTING SHEAR LAYER

Computational results showing the evolution of a large eddy in a temporal shear layer are presented in Figure 3. In this case, the boundary conditions are periodic, i.e., $w(x,y,t) = w(x+\lambda,y,t)$ and $u(x,y,t) = u(x+\lambda,y,t)$, where λ is the wavelength of the perturbation. Since detailed analysis of the evolution of the temporal, thermally stratified shear layer was presented in Ghoniem et al.²⁷, it will not be repeated here. The qualitative resemblance between the development of large eddies in a spatial and a temporal shear layer is clearly seen by comparing Figures 2 and 3. Moreover, the shedding frequency, i.e. the frequency of the most amplified mode, is almost the same in both case. However, the growth rate of the perturbation is different since it depends on the velocity ratio across the layer; a parameter that does not appear in the analysis of the temporal layer.

In the computation of the temporal layer, the window is limited to one wavelength and one can afford to use more elements within the domain to improve the resolution. One can also conduct, inexpensively, parametric studies on the effect of various physical parameters that appear in the model, Eqs.(1-9). Thus, the temporal layer will be used as a model for the spatial layer to study turbulence-combustion interactions in shear flow.

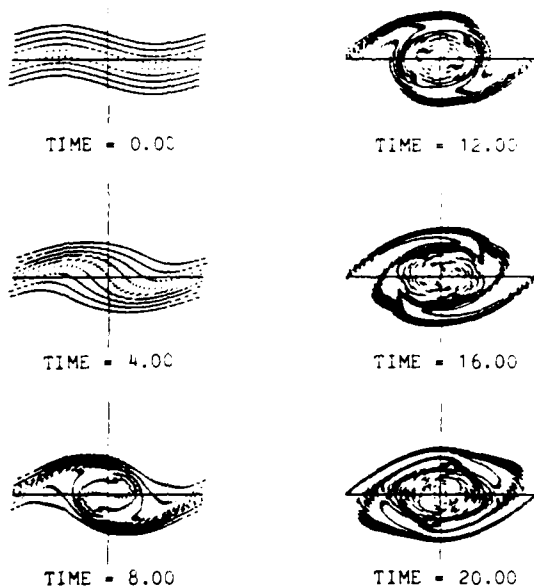


Figure 3. The development of a large eddy in a temporally growing shear layer at the same conditions as in Figure 2.

Since the flow is unconfined, the wavelength λ is used instead of H to non-dimensionalize the length.

The temperature profile across the midsection of the eddy is exhibited in Figure 4. The rollup brings fluid from one side to the opposite side, while stretch increases the gradient across each

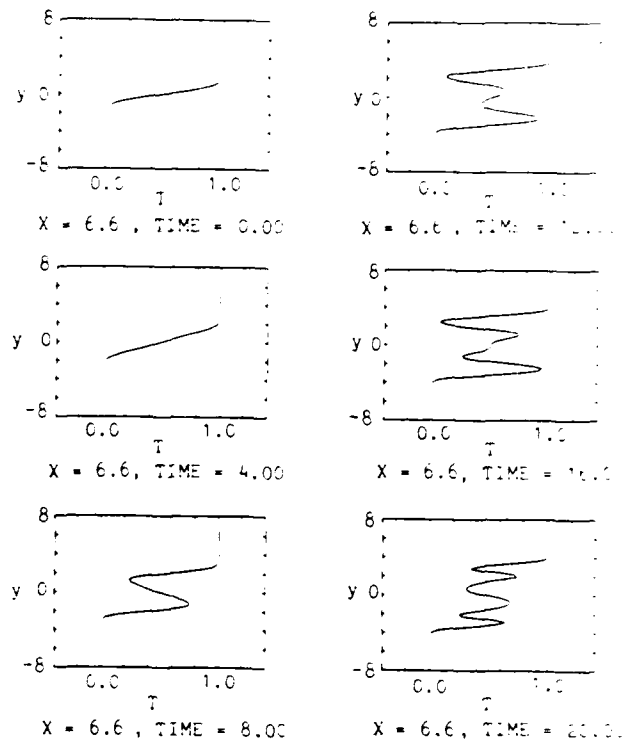


Figure 4. Temperature distribution across the midsection of the large eddy shown in Figure 3

layer. The profiles show that after the relaxation of the first rollup, a secondary instability develops which forces the core through another turn, thus creating a more ragged temperature distribution. Moreover, it can be seen that the rollup of the shear layer is the mechanism of entrainment that leads to strong mixing enhancement as the two fluids diffuse across the stretched interface. Since rollup is associated with strong stretch that reduces the thickness of the material layers, it increases the gradients across these intertwining layers, thus enhancing the diffusion fluxes. Quantitatively,

the rate of mixing can be expressed as $\dot{M} = \int q \cdot n da$, where q is the diffusion flux, n is the unit vector normal to the material surface, and da is the surface area element. Since for two dimensional flow, $da = dl$, and since $q / \delta l =$

constant, then \dot{M} is proportional to $(\delta l)^2$. The net result is that stretch by a factor ζ enhances mixing by a factor ζ^2 . The quadratic rise in mixing during rollup will have a significant effect on the rate of reaction.

In the reacting layer calculations, the full system of equations is integrated using particles that transport vortex elements, temperature gradient elements, reactant and product gradient elements. At time $t = 0$, the vorticity layer and the flame front coincide, and the thicknesses of the vorticity layer as well as the temperature and species concentration within the layer are taken to be equal. A small sinusoidal perturbation with amplitude $c = 0.05 \lambda$ is imposed on both distributions. The first case to be computed corresponds to the following set of parameters: $Pe = 200$, $Le = 1$, $A_F = 1$, $Q = 4$ and $T_a = 10$, and $n = 1$.

The corresponding Damköhler number, measured at the conditions of maximum reaction rate, is around .02, and the temperature ratio across the layer is $T_p/T_R = 5$.

Figure 5 shows the reacting shear layer as rollup proceeds along with the chemical reaction. At the early stages, the eddy strongly resembles that of the nonreacting flow shown in Figure 3. However, as rollup starts, the following is

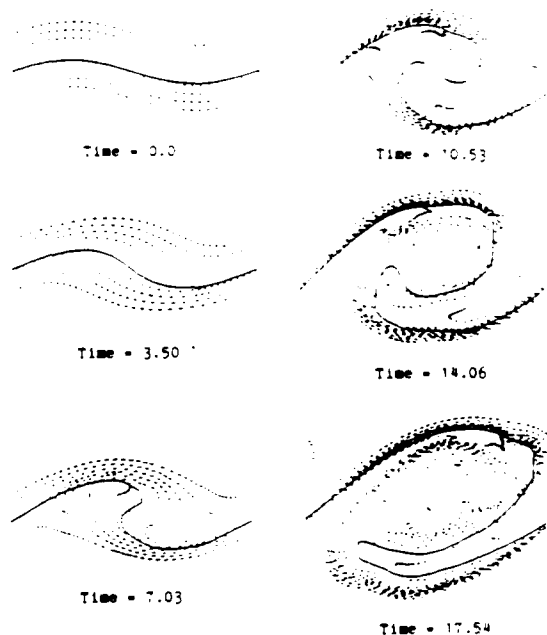


Figure 5. The development of a large eddy in a reacting temporal shear layer at the same conditions as in Figure 3. The solid line defines the flame front.

observed: (1) a swelling, due to the concomitant increase in the rate of heat release, continues as more reactants are entrained into the burning core; (2) the growth of the instability, as measured by the angle between the major axis of the elliptical structure and the main stream direction, is encumbered because the volumetric expansion causes the vorticity intensity to decrease and the eddy to become weaker and less coherent; and (3) the eddy loses its symmetry and becomes eccentric due to the asymmetric expansion and the generation of a non-baroclinic torque associated with heat release. As more of the initial core is burnt, the fluid inside the eddy ceases to spin, contrary to the nonreacting case. Meanwhile reactants move through the side to enter the reaction region. These results agree qualitatively with the experimental results of Keller and Daily⁵ on the reacting mixing layer at high equivalence ratios.

On the same figure, a solid line is plotted through points of maximum reaction rate. The line indicates where the flame front, or the maximum heat release rate, is within the shear layer. Below this line, the product concentration approaches unity and the temperature reaches T_p .

During the early stages of rollup, the line of maximum reaction rate follows one of the material lines closely, i.e., the growth of perturbation

merely changes the topology of the flame front. At later stages, this line, while staying close to another material line, forms a boundary of the products where the reactants are entrained to burn. Below this line, where products form, the core almost stops its rotation. At the last stage of burning of the eddy, the two sides of the flame burn to close this entry way and the flame moves out of the eddy and becomes an ordinary laminar flame.

The effect of heat release on the structure of the eddy, which is generated by the rollup of the shear layer, can be seen from the temperature profiles across the midsection of the wavelength, Figure 6. Since the Lewis number is one, $Le = 1$ ($T = T_R/\lambda$). As reactants are entrained into the

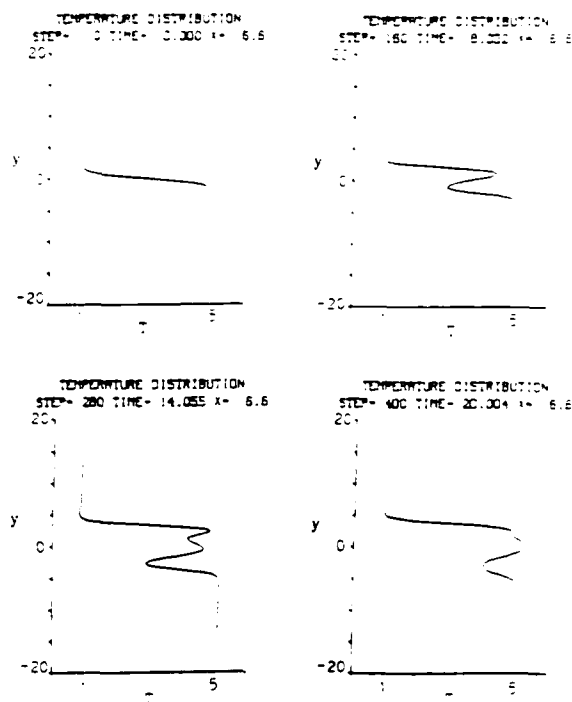


Figure 6. Temperature distribution across the midsection of the reacting large eddy shown in Figure 5.

core of the growing eddy from the right side, a Z-shaped flame is formed. At the initial stages where the rate of entrainment is faster than the rate of burning, the flame extends deeper into the lower stream. As the reactants within this zone burn, heat is released within the core of the rotating eddy, causing the eddy to swell, while maintaining its elliptical shape. The non-baroclinic vorticity generated around this zone causes the observed eccentricity of the large eddy. The temperature profiles show that the higher order instabilities observed in the nonreacting case are suppressed by the heat release, and that the core of the eddy stops its rotation. As the reactants within the eddy burn, the flame leaves the structure and moves into the reactants. This results in the formation of a temperature profile which is very similar to the temperature profile at $t=0$.

To study the effect of the shear layer on the chemical reaction, we compare the rate of burning

for a flame moving through a shear layer, i.e., a reacting shear layer, with the same flame moving into a quiescent environment, i.e., a laminar flame. Results for the laminar flame are obtained using the same method but with $u_x, u_y = 0$. The rate of burning is defined in terms of the total mass of products generated since $t = 0$. Figure 7 depicts the total mass burnt, M_p , for both cases.

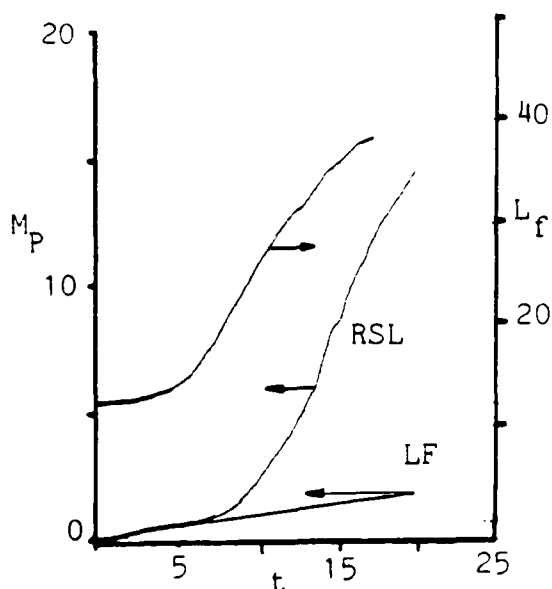


Figure 7. Total mass of products M_p formed since $t = 0$, in the reacting shear layer, labelled as RSL, and in the laminar flame, labelled as LF, at the same conditions, and the total length of the flame in the reacting shear layer of Figure 5.

showing clearly the different stages of burning in the reacting shear layer. At the early stages, during the linear phase of development where the stretch is negligibly small, the rate of burning is linear and identical to that of a laminar flame. As the layer starts to roll up, the area of the reaction surface increases and the flame is convoluted around the growing eddy. The increase in the flame area due to convection is nearly linear, as shown in Figure 7. However, as indicated by the Figure 7, the products form at almost a quadratic rate during this stage. This phenomenon can only be explained by recalling that mixing is enhanced as the square of the stretch, and that in this case of fast chemistry, the rate of burning is governed by mixing.

At later stages, around $t = 20$, the amount of products forming is almost nine times that which forms in the laminar flame. Due to flame convection, the reacting surface area has increased by three folds. Since stretching a layer of material by three times its initial length decreases its thickness by the same amount, and the fluxes across it increase by three fold as well. This augments the rate of mixing by nine times over the non stretching case. When the chemical reaction is fast, as in this

case, the material mixed reacts and the rate of reaction increases by the same rate as the mixing. This is what has been labelled "mixing-controlled reaction" in the turbulent combustion literature.

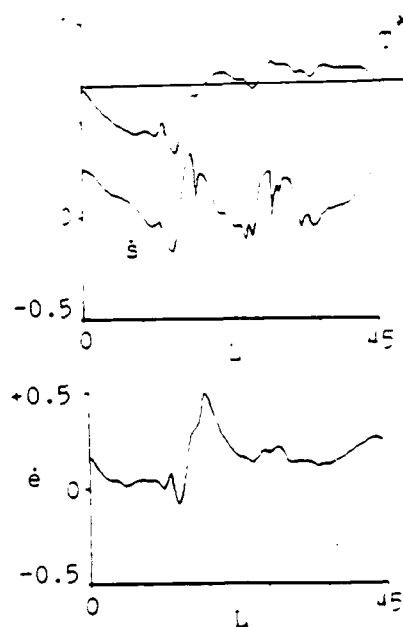


Figure 8. The temperature T , strain rate \dot{s} , and expansion rate \dot{e} along layer 7 in the reacting eddy.

To further analyze the results, we plot the temperature T , the strain rate \dot{s} , and rate of expansion \dot{e} , along one particular layer of fluid within the reacting eddy. The rate of expansion is an indication of the rate of product formation, i.e., the actual reaction rate. Figures 8 and 9

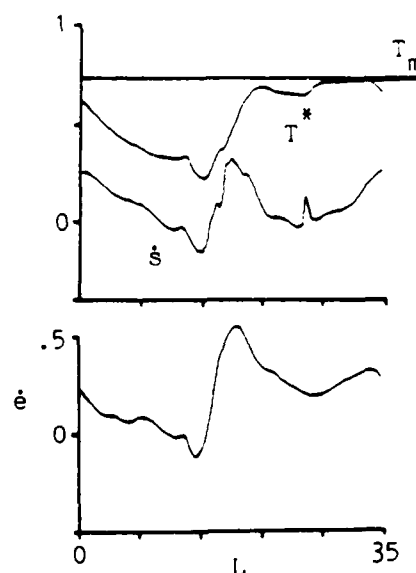


Figure 9. The temperature T , strain rate \dot{s} , and expansion rate \dot{e} along layer 8 in the reacting eddy.

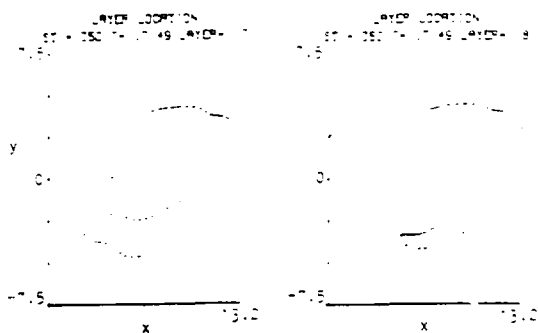


Figure 10. Layers 7 and 6 in the reacting eddy of Figure 5.

show these plots for layers 7 and 6, respectively, which are shown in Figure 10. Figures 8 and 9 show a positive correlation between the temperature and the strain rate; each temperature peak corresponds to a maximum in the strain rate

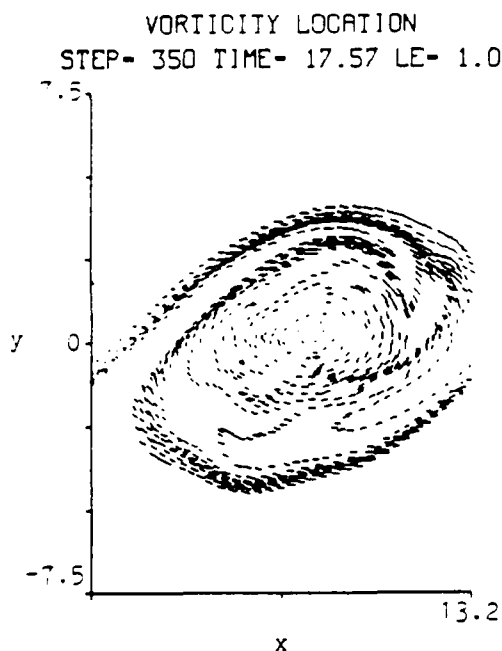


Figure 11. The eddy in a reacting temporal shear layer at the same conditions as in Figure 5 but with $A_f = 0.5$, $t = 17.57$.

curve and vice versa. Moreover, Figures 8 and 9 exhibit a strong correlation between the local strain rate and reaction rate; as the strain rate decreases, the reaction rate decreases and the temperature drops. These results indicate that the rate of burning and temperature are positively correlated with the strain rate. As the layer stretches, the diffusion flux of the reactants into the flame increases and, since chemistry is fast, the rate of burning increases. Under compression, the reactants diffusion flux is reduced and the amount of burnt mixture, and hence the rate of expansion, is reduced.

Decreasing the frequency factor to $A_f = 0.1$, which reduces the Damkohler number by the same factor, yields another remarkable phenomenon: the development of the large eddy in this case is shown in Figure 12. The swelling of the eddy is reduced since the rate of chemical reaction is less than in the case of $A_f = 1.0$. At the early stages, the reaction proceeds in the same manner as before. However, at $t = 10.57$, the reaction suddenly stops, as shown in Figure 12 for the mass of products M_p . The laminar flame with the same

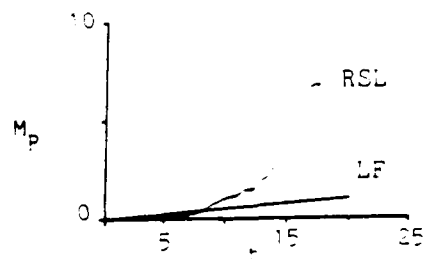


Figure 12. The total mass of products M_p formed since $t = 0$ for a reacting shear layer with $A_f = 0.5$, RSL, and a laminar flame at the same conditions, LF.

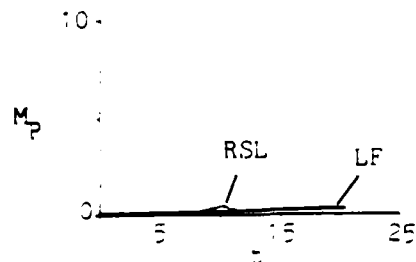


Figure 13. The total mass of products M_p formed since $t = 0$ for a reacting shear layer with $A_f = 0.25$, RSL, and a laminar flame at the same condition, LF.

parameters shows a continuous linear rise in the mass of products. If the frequency factor is lowered further to $A_f = 0.25$, extinction occurs earlier at around $t = 10$, as shown in Figure 13. Meanwhile, the corresponding laminar flame shows a linear rise in M_p . Since the strain rate increases with time, the extinction phenomenon is encountered earlier as the Damkohler number is reduced.

To explain what happens around extinction in more detail, we refer to plots of T , \dot{s} , and \dot{e} , shown for layer 3 in Figure 14 and for layer 5 in Figure 15, both for $A_f = 0.5$. The plots exhibit the variation of the three parameters at $t = 17.57$. The geometry of the two layers is shown in Figure 16. Plots for \dot{e} show that the expansion has almost stopped.

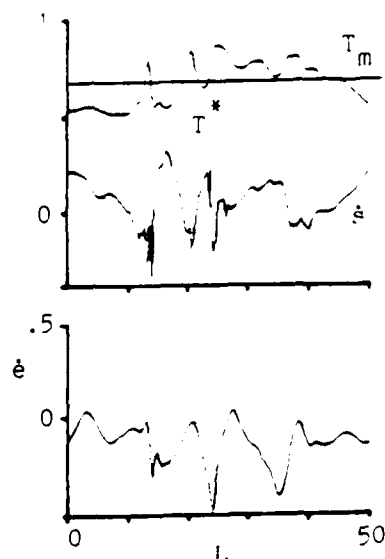


Figure 14. The temperature T , strain rate \dot{s} , and expansion rate \dot{e} along layer 3 in the reacting eddy in Figure 11.

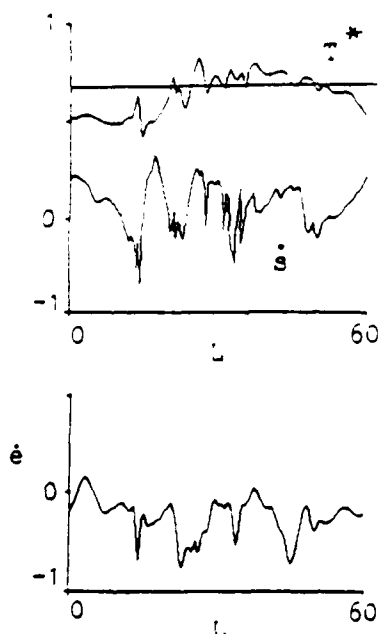


Figure 15. The temperature T , strain rate \dot{s} , and expansion rate \dot{e} along layer 5 in the reacting eddy in Figure 11.

This is in spite of the fact that T corresponds to maximum reaction rate along most of the layer. Contrary to the case of $A_f = 1.0$, the values of T and \dot{s} are now negatively correlated, i.e.

temperature maxima correspond to minima in \dot{s} as shown in Figures 14 and 15. It is also observed that \dot{s} and \dot{e} are negatively correlated, leading to a situation in which strain acts to extinguish the flame. This indicates that the temperature drops

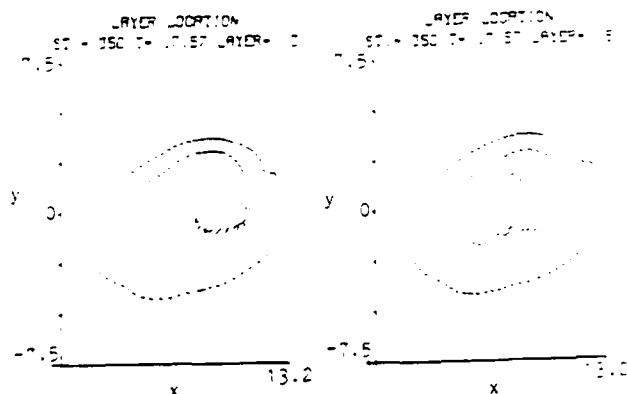


Figure 16. Layers 3 and 5 in the reacting eddy in Figure 11.

with strain due to the increase of the heat flux out of the layer and the reactants flux into the layer. Since chemical reaction is slow, the heat loss and the gain in reactants cannot be compensated by chemical heat release, leading to flame blowout.

VI. CONCLUSIONS

Advanced numerical methods enable one to: (1) integrate elaborate and detailed models, which cannot be done analytically, so that complex mechanisms may be revealed and analyzed; and (2) provide detailed information about the flow field which may not be possible using traditional experimental techniques. Computer output, rich in data, offers a challenge in how to extract valuable information about the phenomena under investigation, and how to present these information in compact form. Finding out the appropriate diagnostics to probe computational results is half the way to reaching the conclusions.

In this article, we have introduced the transport element method: a Lagrangian particle scheme based on the discretization of the vorticity and the gradients of the scalars into finite elements. The particles move along material lines, in accordance with their transport equations. As strong strains develop in the dynamic field, the finite elements may change their shape or configuration to accommodate the distortion which is produced by these strain fields. In case of chemical reaction: (1) the strength of the elements, i.e. the source strength, changes according to the rate of reaction; and (2) the chemical heat release induces volumetric expansion and non-baroclinic vorticity into the dynamic field.

The simplest model which can be proposed to study turbulence-combustion interactions contains five parameters: (1) the Peclet number which defines the ratio between the rate of convective and diffusive heating; (2) the Lewis number which represent the ratio between the rate of heat and mass diffusion; (3) the frequency factor which defines the ratio between the rate of chemical reaction and mass convection; (4) the activation energy of the reaction; and (5) the enthalpy of reaction. The outcome of these interactions can, thus, be presented on a five dimensions space on

which one can identify several subdomains for burning enhancement, flame extinction, flame oscillations, etc. To accomplish this goal, computations must be performed for a matrix of parameters. The compiled data can then be plotted on this space. Under the idealization of high activation energy and thin flame structure, results of the asymptotic analysis can be used to fill some parts of this space and show the limiting trends^{32,33,34}.

In this article, we presented results for the effect of changing the frequency factor, which leads to changing the Damköhler number, at fixed values of the rest of the parameters. We showed that for $P_e = 200$, $L_e = 1$, $T_a = 10$ and $Q = 4$, at $A_f = 1.0$, the stretch associated with the rollop of large eddies in the mixing layer enhances the combustion process by a factor proportional to the square of the stretch. This is contrary to the assumption made in the conventional wrinkled laminar flame theory that the increase in the rate of burning is linearly proportional to the stretch factor. This quadratic increase in the total rate

of burning was found to result from the increase in the mass diffusion flux across the burning layer.

At values lower than $A_f = 1$, combustion is interrupted under strong stretch. At smaller values of A_f , the flame is extinguished earlier. This is due to the fact that the rise in the mass flux into the reaction zone is not balanced by an increasing in heat release by chemical reaction within this zone. The reaction zone is thus cooled, followed by the extinction of the flame. Work is underway to vary the rest of the controlling parameters and study their effect on the flame stability.

ACKNOWLEDGEMENT

This work was supported by the Air Force Office of Scientific Research Grant AFOSR-84-0301, the U.S. Department of Energy, Office of Energy Utilization, Energy Conservation and Utilization Technologies Program Contract DE-AC04-85-OR21401, the National Science Foundation Grant DMR-84-14441, and the Edgerton Professorship at M.I.T.

REFERENCES

1. Libby, P.A. and Williams, F.A., eds., Turbulent Reacting Flows, Springer-Verlag, Berlin, 1980, XIII + 243 p.
2. Chigier, N.A., ed., Progress in Energy and Combustion Science, special issue on Turbulent Reacting Flows, 12, (1986).
3. Brown, G.L. and Rosko, A., J. Fluid Mech., **64**, 775 (1974).
4. Ho, C.-H., and Huerne, P., Ann. Rev. Fluid Mech., **16**, 365, (1985).
5. Keller, J.O. and Dally, J.W., AIAA J., **23**, 1937, (1985).
6. Mungal, M.G., and Dimotakis, P.E., J. Fluid Mech., **146**, 349, (1984).
7. Ghoniem, A.F. and Ng, K.K., Phys. Fluids, **30**, 706, (1987).
8. Broadwell, J.E. and Breidenthal, R.E., J. Fluid Mech., **125**, 397, (1982).
9. Driscoll, J.F., Tangirala, V. and Chen, R.H., Combust. Sci. Tech., **51**, 75, (1986).
10. Kelly, J. private communications.
11. Hald, O., SIAM J. Num. Anal., **16**, 726, (1979).
12. Beale, J.T. & Majda, A., Math. Comp., **39**, 26, (1982).
13. Anderson, C., J. Comput. Phys., **61**, 417, (1985).
14. Corcos, G.M. and Snerman, F.S., J. Fluid Mech., **139**, 29, (1984).
15. Grinstein, F.F., Oran, E.S. and Boris, J.P., J. Fluid Mech., **165**, 201, (1986).
16. Riley, J.J., and Metcalfe, R.W., AIAA paper 80-0274.
17. Ashurst, W.T., in Turbulent Shear Flows, ed. Durst et al. (Springer-Verlag, Berlin, 1984), p. 412.
18. McMontry, P.A., Jou, W.A., Riley, J.J., and Metcalfe, R.W., AIAA Journal, **24**, 960 (1986).
19. Ghoniem, A.F. and Givi, P., AIAA paper 87-0226.
20. Chorin, A.J., J. Fluid Mech., **57**, 757 (1973).
21. Chorin, A.J., "Vortex models and boundary layer instability," SIAM J. Sci. Stat. Comput., **1**, 1980, pp. 1-24.
22. Leonard, A., J. Comput. Phys., **37**, 289 (1980).
23. Ghoniem, A.F. and Gagnon, Y., J. Comput. Phys., **65**, 342, (1987).
24. Sethian, J.A. and Ghoniem, A.F., "Validation of the vortex method," J. Comput. Phys., to appear.
25. Ashurst, W.T. and Barr, P.K., "Lagrangian-Eulerian calculation of turbulent diffusion flame propagation," Sandia Report SAND80-9950, Sandia National Laboratories, 1980.
26. Ghoniem, A.F., Chorin, A.J. and Oppenheim, A.K., Phil. Trans. Roy. Soc. Lond., **A304**, 303, (1982).
27. Ghoniem, A.F., Heidarinejad, G. and Krishnan, A. "Vortex element simulation of the rollop and mixing in a thermally stratified shear layer," J. Comput. Phys., submitted for publication.
28. Leonard, A. Ann. Rev. Fluid Mech., **17**, 543, (1985).

29. Ghoniem, A.F., Knio, G.M., and Ali, H.F.,
AIAA Paper 87-0379.
30. Majda, A., and Sethian, J.A., Comput. Math.
Tech., 42, 185, (1987).
31. Ghoniem, A.F., Lectures in Applied
Mathematics, 34, ed. by A. Ludford, 1987,
(Amer. Math. Soc., 1988), p. 197.
32. Clavin, F., Prog. Energy Combust. Sci., 11, 1
(1985).
33. Williams, F.A., Combustion Theory, 2nd ed.,
Benjamin/Cummings, 1985, xxiii + 650 p.
34. Buckmaster, J.D. and Ludford, G.S.G.,
Lectures on Mathematical Combustion, SIAM,
1983, V + 126 p.

Appendix III

The paper on "Vortex-scalar element calculations of diffusion flame stabilized on a plane mixing layer" describes the scalar element method and its application to a diffusion flame with low heat release.

AIAA'87

AIAA-87-0225

**Vortex-Scalar Element Calculations of a
Diffusion Flame**

A. F. Ghoniem, Massachusetts Institute of
Technology, Cambridge, MA; and

P. Givi, Flow Research Company, Kent, WA

AIAA 25th Aerospace Sciences Meeting

January 12-15, 1987/Reno, Nevada

For permission to copy or republish, contact the American Institute of Aeronautics and Astronautics
1633 Broadway, New York, NY 10019

VORTEX-SCALAR ELEMENT CALCULATIONS OF A DIFFUSION FLAME
STABILIZED ON A PLANE MIXING LAYER

Ahmed F. Ghoniem* and Peyman Givi**
Department of Mechanical Engineering
Massachusetts Institute of Technology
Cambridge, MA 02139

ABSTRACT

The vortex-scalar element method, a scheme which utilizes vortex elements to discretize the region of high vorticity and scalar elements to represent species or temperature fields, is utilized in the numerical simulations of a two-dimensional reacting mixing layer. Computations are performed for a diffusion flame at high Reynolds and Péclet numbers without resorting to turbulence models. In the non-reacting flow, the mean and fluctuation profiles of a conserved scalar show good agreement with experimental measurements. Results for the reacting flow indicate that for temperature-independent kinetics, the chemical reaction begins immediately downstream of the splitter plate where mixing starts. Results for the reacting flow with Arrhenius kinetics show an ignition delay, which depends on the reactants temperature, before significant chemical reaction to occurs. Harmonic forcing changes the structure of the layer, and concomitantly the rates of mixing and reaction, in accordance with experimental results. Strong stretch within the braids in the non-equilibrium kinetics case causes local flame quenching due to the temperature drop associated with the large convective fluxes.

I INTRODUCTION

Turbulent diffusion flames have been the subject of extensive experimental and theoretical investigations during recent years (for a review, see Bilger [1]). In most of the theoretical work, turbulence models are used to close a system of averaged transport equations which describes the statistical behavior of the aerothermodynamical variables. Moment methods [2], eddy break-up and mixing controlled models [3], flame sheet approximation [4], assumed probability density function (PDF) shape methods [5], solutions based on modelled joint PDF of scalar quantities [6,7], and based on modelled joint PDF of scalar and velocity [8] are examples in which turbulence modelling have been used for the closure of equations governing the statistical quantities. Much effort has gone into constructing accurate

models and in obtaining results that are in agreements with experimental measurements. However, in complex systems, modelling is difficult because of our lack of knowledge on the detailed dynamics of the flow. Furthermore, since most of the interesting dynamical behavior of the flow is modelled a priori, such features are not exhibited from the results of numerical computations based on turbulence models, and thus can not advance our understanding of turbulent combustion.

The progress in numerical methods and the availability of supercomputers have had a major impact on turbulence research. Improved accuracy of the numerics and increased storage and computational speed have made it possible to solve the appropriate transport equations governing turbulent combustion directly without the need for modelling for some limited parameter range. Such model-free "simulations," in comparison with calculations utilizing turbulence models, have the advantage that the physics of the problem is not modelled a priori, but is recovered directly from the computed results. Their results can be used to understand many important mechanisms of turbulent transport and its direct influence on chemical reactions. Furthermore, since the instantaneous behavior of the variables are known at all points and at all times, accurate simulations offer a good method of probing the flow when experimental techniques may fail. Ultimately, by validating the results of the simulation against experimental measurements, ab initio predictions will be a reality.

Numerical methods have been used in a variety of forms for the simulation of turbulent flows in complex configurations. A recent survey can be found in review articles [9,10]. In reacting flow, three approaches are used: (1) finite difference methods, (2) spectral methods; and, (3) vortex methods. In the first approach, the variables are defined on a grid and the transport equations are approximated by discretizing the derivatives on the grid nodes. Examples of this approach can be found in the work of Corcos and Sherman [11] who used a projection method to study the temporal evolution of a periodic shear layer, and in Grinstein et al. [12] who used a flux-corrected transport scheme to simulate the development of coherent structures in a two-dimensional spatially evolving shear layer and examined their effect on mixing.

In spectral methods, the variables are expanded in series of harmonic functions that satisfy the differential equations on a number of collocation points. Riley et al. [13] used a pseudo-spectral scheme to study a three dimensional temporally-evolving reacting mixing layer assuming a constant reaction rate, constant

Copyright © 1987 by A.F. Ghoniem. Published by the American Institute of Aeronautics and Astronautics, Inc. with permission.

* Associate Professor, Associate fellow AIAA.

** Research Scientist, Flow Research Company, Kent, Washington, Member AIAA.

density and no heat release. McMurry et al. [14] considered the effects of the chemical heat release on the fluid dynamics of a two-dimensional mixing layer for a constant reaction rate. The interplay between fluid dynamics and the chemical reaction is investigated under these conditions. Givi et al. [15] used the same method to compute a two-dimensional mixing layer with an Arrhenius chemical reaction and constant density to assess the effects of large coherent structure on the local extinction of the flame. Extension to spatially-growing layers was initiated by Givi and Jou [16] using a hybrid pseudo-spectral second order finite difference scheme. In all cases, the Reynolds number was kept at small values, $O(100)$, limited by the grid resolution and the number of harmonic modes.

In the third approach, vortex methods are used. These schemes are grid free, the transport of the variables take place in a Lagrangian form, and the solution is not restricted by the geometry of the confinement. Therefore they can provide accurate simulations for high Reynolds number, spatially growing flows. Moreover, vortex methods optimize the computational efforts by distributing computational elements around regions of high vorticity. The application of the method in thin premixed flame calculations with a finite density jump has been reported by Ghoniem et al. [17] and Sethian [18], among others. In these calculations, the vortex method was employed to compute the flow field, and the dynamic effect of combustion was represented by the propagation of a thin interface at the laminar burning velocity acting as a volumetric source.

Vortex methods were also used in simulating diffusion flames in connection with a finite-difference approach for the treatment of the scalar variables. Ashurst and Barr [19] used the vortex method to compute the hydrodynamic field and an Eulerian flux-corrected transport algorithm to compute the diffusion and convection of a conserved Shvab-Zeldovich scalar approximating the shape and convolution of the flame in the limit of infinitely fast chemical reaction. Lin and Pratt [20] used the random vortex method to simulate the large-scale motion and a Monte-Carlo method to calculate the time-dependent probability density function of the scalar quantities for both gaseous and aqueous mixing layers. The PDF transport equation, however, required a closure model for the molecular mixing term.

From this short review, it is clear that numerical simulations have played an important role in elucidating the physics of turbulent reacting flows, and that there is a continuing need for more model-free simulations in order to explain better some of the interesting physical phenomena that have been observed in laboratory experiments.

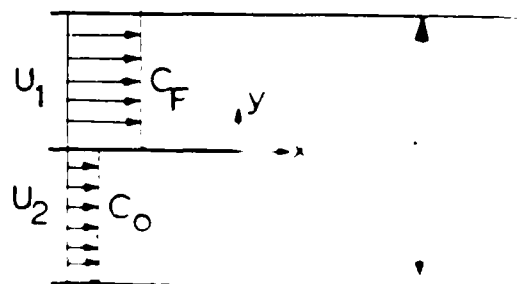
In this work, we extend the vortex method to study non-premixed chemical reactions. A vortex-scalar element method is developed to treat both the hydrodynamic and the scalar field in a Lagrangian sense. The fact that a chemical reaction is truly a Lagrangian process, i.e., it occurs when the particles (or macroscopic elements) interact as they flow, motivate the implementation of Lagrangian methods for simulations of high Reynolds number reacting flows. The method is capable of handling a wide variety of initial and boundary conditions and is not limited to simple flow configurations.

allows simulations of flow with higher Reynolds and Peclet numbers. In this paper, we concentrate on the formulation of the model and the numerical schemes, and present some preliminary validation studies and interpretations of the results.

In Section II, the geometrical configuration of a spatially evolving mixing layer is presented, and the formulation of the problem and of the scheme are described. Results of some sample calculations are given in Section III. Computations of a non-reacting mixing layer is performed first in order to check on the accuracy of the method by comparing its results with experimental measurements at the same conditions. Preliminary results of a simulation of a reacting mixing layer in which the two reactants are introduced in different streams are presented next. Both constant rate kinetics and temperature dependent kinetics are considered. In both cases, the influence of the coherent structures on the finite rate chemistry is assessed and in the second case, the non-equilibrium effects in the reaction rate are examined. In the constant rate kinetics calculations, the influence of harmonic forcing at the inlet of the mixing layer is investigated. This study was motivated by recent experimental observations of Roberts and Roshko [21] and numerical computations of Ghoniem and Ng [22]. The paper is concluded in Section IV with a summary of our new results and suggestions for future developments.

II FORMULATION AND NUMERICAL SCHEME

A two-dimensional, confined, planar mixing layer is considered. A schematic diagram for the flow field is shown in Fig. 1. Two initially unmixed reactants, fuel F and oxidant O , are present at small concentrations in the top high speed stream and bottom low speed stream, respectively. We make the following assumptions: (1) the heat release is low so that its effect on the dynamics of the flow is negligible; (2) the Mach number is small; (3) the free stream concentrations of F and O are equal and constant; (4) the molecular diffusivities are equal and constant; (5) the viscosity is the same in both streams; and (6) the chemical reaction between F and O is single step, irreversible, and second order. The density is, therefore, constant.



AD-A189 813

NUMERICAL SIMULATION OF TURBULENT FLAMES USING VORTEX
METHODS(U) MASSACHUSETTS INST OF TECH CAMBRIDGE
A F GHONIEH 05 OCT 87 AFOSR-TR-87-1853 AFOSR-84-0356

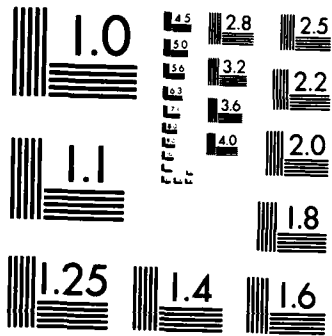
2/2

UNCLASSIFIED

F/G 21/2

ML





MICROCOPY RESOLUTION TEST CHART
NATIONAL BUREAU OF STANDARDS-1963-A

the transport equations of the hydrodynamic field and the scalar -- temperature or species -- fields are decoupled. The equations governing this system are:

$$F + 0 \xrightarrow{k} P \quad (1)$$

$$\nabla^2 \psi = -\omega(x, t) \quad (2)$$

$$\frac{\partial \omega}{\partial t} + \mathbf{u} \cdot \nabla \omega = \frac{1}{Re} \nabla^2 \omega \quad (3)$$

$$\frac{\partial T}{\partial t} + \mathbf{u} \cdot \nabla T = \frac{1}{Pe} \nabla^2 T + Q Da \dot{W} \quad (4)$$

$$\frac{\partial c_j}{\partial t} + \mathbf{u} \cdot \nabla c_j = \frac{1}{Pe Le} \nabla^2 c_j - Da \dot{W} \quad (5)$$

$$\frac{\partial c_p}{\partial t} + \mathbf{u} \cdot \nabla c_p = \frac{1}{Pe Le} \nabla^2 c_p + Da \dot{W} \quad (6)$$

where P indicates products and $\dot{W} = c_F c_O \exp(-Ta/T)$ is the reaction rate, written in terms of the rate of generation of products per unit mass. $\mathbf{u} = (u, v)$ is the velocity, $\mathbf{x} = (x, y)$ and x, y are the streamwise and cross stream directions, respectively, t is time, ψ is the stream function defined such that $u = \partial \psi / \partial y$ and $v = -\partial \psi / \partial x$, $\omega = \nabla^2 \psi$ is the vorticity, c is the concentration per unit mass, T is temperature. $\nabla = (\partial/\partial x, \partial/\partial y)$, and $\nabla^2 = \partial^2/\partial x^2 + \partial^2/\partial y^2$. Variables are non-dimensionalized with respect to the appropriate combination of the total shear $\Delta U = U_1 - U_2$, the channel height H , the free stream concentration of F , c_{FO} , the free stream temperature at $x = 0$, T_0 .

In Eq. (5), $j = F$ or O for fuel and oxidizer, respectively. $Re = \Delta U H / \nu$ is the Reynolds number, where ν is the kinematic viscosity. The reaction rate constant $k = A \exp(-Ta/T)$ where A is the frequency factor, and Ta is the activation energy, non-dimensionalized with respect to (RT_0) , R being the gas constant. Q is the enthalpy of reaction, non-dimensionalized with respect to $C_p T_0$, where C_p is the specific heat at constant pressure. $Pe = \Delta U H / \alpha$ is the Peclet number, where α is the thermal diffusivity. $Da = A c_{FO} H / \Delta U$ is the first Damkohler number. $Le = \alpha / D$ is the Lewis number.

Since Eqs. (4), (5) and (6) are similar, there is no need to solve them all if the scalar concentrations c_F , c_O and c_p are normalized in such a way that their initial and boundary conditions are identical. This is accomplished by the use of Shvab-Zeldovich transformation [1]. Introducing conserved scalars $\beta_{FP} = c_F + c_p$, and $\beta_{OP} = 1 - (c_O - c_p)$, we get:

$$\frac{\partial \beta_j}{\partial t} + \mathbf{u} \cdot \nabla \beta_j = \frac{1}{Pe Le} \nabla^2 \beta_j \quad (7)$$

for $j = FP$ or OP . Since β_{FP} and β_{OP} have the same initial and boundary conditions, $\beta_{FP} = \beta_{OP} = \beta$.

The finite rate kinetics effects can be taken into account by considering the transport equation for the product of chemical reaction, Eq.(6), and Eq. (7) for a conserved scalar. If the Lewis number

is unity, another conserved scalar can be introduced, $\beta_{PT} = c_p - T/Q$, and the solution of Eqs. (6) and (7) for c_p and β will determine the behavior of all the scalar quantities, c_F , c_O , c_p , and T .

II.1 THE VORTEX SCHEME

In the vortex method, the vorticity field is represented by a finite number of vortex elements of finite cores:

$$\omega(x, t) = \sum \Gamma_i / \delta^2 f(\mathbf{x} - \mathbf{x}_i) \quad (8)$$

where $\Gamma_i = \oint \omega dA$, is the circulation of a vortex element and δ is the core radius, while \mathbf{x}_i is the center of the element. f represents the vorticity distribution associated with a vortex element, or the core function (Chorin [23] and Hald [24], and Beale and Majda [25].) The velocity field is obtained by solving Eq. (2) using the discrete vorticity distribution:

$$\mathbf{u} = \sum \Gamma_i K(\mathbf{x} - \mathbf{x}_i) \kappa(\mathbf{x} - \mathbf{x}_i) + \mathbf{u}_p \quad (9)$$

where $K(\mathbf{x}) = -(y, -x)/r^2$ is the kernel of the Poisson equation, $\kappa(\mathbf{x}) = \oint r f(r) dr$ is the circulation within r , and $r = |\mathbf{x}|$. \mathbf{u}_p is an irrotational velocity field added to satisfy the potential boundary condition; $\mathbf{u}_p = \nabla \phi$ where $\nabla^2 \phi = 0$ and $\mathbf{u} \cdot \mathbf{n} = 0$ on solid boundaries while $\mathbf{u} \cdot \mathbf{n} = U$ at the inlet, \mathbf{n} is the normal unit vector. For the confined shear layer, the boundary condition at $x = 0$ is: $\mathbf{u} = U_1$ for $y > 0$ and $\mathbf{u} = U_2$ at $y < 0$, while $y = 0$ is a vortex sheet of strength $\Delta U = U_1 - U_2$.

In this work, we use Rankine vortex elements, i.e., the vorticity of an element is constant within the core and zero outside, $f(r) = 1/\pi$ for $r \leq \delta$ and $f(r) = 0$ for $r > \delta$. Correspondingly, $\kappa(r) = r^2/2\pi$ for $r \leq \delta$ and $\kappa = 1$ for $r > \delta$. Moreover, the potential velocity field is obtained by conformal transformation. Thus, the physical plane is mapped onto the upper half plane and image vortices are used to satisfy the potential boundary conditions. The form of the mapping function for the confined shear layer is given by Ghoniem and Ng [22].

The motion of the vortex elements must be constructed such that the vorticity field satisfies Eq. (3). This is accomplished by solving this equation in two fractional steps:

$$\text{Convection: } \frac{\partial \omega}{\partial t} + \mathbf{u} \cdot \nabla \omega = 0 \quad (10)$$

$$\text{Diffusion: } \frac{\partial \omega}{\partial t} = \frac{1}{Re} \nabla^2 \omega \quad (11)$$

In the first step, the convective transport of vorticity is implemented in terms of the Lagrangian displacement of the vortex elements using the current velocity field computed from Eq. (9). In the second step, the solution of the diffusion equation is simulated stochastically by the random walk displacement of the vortex elements according to the appropriate population. Thus:

$$\mathbf{x}_i(t + \Delta t) = \mathbf{x}_i(t) + \sum_k \mathbf{u}(\mathbf{x}_{ik}) \Delta t + \boldsymbol{\eta}_i \quad (12)$$

for $i = 1, 2, \dots, N$, where Γ_k is a k -th order time-integration scheme and η_i is a two dimensional Gaussian

random variable with zero mean and standard variation $\sqrt{2\Delta t/Re}$. For more details, see Ghoniem and Ng [22], Ghoniem and Gagnon [26].

The no-slip boundary condition at the walls is satisfied by generating new vortex elements to cancel the induced velocity by the vorticity field. Here, we generate vorticity only at the point of separation, i.e. at the tip of the splitter plate since the growth of the boundary layers along the channel walls at these high Reynolds numbers is small. At each time step, the new vorticity $\Delta\Gamma = -\Delta U \Delta t$, where $U_m = (U_1 + U_2)/2$, is consigned to No elements of strength $\Delta\Gamma/No$ and added to the field at points $\Delta x = U_m/No$ apart downstream of $x = 0$.

The effect of the numerical parameters on the accuracy of the results was investigated by Ghoniem and Ng [22]. Their results emphasized the importance of using a high order time-integration scheme with $k=2$ to avoid excessive numerical diffusion in the vorticity field. The value of $No = 6$ was also found to be appropriate in order to obtain well-defined eddy structures after the rollup and the first two pairings. The second pairing is accomplished within the domain of $0 \leq x \leq 6$, therefore the computational domain was limited to $X_{max} = 6$. Downstream of X_{max} , the vorticity was deleted. Varying X_{max} showed that the effect of deleting the vortex elements propagates about one channel height upstream, hence the results are accurate only for $0 \leq x \leq 5$.

II.2 THE SCALAR ELEMENT METHOD

In this scheme, which is a two dimensional extension of the random element method of Ghoniem and Oppenheim [27], the scalar field is represented by a set of elements each carrying a finite amount of the scalar field:

$$s(x, t) = \sum s_i \delta(x - x_i) \quad (13)$$

where s is a scalar field, being the temperature or species concentration, s_i is the strength of an element, defined as the amount of scalar carried by this element and $\delta(\cdot)$ is the Dirac delta function. $s_i = 1/\delta A \int s(x, t) dA$, where $\delta A = \delta x \delta y$, and δx and δy are the distances between the centers of neighboring elements in the streamwise and cross stream directions, respectively, and x_i is the center of the element. If s is an active scalar, its transport is governed by:

$$\frac{\partial s}{\partial t} + u \cdot \nabla s = \frac{1}{Se} \nabla^2 s + \dot{w} \quad (14)$$

where Se is the ratio between the diffusive and convective time scales of transport of s , $Se = Pe$ for $s = T$, and $Se = Pe Le$ if $s = c$. In the scalar element method, this equation is solved in three fractional steps:

$$\text{Convection} \quad \frac{\partial s}{\partial t} + u \cdot \nabla s = 0 \quad (15)$$

$$\text{Diffusion} \quad \frac{\partial s}{\partial t} = \frac{1}{Se} \nabla^2 s \quad (16)$$

$$\text{Reaction} \quad \frac{\partial s}{\partial t} = \dot{w} \quad (17)$$

Convective and diffusive transport are taken into account in a similar way as in the vortex method, i.e. by the Lagrangian motion of the scalar elements using the velocity field u , computed using Eq. (9), and the random walk displacement of the elements using a set of Gaussian random variables with zero mean and standard deviation $\sqrt{2\Delta t/Se}$ (Ghoniem and Sherman [28].) If x_i is the center of the element i , then,

$$x_i(t+\Delta t) = x_i(t) + \sum u(x_{ik}) \Delta t + \eta_i \quad (18)$$

Chemical reaction changes the amount of reactants carried by the element according to the integration of Eq. (17),

$$s_i(t+\Delta t) = s_i(t) + \dot{w} \Delta t \quad (19)$$

However, the reaction occurs only when the elements are close enough for molecular mixing to affect their composition. Therefore, at every time step, the distance between the centers of each two elements of F and O , $\Delta x_{ij} = |x_i - x_j|$, is computed. If $\Delta x_{ij} \leq \delta_D$, where $\delta_D = 0(1/\sqrt{Se})$ is the diffusion length scale, the composition of each of the two elements changes according to Eq. (19). The initial distance between neighboring elements must be small enough to allow enough interactions between the elements. This limits the maximum value of the Peclet number that can be economically used in the computations to $O(1000)$.

The scheme, while providing an approximate solution of Eq. (12) in a stochastic sense, mimics closely the actual physics of the reaction process. This is achieved by using the lagrangian formulation of the transport equations and dealing with the chemical production terms in individual particles.

III RESULTS AND DISCUSSION

The computer code, developed by Ghoniem and Ng [22] for vortex simulation of a non-reacting shear layer, was vectorized in order to take advantage of the computational capability of a CRAY-XMP. The scheme, being explicit in time and requiring mostly non recursive computations, can utilize this capability efficiently. The dynamics of the non reacting layer was investigated in detail in the work of Ghoniem and Ng [22]. Here we concentrate on results pertaining to mixing and to a chemically-reacting layer.

III.1 NON-REACTING MIXING LAYER

Results of a typical simulation, presented in terms of the velocity and location of all vortex elements used in the computations, are shown in Figs. 2, 3 and 4 for the cases of $Re = 24000$, $Re = 4000$, and $Re = 1000$, respectively. Each vortex element is depicted by a point, while its velocity relative to the mean velocity is represented by a line vector starting at the center of the vortex element. The velocity ratio across the layer at the inlet is $U_2/U_1 = 1/3$.

U2 = 0.3333, Re = 24000
TIME = 20.00.



U2 = 0.3333, Re = 24000
TIME = 20.00.



U2 = 0.3333, Re = 24000
TIME = 20.00.



Figure 2. Vorticity field at $Re = 24000$,
 $U2/U1 = 1/3$.

U2 = 0.3333, Re = 10000
TIME = 20.00



U2 = 0.3333, Re = 10000
TIME = 20.00



U2 = 0.3333, Re = 10000
TIME = 20.00



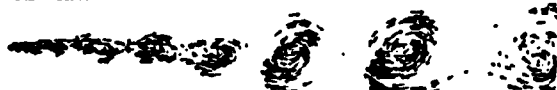
Figure 3. Vorticity field at $Re = 10000$,
 $U2/U1 = 1/3$.

Results show the formation of large vortex eddies by the rollup of the vorticity layer that emanates at the splitter plate, and the subsequent pairings of these eddies into larger structures. The rollup of the shear layer was investigated in Ghoniem and Ng [22] by analyzing results at a wide range of the Reynolds number and at different boundary conditions. Their analysis show that: (1) the rollup is due to the growth of perturbations by the Kelvin-Helmholtz instability mechanism, and the shedding frequency corresponds to the most unstable frequency predicted from the linear stability analysis of a spatially growing layer; (2) pairing, which is associated with the local subharmonic perturbations, results in a step-wise increase in the size of the vorticity layer as two eddies merge; (3) The two sources of the subharmonic perturbations are the downward motion of the layer and the monotonic growth in the size of the eddies downstream; (4) the intrinsic dynamics of the instability is not strongly affected by the value of the Reynolds

U2 = 0.3333, Re = 4000
TIME = 20.00.



U2 = 0.3333, Re = 4000
TIME = 20.00.



U2 = 0.3333, Re = 4000
TIME = 20.00.



Figure 4. Vorticity field at $Re = 4000$,
 $U2/U1 = 1/3$.

number, except that at the low Reynolds number the eddies are slightly larger due to the dispersion of vorticity by diffusion; and (5) the computed velocity statistics show good agreements with experimental data, indicating that the fundamental mechanisms of the shear layer are two dimensional and, hence, the numerical scheme is capable of predicting the large scale features accurately.

To study entrainment, a passive conserved scalar with a normalized concentration value equal to zero in the high speed stream and equal to one in the low speed side is introduced at the inlet section. At each time step, 19 elements are introduced in each stream. The initial distance between two neighboring elements in the cross stream direction is taken as $\delta y = 0.021$. The time step $\Delta t = 0.1$, thus the distance between the elements in the streamwise direction is $\delta x = 0.05$ on the average. Since diffusion is more critical in the cross stream direction, δy is chosen to be smaller than δx . A case with $\delta y = 0.016$, using 25 elements in each stream was computed, showing no significant change in the overall behavior.

Figures 5, 6 and 7 are obtained for Reynolds number, Peclet number and velocity ratio 10,000, 4,000 and 1/2, respectively. Figures 5 and 6 show the velocity and location of all the vortex and scalar elements respectively, while Fig. 7 exhibits the strength of each of the scalar elements at the non-dimensional times of $t = 28, 29$ and 30 . In Fig. 6, the dots represent the fluid from the high speed side with normalized concentration $c = 0$, and the open circles represent the fluid from the low speed side with $c = 1$. This figure indicates that the rollup of the vortices and their subsequent pairing entrains fluid from both sides of the free streams into the cores of the vorticity layer, which results in the enhancement of mixing between the two streams. Entrainment asymmetry is observed as more fluid from the high speed side is present in the low speed side than the opposite (Koochesfahani [29]).

The instantaneous profiles of the concentration field are averaged over a long-time period and the statistical values are compared with experimental data in Figs. 8 and 9. Figure 8 shows the mean value of the concentration, c_m , as

a function of $(y-y_0)/(x-x_0)$, where y_0 is measured at $\bar{c}_m = 0.5$ and x_0 is the virtual origin of the mixing layer based on the mean concentration profile (in the calculation, $x_0 = 0$). In this figure, the solid line is the computed mean concentration at $x = 4$ and the data points are obtained from recent experimental measurements by Masutani and Bowman [30] for a dilute non-reacting mixing layer with the same velocity ratio. Figure 9 shows a comparison between the computed and measured mean fluctuations of the concentration, $\bar{c}'^2 = (\bar{c} - \bar{c}_m)^2$.

It is evident from the two

figures that both the mean and the second moment of the conserved scalar across the width of the shear layer are accurately predicted by our computations.

U2 = 0.5000, RE = 10000
TIME = 20.00



U2 = 0.5000, RE = 10000
TIME = 20.00



U2 = 0.5000, RE = 10000
TIME = 20.00

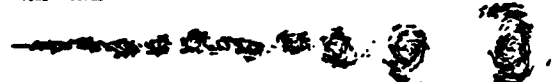


Figure 5. Vorticity field at $Re = 10000$, $U2/U1 = 0.5$.

U2 = 0.5000, RE = 10000
TIME = 20.00



U2 = 0.5000, RE = 10000
TIME = 20.00



U2 = 0.5000, RE = 10000
TIME = 20.00



Figure 6. Scalar's velocity field at $Re = 10000$, $U2/U1 = 0.5$.

U2 = 0.5000, RE = 10000

TIME = 20.00



U2 = 0.5000, RE = 10000

TIME = 20.00



U2 = 0.5000, RE = 10000

TIME = 20.00



Figure 7. Concentration field at $Re = 10000$, $Pe = 4000$, $U2/U1 = 0.5$.

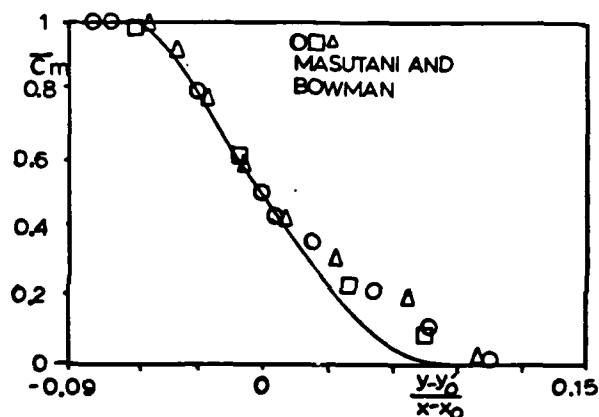


Figure 8. Normalized mean concentration profile as a function of the cross-stream coordinate.

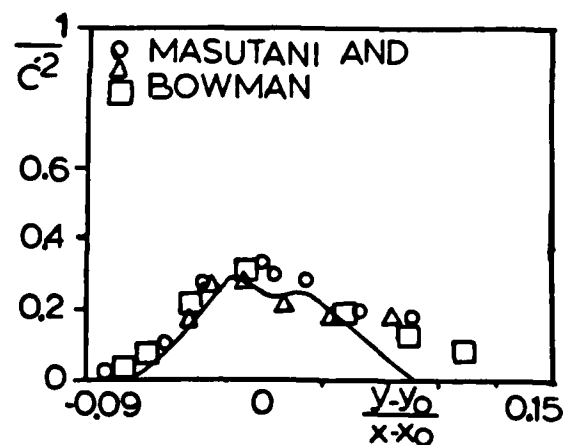


Figure 9. Normalized rms concentration profile as a function of the cross-stream coordinate.

We note that the results in Figs. 8 and 9 are in better agreement with experimental data than those previously predicted by Givi et al. [31]. In these calculations, a $k-\epsilon$ turbulence model and a gradient diffusion model for turbulent transport of the scalar mean, moment and probability density function was utilized. In the $k-\epsilon$ calculations, the concentration fluctuations exhibit a fairly smooth bell-shaped profile with a much less clear double "hump" in the middle region, indicating poor agreement near the high speed stream. The present calculations show the two local maxima in the fluctuation profiles that correspond to the location where the gradient of the mean value is highest. The same behavior is observed by the experimental results of Masutani and Bowman [30] and Batt [32]. It is clear that, in accordance with the findings of Broadwell and Briedenthal [33], the intermittency caused by the large coherent structures contributes greatly to the statistics of turbulent flows.

III.2 REACTING MIXING LAYER

In the calculation of a reacting mixing layer, two reactants F and O are introduced on both sides of the splitter plate. At $x = 0$, for $y > 0$, $c_F = 1$ and $c_O = 0$, and for $y < 0$, $c_O = 1$ and $c_F = 0$, while $c_p = 0$. As reactants are entrained into the mixing cores of the layer, they diffuse across the original interface and chemical reaction proceeds. The rollup and pairing increases the original length of the interface by many folds and allow the entrained fluid to diffuse along a larger boundary (Ghoniem et al. [34]). During this process, if the Lagrangian elements utilized to represent the interaction between chemically reacting species are brought close enough so that the distance between two neighboring elements is smaller than the characteristic diffusion length, they react at the rate defined by Eq. (17).

In Figs. 10, 11 and 12, we present the velocity, location and the strength of the elements in terms of product concentration for the reacting mixing layer with constant rate chemical kinetics and temperature-dependent reaction rate, respectively. The amount of the products formed due to chemical reaction is represented by the diameter of the circles in the figures, i.e. larger circles indicate more products. In both cases, $Re = 10000$, $Pe = 4000$, and $U_2/U_1 = 1/3$ while $Le=1$. In the constant rate kinetics case, the value of the Damkohler number $Da = 1$ and in the temperature-dependent kinetics $Da = 200$, $T_a = 10$ and $Q = 5$. Note that in both cases the value of the non-dimensional kinetic parameters are low enough so that the effects of heat release on the fluid dynamics can be negligible. The stiffness of Eq. (19) for large values of the Damkohler number imposes a restriction on the time step of integration. In these calculations, we found that $\Delta t = 0.1$ is sufficiently small to accurately integrate the slow chemistry.

A comparison between the two figures reveal that under isothermal conditions, the products are formed as mixing occurs just downstream of the splitter plate, while in the temperature-dependent kinetics calculations, there is an ignition delay before the reactant reach a temperature high enough to allow any significant chemical reaction to occur. Once the reaction begins, the mechanism

U2 = 0.3333, Re = 10000

TIME = 18.00.



U2 = 0.3333, Re = 10000

TIME = 20.00.



U2 = 0.3333, Re = 10000

TIME = 21.00.



Figure 10. Scalar's velocity field at $Re = 10000$, $U_2/U_1 = 1/3$.

U2 = 0.3333, Re = 10000

TIME = 18.00.



U2 = 0.3333, Re = 10000

TIME = 20.00.



Figure 11. Product concentration field, $Re = 10000$, $Pe = 4000$, $U_2/U_1 = 1/3$, isothermal reacting layer.

U2 = 0.3333, Re = 10000

TIME = 18.00.



U2 = 0.3333, Re = 10000

TIME = 20.00.



Figure 12. Product concentration field, variable temperature reacting layer.

of product formation and chemical reaction in both cases are asymptotically the same. Increasing the Damkohler number to $Da = 400$ results in a shorter ignition delay, and preheating the reactants by increasing the temperature at the inlet to $T_1 = Q/2$ while $Da = 200$, eliminates the ignition delay as indicated in Figs. 13 and 14, respectively.

In order to examine the effects of chemical reaction on the transport of species, the concentration statistics in the temperature-independent reaction case are presented in Figs. 15 and 16. These figures correspond to the ensemble mean and fluctuation in the bottom-stream species concentration in a reacting mixing layer with $Da = 1$, $U_2/U_1 = 1/2$, $Re = 10000$, and $Pe = 4000$. A comparison between figures 15 and 8, and between figures 16 and 9 indicates that near the free stream, the chemistry affects the statistical behavior of the species. Near the reaction zone, however, the mean and the rms values of the concentration are lower under reacting conditions, while the second hump near the high speed stream side of the rms profile in the non-reacting layer is eliminated in the reacting flow due to the local consumption of the species by chemical reaction. The same behavior was also observed in the experiments of Masutani and Bowman [30] in a reacting mixing layer under isothermal conditions. Their results, however, can not be compared quantitatively with the present calculations since the values of the chemical parameters employed in the numerical simulation are substantially lower than those of the experiment.

Q2 = 0.5000, RE = 10000
TIME = 20.00

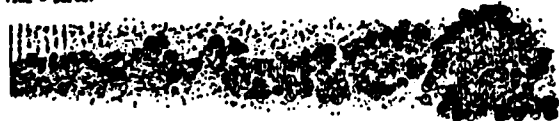


Figure 13. Product concentration field, variable temperature reacting layer.

Q2 = 0.5000, RE = 10000
TIME = 18.00



Q2 = 0.5000, RE = 10000
TIME = 20.00



Q2 = 0.5000, RE = 10000
TIME = 21.00



Figure 14. Product concentration field, variable temperature reacting layer.

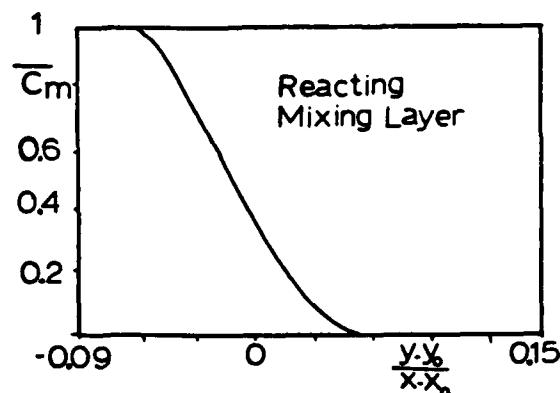


Figure 15. Normalized mean concentration profile as a function of the cross-stream coordinate.

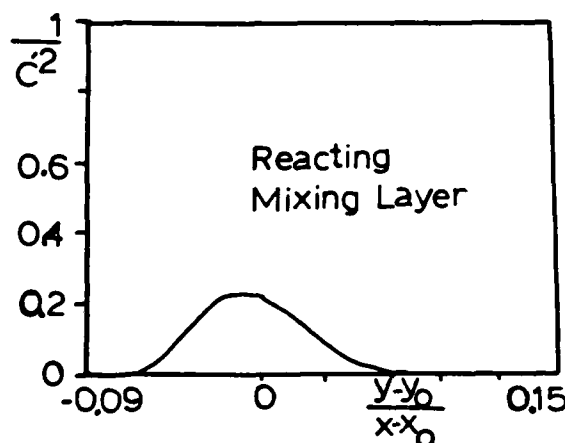


Figure 16. Normalized rms concentration profile as a function of the cross-stream coordinate.

III.3 EFFECT OF HARMONIC FORCING

The dynamic effect of oscillating the upstream side of the layer was studied experimentally by several authors, e.g. Oster and Wygnanski [35] and Roberts and Roshko [21] and numerically by Ghoniem and Ng [22]. Their results indicate that in the forced case, eddy interactions follow four stages. In the first stage, the layer rolls up at the harmonic of the forcing frequency closest to the most amplified mode. In the second stage, a process of accelerated pairings yields a large eddy which is in tune with the forcing frequency. This large resonant eddy appears earlier than it would appear in the case of an unforced layer. In the third stage, pairing among resonant eddies, which represents a neutrally stable mode, is disabled and the growth of the vorticity layer is impaired for several eddies downstream. In the fourth stage, the effect of forcing diminishes and pseudo-random pairing is resumed. Moreover, velocity statistics is affected by forcing, and the sign of momentum transfer across the layer is reversed following pairing. Entrainment of passive particles was found to be commensurate with the development of the vorticity layer.

In the recent experiment by Roberts and Roshko [21], it has been observed that periodic forcing has a direct influence on the outcome of chemical reaction across a turbulent shear layer. The results of this experiment indicate that when harmonic forcing is applied, the mixing rate: (1) is increased in the initial stages where the resonant eddy is forming; (2) is decreased in the intermediate stage which corresponds to the resonant or "frequency-locked" region; and, (3) is the same as that of the unforced layer further downstream. In order to characterize these three regions, the Wygnanski-Oster parameter $X_w = \Delta U \Omega x / U_m^2$ is utilized, where Ω is the forcing frequency [35]. Roberts and Roshko [21] and Browand and Ho [36] show that the three different regions can be classified according to the local value of X_w parameter. In region I, $X_w < 1$, the growth rate is enhanced. In region II, $X_w > 1$, the frequency-locked region, the growth rate is inhibited. In region III, the growth rate relaxes to that of the unforced layer.

In order to investigate this phenomenon computationally, the response of the reacting shear layer to the application of low frequency, low amplitude perturbations on the upstream side of the shear layer is computed. Streamwise oscillations are applied on both sides of the layer, hence a pressure perturbation is imposed without changing the vorticity field. The streamwise velocities are taken as $U_1 = 1 + a \sin(2\pi\Omega t)$, and $U_2 = a U_2$, where a is the amplitude of forcing.

The normalized distribution of the product thickness along the mixing layer for three cases, $\Omega = 0, 0.5$ and 1 , is shown in Fig. 17. In these calculations, $a = 0.1$, and $Re = 4000$. The figure indicates that for $\Omega = 1$, mixing is enhanced in the initial part of the layer, $1 \leq x \leq 2$. The resonant, frequency-locked region begins at $x = 2$ and ends at value $x \sim 3$. In this region, mixing is reduced and is less than that of unforced mixing layer. Downstream of this region, $x \geq 3$, mixing rate resumes its natural growth and reaches asymptotically that of the unforced layer. For lower forcing frequency, $\Omega = 0.5$, the same overall behavior is observed. In this case, however, the results of numerical calculations indicate that the resonant frequency-locked region is approximately in the range $3 \leq x \leq 4$. A comparison between the range of the frequency locked region calculated here with that estimated by Browand and Ho [36] is shown on Table I. Considering the fact that our simulations ignore the effect of small scale three-dimensional turbulence motion, and considering the non-universality of the Browand and Ho's curve due to its independence to experimental conditions and other important non-dimensionalized parameters, this agreement is encouraging.

TABLE I

Ω	frequency locked region	
	calculated	measured [36]
0.5	$3 \leq x \leq 4$	$2.66 \leq x \leq 5.33$
1.0	$2 \leq x \leq 3$	$1.33 \leq x \leq 2.66$

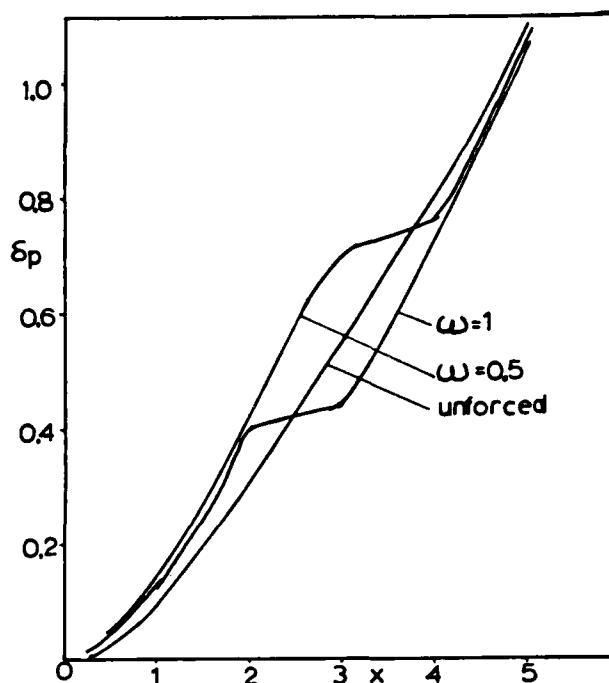


Figure 17. Variation of the product thickness versus the downstream distance.

III.4 EFFECT OF STRAIN RATE

It has been shown experimentally by Tsuji [37], numerically by Liew et al. [38], and analytically by Peters [39], that the strain rate has a major influence on the flame structure, particularly in non-premixed systems. In the counter-flow diffusion flame experiment of Tsuji [37], it was observed that increasing the magnitude of stretch near the flame surface results in an increase of the flow of reactants into the reaction zone. As a result, the chemical reaction is not able to keep pace with the supply of reactants, and the reaction rate is reduced until local flame quenching occurs. The analysis of Peters [39], which is based on the method of matched asymptotic expansion at large activation energy, shows that the mechanism of flame extinction can be addressed by examining the local value of the rate of scalar dissipation. This parameter is viewed by Peters [39] as the inverse of the diffusion time scale. If the local value of dissipation is increased beyond a critical limit, the heat conducted away from of the diffusion flame can not be balanced by the heat produced by the chemical reaction. As a result, the maximum value of the temperature decreases, and the reaction eventually ceases.

By increasing the number of scalar elements to 38 in each stream while decreasing the computational domain to $X_{max} = 4$, and by preheating the incoming reactants to $T_i = Q/2$ to start the chemical reaction immediately downstream the splitter plate, we were able to observe this phenomenon. Figures 18 and 19 show the

instantaneous velocity and temperature rise, $T-T_i$, of the scalar elements at times of $t = 19$ and $t = 21$, respectively. In this case, the Damkohler number, the normalized enthalpy of reaction, the activation energy and the velocity ratio at the inlet are 50, 8, 20 and $1/3$, respectively. The cross stream direction is enlarged by a factor of 2 for the purpose of clarity.

The figures show that the number of scalar elements near the braid, which is the thin link between two neighboring cores, is only a small portion of the total number of elements within the computational domain, which reached more than 5100. This indicates an instantaneous quenching at the stagnation points of the layer. Moreover, the temperature and product concentration in the reaction zone reach a maximum at the core of the eddies where the vorticity concentration is high, while they reach a minimum at the stagnation point within the braid between the neighboring cores where the strain and the scalar gradients reach their maximum values. This is consistent with the results of the pseudo-spectral calculations of Givi et al. [15], and with the experimental observations of Tsuji [37] who showed that the local extinction of diffusion flames occurs mainly at the regions of high dissipation rate. At these regions, the temperature tends to decrease, and if it goes below a critical characteristic value, the flame locally extinguishes.

Quantitative analysis of the effects of stretch on the chemical reaction is rather difficult in the context of present algorithm. This is due to the fact that there are very few scalar elements near the regions of high strain, and as shown by Ghoniem et al. [34], most of the elements tend to be concentrated near the regions with low dissipation. Implementation of a numerical scheme based on the transport of the scalar gradients, as in Ghoniem et al. [34] can improve the accuracy of the analysis substantially, particularly those associated with the effects of stretch. In this method, the elements are concentrated near the regions of

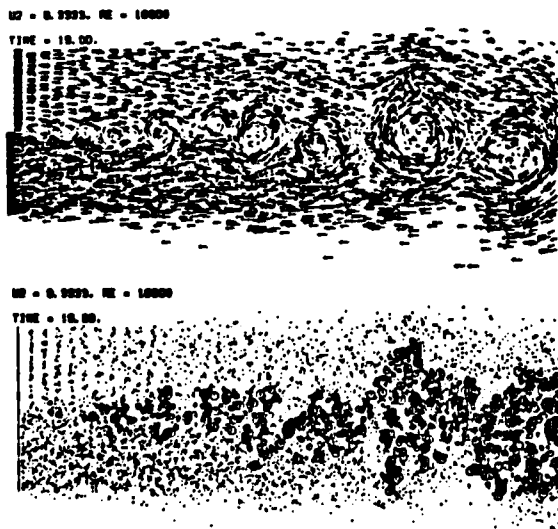


Figure 18. Temperature field for reacting mixing layer.

U2 = 0.5233, RE = 10000

TIME = 21.00



U2 = 0.5233, RE = 10000

TIME = 21.00



Figure 19. Temperature field for reacting mixing layer.

large gradients, or high dissipation, and hence a smaller total number of elements have to be considered. The implementation of this method for the numerical simulation of unpremixed reacting flows is presently underway to study the effect of strain rate more accurately.

IV CONCLUSIONS

In this work, a numerical scheme based on the transport of computational elements carrying vorticity and scalar quantities has been developed to simulate a reacting planar, two-stream mixing layer with unmixed reactants. The scheme solves the transport equations at high Reynolds and Peclet numbers without using models for turbulence closure. A Lagrangian stochastic model is used to implement the chemical reactions for both constant rate kinetics and variable temperature Arrhenius reactions.

In the non-reacting flow simulations, the calculated statistics of the mixing of a conserved scalar are in good agreement with experimental data. In particular, the numerical results show the presence of two maxima in the fluctuation profile. In the constant rate reacting flow simulation, the effect of chemistry is to smooth out this curve and produce a single maximum, which agrees with the experimental observations. Harmonic forcing enhances the mixing within the accelerated growth zone of the vorticity layer, while it impairs the entrainment of the unmixed fluid into the cores in the resonating region. As a result, the numerical simulation indicates a decrease in the rate of product formation in the frequency-locked region, similar to previous experimental findings.

In the Arrhenius, temperature-dependent kinetics, the mechanism of ignition delay and the effects of reactants preheating on the decrease of the duration of this delay is observed. Also, the

non-equilibrium coupling between the scalar dissipation rate and the flame structure is revealed as quenching frequently appears within the braids. To describe this phenomenon more accurately, work is underway to construct a higher order scheme which can provide better resolution at the regions of strong strain rates.

ACKNOWLEDGEMENT

The work of AFG is supported by the Air Force Office of Scientific Research Grant AFOSR 84-0356, the National Science Foundation Grant CPE-840481, and the Edgerton Associate Professorship at MIT. Part of this work was performed while PG was on leave at the Institute for Computational Mechanics in Propulsion at NASA Lewis Research Center. The authors appreciate the support of NASA Lewis in providing computer time on the CRAY-XMP. The help of Mr. Don Lovell of Flow Research Company in vectorizing the codes and in providing graphics routines is gratefully acknowledged.

REFERENCES

1. Bilger, R.W. "Turbulent Flows with Nonpremixed Reactants", Turbulent Reacting Flows, Springer-Verlag, Berlin, 1980, pp. 65-113.
2. Donaldson, C. duP., and Varma, A.K., "Remarks on the Constructions of a Second-Order Closure Description of Turbulent Reacting Flows", Combust. Sc. and Tech., Vol. 13, 1976, pp. 55-78.
3. Givi, P., Ramos, J.I., and Sirignano, W.A., "Turbulent Reacting Concentric Jets: Comparison Between PDF and Moment Calculations", AIAA Prog. Astron. and Aeron., Vol. 95, 1984, pp. 384-448.
4. Bilger, R.W., "Turbulent Jet Diffusion Flames", Prog. Energy and Combust. Sc., Vol. 1, 1976, pp. 87-109.
5. Lockwood, F.C. and Naguib, A.S., "The Prediction of the Fluctuations in the Properties of Free, Round Jet, Turbulent, Diffusion Flames", Combust. Flame, Vol. 24, 1975, pp. 109-124.
6. Givi, P., Sirignano, W.A. and Pope, S.B., "Probability Calculations for Turbulent Jet Flows with Mixing and Reaction of NO and O₃", Combust. Sc. Tech., Vol. 37, 1984, pp. 599-74.
7. Nguyen, T.V. and Pope, S.B., "Monte-Carlo Calculations of Turbulent Diffusion Flames", Combust. Sc. Tech., Vol. 42, 1984, pp. 13-45.
8. Pope, S.B. and Correa, S.M., "Joint PDF Calculations of A Non-Equilibrium Diffusion Flame", Proceedings of 21st Symposium (Int.) on Combustion, Combustion Institute, Pittsburgh, PA., to appear, 1987.
9. Ghoniem, A.F., "Computational Methods in Turbulent Reacting Flows", Lectures in Applied Mathematics, Vol. 24, 1986, 199-265.
10. Oran, E.S. and Boris, J.P., Numerical Simulation of Reactive Flows, to be published by Elsevier Science Publishing Co., 1987.
11. Corcos, G.M. and Sherman, F.S., "The mixing layer: deterministic models of a turbulent flow. Part 1: Introduction and the two-dimensional flow", J. Fluid Mech., Vol. 139, 1984, pp. 29-65.
12. Grinstein, F.F., Oran, E.S. and Boris, J.P., "Numerical simulations of asymmetric mixing in planar shear flows", NRL Memorandum Report 5621, Washington, D.C., 1985.
13. Riley, J.J., Metcalfe, R.W. and Orszag, S.A., "Direct numerical simulations of chemically reacting turbulent mixing layers", Phys. fluids, Vol. 29, 1986, pp. 406-422.
14. McMurtry, P.A., Jou, W.H., Riley, J.J., and Metcalfe, R.W., "Direct numerical simulations of a reacting mixing layer with chemical heat release", AIAA Journal, Vol. 24, Number 6, 1986, pp. 962-970.
15. Givi, P., Jou, W.H. and Metcalfe, R.W., "Flame extinction in a temporally evolving mixing layer", Proceedings of 21st Symposium (International) on Combustion, The Combustion Institute, Pittsburgh, PA, to appear.
16. Givi, P. and Jou, W.H., "Mixing and chemical reaction in a spatially developing mixing layer," Presented at the Central States Section Meeting of The Combustion Institute, Cleveland, OH, May 1986.
17. Ghoniem, A.F., Chorin, A.J. and Oppenheim, A.K. "Numerical modelling of turbulent flow in a combustion tunnel," Phil. Trans. R. Soc. Lond., Vol. A304, 1982, pp. 303-325.
18. Sethian, J.A., "Turbulent combustion in open and closed vessels," J. Comput. Phys., 54, 3, 1984, pp. 425-456.
19. Ashurst, W.T. and Barr, P.K., "Lagrangian-eulerian calculation of turbulent diffusion flame propagation", Sandia Report SAND80-9950, Sandia National Laboratories, 1982.
20. Lin, P. and Pratt, D.T., "Numerical simulation of a plane mixing layer, with applications to isothermal, rapid reactions", AIAA Paper 87-0225, 1987.
21. Roberts, R.A. and Roshko, A., "Effects of periodic forcing on mixing in turbulent shear layers and wakes", AIAA Paper No. 85-0570, Jan. 1985.
22. Ghoniem, A.F. and Ng, K.K., "Numerical study of a forced shear layer," Phys. fluids, in press, 1987, and AIAA Paper 86-0056, 1986.
23. Chorin, A.J., "Numerical study of slightly viscous flow", J. Fluid Mech., Vol. 57, 1973, pp. 785-796.

24. Hald, O., "The convergence of vortex methods", SIAM J. Numer. Anal., Vol. 22, 1979, pp. 726-755.
25. Beale, J.T. and Majda, A., "Vortex methods II: higher order accuracy in two and three dimensions", Math. Comput., vol. 39, 1982, pp. 29-52.
26. Ghoniem, A.F. and Gagnon, Y., "Vortex simulation of recirculating flow at moderate Reynolds numbers", J. Comput. Phys., 67, in press (1987) and AIAA Paper, 86-0370, 1986.
27. Ghoniem, A. F. and Oppenheim, A. K., "Numerical solution of the problem of flame propagation by the use of the random element method," AIAA Journal, 22, 10, pp. 1429-1435, 1984.
28. Ghoniem, A. F. and Sherman, F. S., "Grid-free simulation of diffusion using random walk," J. Comput. Phys., 61, pp. 1-37, November 1985.
29. Koochesfahani, M.M., "Experiments on turbulent mixing and chemical reactions in a liquid mixing layer", Ph.D. Thesis, Calif. Inst. of Technology, Pasadena, CA, 1984.
30. Masutani, S.M., and Bowman, C.T., "The structure of a chemically reacting plane mixing layer", Paper 84-44, Western States Section/The Combustion Institute Meeting, Boulder, Colorado, 1984.
31. Givi, P. Ramos, J.I. and Sirignano, W.A., "Probability density function calculations in turbulent, chemically reacting round jets, mixing layers and one-dimensional reactors", Journal of Non-Equilibrium Thermodynamics, Vol. 10, No. 2, 1985, pp. 75-104.
32. Batt, R.G., "Turbulent mixing of passive and chemically reacting species in a low-speed shear layer", J. Fluid Mech., Vol. 82, 1977, pp. 53-95.
33. Broadwell, J.E. and Breidenthal, R.E., "A Simple model of mixing and chemical reaction in a turbulent shear layer", J. Fluid Mech., Vol. 125, 1982, pp. 397-410.
34. Ghoniem, A.F., Heidarienejad, G. and Krishnan, A. "Computation of a thermally stratified mixing layer," J. Comput. Phys., submitted for publication.
35. Oster, D. and Wagnanski, I., "The forced mixing layer between parallel streams", J. Fluid Mech., Vol. 123, 1982, pp. 91-130.
36. Browand, F.E. and Ho, C.M., "The mixing layer: An example of quasi two-dimensional turbulence", Journal de Mecanique theorique et Appliquee Numero Special, 1983, pp. 99-120.
37. Tsuji, H. "Counter-flow diffusion flames", Prog. Energy Combust. Sci., Vol. 8, 1982, p. 93.
38. Liew, S.K., Moss, J.B., and Bray, K.N.C.; "Predicted structure of stretched and unstretched methane-air diffusion flame", AIAA Prog. in Astron. and Aeron., Vol. 95, 1984, pp. 305-319.
39. Peters, N., "Laminar diffusion flamelets models in non-premixed turbulent combustion", Prog. Energy Combust. Sci., vol. 10, 1984, pp. 319-339.

Appendix IV

The paper on "Three dimensional vortex simulation with application to an axisymmetric shear layer" describes the three dimensional vortex element method and its application to the evolution of the azimuthal instability on a vortex ring and the initial stages of development of a turbulent jet.

AIAA'87

AIAA-87-0379

**Three-Dimensional Vortex Simulation
with Application to Axisymmetric
Shear Layer**

**A.F. Ghoniem, H.M. Aly, and O.M. Knio
Massachusetts Institute of Technology
Cambridge, MA 02139**

AIAA 25th Aerospace Sciences Meeting

January 12-15, 1987/Reno, Nevada

**For permission to copy or republish, contact the American Institute of Aeronautics and Astronautics
1633 Broadway, New York, NY 10019**

THREE DIMENSIONAL VORTEX SIMULATION WITH APPLICATION
TO AXISYMMETRIC SHEAR LAYERS

Ahmed F. Ghoniem* and Omar M. Knio**
Department of Mechanical Engineering
Massachusetts Institute of Technology
Cambridge, MA 02139

and

Hany M. Aly***
Department of Mechanical Engineering
and Engineering Science
University of North Carolina
Charlotte, NC

ABSTRACT

A three dimensional vortex element method is developed for the numerical simulation of incompressible flow at high Reynolds number. The method utilizes vortex vector elements with finite point-symmetric cores to discretize the vorticity field. The transport of these elements is done in Lagrangian coordinate by computing the velocity field as a summation over the individual contributions of the elements.

The method is used to compute the self-induced velocity of a vortex ring and the stability of a vortex ring with finite core. Results show that vortex rings become unstable to a particular azimuthal perturbation that depends on the core/radius ratio. The mode frequency and shape of the unstable state are in excellent agreement with analytical and experimental results. The method is applied to study the rollup of an axisymmetric shear layer and the generation of large scale vortex ring structures.

1. INTRODUCTION

At high Reynolds numbers, vorticity occupies a small subset of the volume of the flow field. This is exemplified by boundary layers, shear layers, wakes, jets, separation and recirculation zones, etc. These vorticity distributions are unstable to natural perturbations. At small amplitudes, perturbations grow exponentially in time, however, they have a limited effect on the flow. The growth of these perturbations into the non-linear stages is, however, accompanied with severe distortions of the shape of the vorticity field and strong changes in the local concentration of vorticity. Examples for these changes is the formation of large scale structures in shear layers and recirculation zones.

In highly three-dimensional flows, several forms of instability may arise simultaneously. The evolution of spanwise waves on the large scale eddies and the development of azimuthal instability along the axis of vortex rings have been observed experimentally as evidence of multiple forms of instability. In this case, the distortion of the vorticity field occurs faster and the non-linearity is compounded by the interaction between different instability modes. Moreover, the problem is governed by several length and time scales, and multiple states can be expected depending on which mode grows faster (for photographic record of the development of vorticity fields, see Van Dyke [1] and Lugt [2]).

It has been reported experimentally, and observed in numerical studies, that these changes in the vorticity field may not incur strong variations in the mean flow field. This is expected since the velocity is an integral mean of the vorticity field. However, they affect the fluctuations strongly and to the level where the order of magnitude of the fluctuation may change. This is extremely important in mixing and heat release in chemically reacting flows since the rate of mixing, and thus chemical reaction, is a strong function of the fluctuation and depends weakly on the mean field. It has been confirmed that by changing the vorticity field of a shear layer through imposing certain perturbations on the flow, the rate of chemical reaction can be enhanced or slowed and that turbulent shear stresses can reverse sign during the same process (for a review and some recent results, see Ho and Huerre [3], Robert and Roshko [4] and Ghoniem and Ng [5]).

To capture these changes, numerical simulation of the unaveraged non-linear equations of motion has been utilized. For the success of these simulations, care must be exercised in resolving small variations since they ultimately grow to produce the finite amplitude changes, and hence numerical diffusion should be minimized. Moreover, schemes must adapt to the strong distortion in the flow field without developing numerical instabilities. Thus, Lagrangian schemes seem like natural candidates. A grid-free class of Lagrangian schemes, vortex methods, is utilized in this work to study the evolution of three

Copyright © 1987 by A.F. Ghoniem. Published by the American Institute of Aeronautics and Astronautics, Inc., with permission.

* Associate Professor, Associate Fellow AIAA.

** Research Assistant

***Assistant Professor, Member AIAA.

dimensional flow fields dominated by high concentration of vorticity at high Reynolds numbers.

In vortex simulation, vorticity distribution is represented by a finite number of localized vortex elements, or vortex disks in two dimensions (blobs according to Chorin [6]), and vortex balls in three dimensions (vortons according to Saffman and Merion [7], or vortex arrows according to Leonard [8]) which move in an inviscid field with the local particle velocity. A particular flow configuration can be fully described when the appropriate boundary conditions are imposed on the velocity field by adding an extra irrotational field. Two-dimensional vortex simulations have been useful in providing an accurate description of the large-scale structure of turbulence in shear flows (Ashurst [9], Ghoniem and Sethian [10] and Ghoniem and Ng [5]). However, they cannot be used to describe phenomena in which streamwise vorticity, or variation along vortex lines, plays an important role. Moreover, they lack the ability to capture small-scale turbulence structures which arise due to vortex stretching and tilting with respect to the main flow plane.

In this work, a three dimensional vortex element method is developed for the numerical simulation of flow field with high concentration of vorticity at high Reynolds number. The scheme utilizes vortex vector elements with finite point-symmetric cores to discretize the vorticity field and follows their motion in Lagrangian coordinates. The vortex vector elements change their vorticity according to the local stretch, while their direction is determined by the tilting of the vortex lines. The rotational velocity field is computed by summing over the field of each individual element, which is evaluated from the desingularized Biot-Savart law. The potential velocity added to satisfy the boundary conditions is computed by using the appropriate image system of the vortices. For recent reviews of vortex calculations in three dimensions, see Leonard [8,11] and Saffman and Baker [12].

To check the accuracy of the vortex method, we use test problems and make comparison with experimental and analytical results. The discretization algorithm is applied to compute the self-induced velocity of a vortex ring and the results are compared with the Saffman's analytic solution [13]. The stability results of a vortex ring with a finite non-deformable core and a vortex torus with a deformable core are compared with the analytical solutions of Widnall and Sullivan [14] and Widnall et al. [15]. Preliminary results for the rollup of a three dimensional shear layer subject to an axisymmetric perturbation are compared with the experimental results of Vandsburger et al. [16] and Roquemore et al. [17].

II. FORMULATION AND NUMERICAL SCHEME

In this section, the construction of a three-dimensional scheme for tracking the evolution of a vorticity structure in an arbitrary domain is described. The accuracy of the scheme is checked against theoretical results regarding the motion

and stability of a vortex ring and a vortex torus. The scheme is constructed as follows: The vorticity field is first discretized into a finite number of small straight line vortex vector elements and then followed in a Lagrangian frame of reference. Each element has a finite core of vorticity which is point-symmetrical around its center, and hence the nomenclature "vortex ball". The velocity produced by a distribution of vortex vector elements, or vortex balls, is obtained by the desingularized Biot-Savart law, which amounts to summing the velocity produced by individual vector elements. The procedure for a consistent discretization and the evaluation of the Biot-Savart law is explained in Section II.2. Its numerical accuracy and convergence under steady state conditions is shown in Section II.3. The comparison between the numerical and analytical results for the stability of a thin vortex ring and a vortex torus, another test for the accuracy of the method under unsteady state, is discussed in Sections II.4 and II.5.

The potential velocity field added to satisfy a particular set of conditions on the boundaries is determined by solving the Laplace equation numerically subject to the appropriate boundary conditions. When the boundary conditions match those of a standard potential solver, i.e. Dirichlet or Neumann conditions, that particular routine can be used to evaluate the potential velocity. In cases when the boundary conditions are neither Dirichlet nor Neumann type, one faces difficulty in satisfying continuity along the boundaries, and a special algorithm must be constructed to handle this difficulty. This is discussed in Section III.

II.1. EQUATIONS OF MOTION

The motion of an incompressible inviscid flow is governed by the Euler equations:

$$\nabla \cdot \mathbf{u} = 0 \quad (1)$$

$$\frac{\partial \mathbf{u}}{\partial t} + \mathbf{u} \cdot \nabla \mathbf{u} = -\nabla p \quad (2)$$

expressing the conservation of mass and momentum, respectively. In these equations, $\mathbf{u} = (u, v, w)$ is the velocity, t is time, $\nabla = (\partial/\partial x, \partial/\partial y, \partial/\partial z)$ is the gradient operator, while $\mathbf{x} = (x, y, z)$, and p is pressure. Quantities are normalized with respect to the appropriate combination of a characteristic length scale, velocity scale and density. In vortex simulation, the equations are recast in terms of the vorticity ω :

$$\omega = \nabla \times \mathbf{u} \quad (3)$$

The vortex transport equations are obtained by taking the curl of Eq. (2). Using Eq. (1) and using the fact that $\nabla \cdot \omega = \nabla \cdot \nabla \times \mathbf{u} = 0$, i.e. the vorticity forms a solenoidal vector field, we get:

$$\frac{\partial \omega}{\partial t} + \mathbf{u} \cdot \nabla \omega = \omega \cdot \nabla \mathbf{u} \quad (4)$$

If the vorticity field is known, the velocity can be evaluated by integrating Eqs. (1) and (3), as shown below, while Eq. (4) is used to transport the vorticity in the form of a number of discrete

elements. This is, in essence, the backbone of vortex simulation algorithms.

Based on the Helmholtz decomposition of a vector field, the velocity can be split into a solenoidal and an irrotational component,

$$u = u_\omega + u_p \quad (5)$$

where u_ω is the velocity induced by the vorticity field in an unbounded space, and u_p is the potential component added to satisfy the potential no-flow condition along the boundary of the domain. Each component will be evaluated separately, satisfying the appropriate boundary conditions, and then added to obtain the total velocity.

To evaluate the velocity field induced by a given vorticity distribution ω in an unbounded space, we assume the existence of a vector stream function ψ such that

$$u_\omega = \nabla \times \psi \quad (6)$$

By construction, u_ω satisfies the continuity

equation since $\nabla \cdot \nabla \times \psi = 0$ identically. Substituting in Eq. (3) and assuming that $\nabla \cdot \psi = 0$, one obtains:

$$\nabla^2 \psi = -\omega \quad (7)$$

The solution of this Poisson equation in three dimensions is given by:

$$\psi(x) = \int G(x - x') \omega(x') dx' \quad (8)$$

where $G(x) = 1/(4\pi r)$ is the Green function, and $r = |x|$. As shown by Batchelor [18], the above expression for ψ is solenoidal, as previously assumed, if the boundaries of the domain extend to infinity. This is essentially the condition needed to evaluate u_ω .

The solenoidal velocity component, u_ω , can be evaluated by substitution in Eq. (6) which yields the well-known Biot-Savart law:

$$u_\omega = \int K(x-x') \times \omega(x') dx' \quad (9)$$

$$K(x) = -\frac{1}{4\pi} \frac{x}{r^3} \quad (10)$$

where x' is the position of the volume element dx' .

The implications of the equations of motion, Eqs. (3) and (4), regarding the evolution of the vorticity field can be summarized in the following important dynamical statements, given here without proof while used later in the construction of the numerical algorithm (for details, see Batchelor [18]):

(1) Kelvin theorem: The circulation around a closed material loop, defined as $\Gamma = \oint_A \omega \cdot dA$ where A is the surface area within the loop, is conserved as the loop is deformed;

(2) Helmholtz theorem: Vortex lines, parallel everywhere to the local vorticity vector, move as material lines.

Furthermore, the vorticity vector can be written as $\omega = \omega \mathbf{e}$, where \mathbf{e} is the direction of the local vortex line, or material lines, while $dx = dA \cdot d\mathbf{e}$ where A is the cross sectional area normal to the direction \mathbf{e} . The circulation of a vortex line, Γ , which is conserved along a particle path according to Kelvin theorem, is expressed in terms of the vorticity ω as $\Gamma = \oint_A \omega \cdot dA$.

Since u_p is an irrotational component, then $u_p = \nabla \phi$, where ϕ is a velocity potential governed by:

$$\nabla^2 \phi = 0 \quad (11)$$

while the total velocity, u , is subject to a potential boundary condition at the boundaries of the domain, i.e. $(u_\omega + \nabla \phi) \cdot n$ is given on ∂D , where n is the local normal to ∂D , which denotes the boundary of the domain.

II.2. EVALUATION OF THE ROTATIONAL FIELD

Analytical evaluation of the Biot-Savart integral in Eq. (9) is restricted to simple vorticity distributions, such as rectilinear vortices and circular vortex rings of concentrated vorticity. Therefore, the integration must be performed numerically for an arbitrary vorticity distribution. For that purpose, the continuous vorticity field is discretized into a number of vortex vector elements, each with an assigned vorticity ω_i . The magnitude of the vorticity

associated with each element is distributed over a small spherical volume around its center according to a core function f with a characteristic core radius δ . The vorticity field is hence expressed as:

$$\omega(x,0) = \sum_{i=1}^N \omega_i(0) h^3 f_\delta(x - X_i) \quad (12)$$

where N is the total number of vortex vector elements, and X_i is the center of the vortex

element, while h is the initial distance between the centers of neighboring elements. The accuracy of this discretization is discussed in Seale and Majda [19,20]. Note that if $f_\delta = \delta(x - X_i)$, where

$\delta(\cdot)$ is the Dirac delta function, Eq. (12) represents a distribution of singular vortex lines, or vortons [7]. However, in this representation, vortex balls, while equivalent to vortex disks in two dimensions, are used and $f_\delta =$

$1/\delta^3 f(r/\delta)$, while δ is finite. The distribution of the magnitude of the vorticity associated with each element is point symmetrical around its center X_i , while its direction everywhere is $\mathbf{e} = \omega_i/\omega_i$, and $\omega = |\omega|$. δ is the core radius of the element where most of its vorticity is concentrated, $f > 0$ for $r < \delta$, and f vanishes rapidly for $r > \delta$.

A simple intuitively appealing choice for a core function could be the Hill spherical vortex for which $\omega = A/\rho$ for $\rho < \delta$ and $\omega = 0$ for $\rho > \delta$,

where $\rho^2 = x^2 + y^2$, ρ being the radial direction in a cylindrical coordinate system. This, however, is a poor choice for the core function since the latter should have a maximum at the center and decay further away. Moreover, ω is not a function of r . A better choice may be the three dimensional analogue of the Rankine vortex, i.e. $\omega = \omega_0$ for $r \leq \delta$ and $\omega = 0$ for $r \geq \delta$.

For accurate discretization of the continuous vorticity distribution, δ should be chosen larger than h , where h is the initial separation between the elements and h^3 is the volume element used to construct the vortex balls. This will ensure that the core functions f associated with neighboring elements are highly overlapping. The introduction of a similar discretization procedure has been widely used in two dimensional simulations to construct stable and accurate vortex algorithms [5,6,8,9,19]. Moreover, h may take on different values in the three principle directions, and h^3 is replaced by ΔV , where $\Delta V = h_x h_y h_z$. In this case, the vorticity associated with an element is $\omega_i = 1/\Delta V \int \omega dx$, the integration is performed over ΔV .

From Helmholtz theorem, the vorticity associated with a material element $\Delta \mathbf{l}_i$ changes as it stretches, $\omega_i(t) = \{\omega_i(0)/\Delta \mathbf{l}_i(0)\} \Delta \mathbf{l}_i(t)$, while $\Delta \mathbf{l} = |\Delta \mathbf{l}|$. Moreover, according to Kelvin theorem, the circulation of the vortex vector element remains constant as it moves along particle paths, while due to incompressibility, ΔV is constant. Thus, Eq. (11) can be written as:

$$\omega(\mathbf{x}, t) = \sum_{i=1}^N \Gamma_i \Delta \mathbf{l}_i(t) f_\delta(\mathbf{x} - \mathbf{x}_i) \quad (13)$$

In this expression, $\Delta \mathbf{l}_i$ is the material vector associated with the vortex vector element, and \mathbf{x}_i is the midpoint of this vector, $\mathbf{x}_i(\mathbf{x}_i, 0) = \mathbf{x}_i$.

The velocity field is obtained by substituting Eq. (9) into Eq. (10) and integrating:

$$\mathbf{u}_\omega = -\frac{1}{4\pi} \sum_{i=1}^N \Gamma_i \frac{(\mathbf{x} - \mathbf{x}_i) \times \Delta \mathbf{l}_i}{r^3} \kappa\left(\frac{r}{\delta}\right) \quad (14)$$

where $\kappa(r) = 4\pi \int f(r') r'^2 dr'$, and $r_i = |\mathbf{x} - \mathbf{x}_i|$, while \mathbf{x}_i is the center of the vortex vector $\Delta \mathbf{l}_i$. In this representation, each vortex vector element is described by $(\Gamma, \mathbf{x}, \Delta \mathbf{l})_i$. Since \mathbf{x} and $\Delta \mathbf{l}$ are the position and length of a material particle and a material line, respectively, their variation with time can be obtained from (Truesdell [21]):

$$\frac{d\mathbf{x}}{dt} = \mathbf{u}(\mathbf{x}(t), t) \quad (15)$$

$$\frac{d\Delta \mathbf{l}}{dt} = \Delta \mathbf{l} \cdot \nabla \mathbf{u} \quad (16)$$

Thus, using a first-order time integration:

$$\mathbf{x}_i(t + \Delta t) = \mathbf{x}_i(t) + \mathbf{u}_i \Delta t \quad (17)$$

and

$$\Delta \mathbf{l}_i(t + \Delta t) = \Delta \mathbf{l}_i(t) + \Delta \mathbf{l}_i(t) \cdot \nabla \mathbf{u}_i \Delta t \quad (18)$$

The velocity gradient can be evaluated analytically by differentiating Eq. (14), as proposed by Anderson and Greengard [22]. However, since the vorticity moves along particle paths, the material line coinciding with the vortex vector $\Delta \mathbf{l}_i$ can be approximated by its terminal points $\mathbf{x}_1' = \mathbf{x}_i + \Delta \mathbf{l}_i/2$ and $\mathbf{x}_2' = \mathbf{x}_i - \Delta \mathbf{l}_i/2$, and

the center of the vortex vector element is approximated by $\mathbf{x} = (\mathbf{x}_1' + \mathbf{x}_2')/2$. In this scheme, a vortex vector element is described by $(\Gamma, \mathbf{x}_1', \mathbf{x}_2')$ and both terminal points are updated each time step. A similar construction was used by Chorin [23,24,25] to study boundary layer stability, the evolution of a turbulent vortex and the properties of developed turbulence. Since the vorticity field is solenoidal, the end of an element is the beginning of the next element if these elements were neighboring elements on the same vortex line at $t = 0$. Thus, this scheme can be used to ensure the satisfaction of the condition $\nabla \cdot \omega = 0$ by maintaining the connectivity of vortex tubes no matter how accurate is the discretization of the vorticity field. The same property is utilized in the filament scheme of Leonard [26] (see also Ashurst and Meiburg [27]). A discussion of the relationship between different algorithms is given by Greengard [28]. In our computations, a second-order time integration algorithm is used to move the terminal points, $(\mathbf{x}_1', \mathbf{x}_2')$, of the vortex vector elements, e.g., for \mathbf{x}_1' :

$$\mathbf{x}_1'^* = \mathbf{x}_1'(t) + \mathbf{u}_i \Delta t \quad (19)$$

and

$$\mathbf{x}_1'(t + \Delta t) = \mathbf{x}_1'(t) + (\mathbf{u}_i + \mathbf{u}_i^*)/2 \Delta t$$

where $\mathbf{u}_i^* = \mathbf{u}(\mathbf{x}_1'^*)$.

The accuracy of the vorticity discretization depends on: the choice of the core function f , the distance between the centers of neighboring elements h , and the ratio between the initial separation between the vorticities and the core radius, δ/h . In the analysis of Beale and Majda [29], it is shown that a second order scheme is obtained if the following third order Gaussian core function is used:

$$f(r) = \frac{3}{4\pi} e^{-r^3} \quad (20)$$

and:

$$\kappa(r) = 1 - e^{-r^3} \quad (21)$$

As the flow develops strong stretch along the vortex lines, the effective value of $\delta \mathbf{l}$ exceeds h and the amount of vorticity transported by each

vortex ball grows. To maintain a uniform resolution, if $\Delta x_1 > 2h$, a vortex element is split into two elements, each with $\Delta x = \Delta x_1/2$ and $\Gamma = \Gamma_1$. Effectively, this amounts to redistributing the vorticity field among a larger number of elements to maintain the accuracy of the calculations. The value of δ is kept constant in our calculations.

II.3. SELF-INDUCED VELOCITY OF A RING

To investigate the effect of discretization of the vorticity field on the accuracy of the calculation of the velocity field, the self-induced velocity of a vortex ring with a radius R and a finite core radius σ is computed and compared with the analytical results for a thin vortex ring. For this purpose, the ring is discretized along its axis into a number N of vortex vector elements, where the length of each element is $h = \Delta x(0) = 2\pi R/N$. Each element is represented by a computational vortex ball with core radius $\delta = \sigma$. This is a worst-case analysis, since normally one would use several elements to represent the core, and choose $\delta < \sigma$ (as will be shown later). However, we start with this case for simplicity and computational convenience.

To distinguish between the two representations of a vortex ring; where the vortex balls are aligned along the ring axis forming a tube of vorticity, is called the thin tube approximation while if several vortex balls are used within the cross section of the ring, it is called a vortex torus. The first approximation is different from the thin filament approximation of Leonard [26]. In the thin filament approximation, the Biot-Savart law is modified to remove the singularity at the center of the filament and the core maintains its vorticity distribution as the filament is deformed. In the thin tube approximation, neighboring elements can move freely with respect to each other, and hence changing the local vorticity distribution of the tube.

In the discretization of the vortex ring using the thin tube approximation, $\delta = \delta h$, where $\delta > 1$ to insure the overlapping between neighboring elements. Eq. (14) is used to evaluate the self-induced velocity V by summing the contribution of the elements around the ring, excluding the effect of the element on itself. Results are compared with the analytical expression of Saffman [13] for a thin vortex ring, $\sigma/R \ll 1$:

$$V = \frac{\Gamma}{4\pi R} \left(\ln \frac{8R}{\sigma} - C \right) \quad (22)$$

where $C = 0.558$ for a second order Gaussian distribution of vorticity within the core and σ is the effective radius, i.e. it is the standard deviation in the Gaussian.

A comparison between our computations of the self-induced velocity and Eq. (22) is shown in Fig. 1 for different values of N , $\bar{V} = V/(\Gamma/4\pi R)$. Three comments should be made here: (1) since the

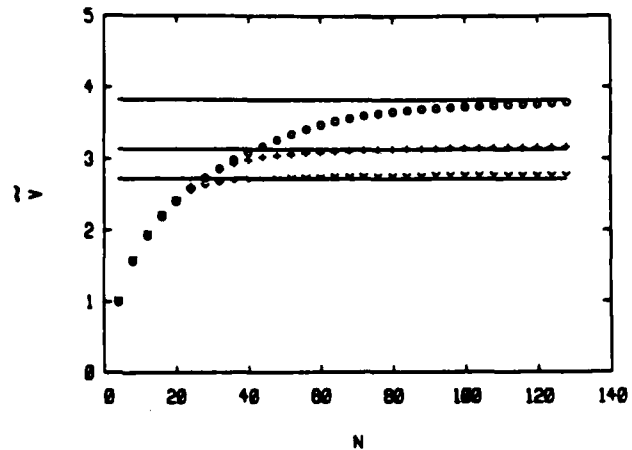


Figure 1. The normalized self-induced velocity of a vortex ring $\bar{V} = V/(\Gamma/4\pi R)$ vs. the number of computational vortex balls used to discretize the ring, N . The analytical results of Saffman is represented by the straight line. $\sigma/R=0.1 \rightarrow \circ$; $\sigma/R=0.2 \rightarrow +$; $\sigma/R=0.3 \rightarrow \Delta$.

core function of the vortex elements is a third order Gaussian, Eq. (18), and not a second order Gaussian as in Saffman's calculations, a slight discrepancy in the self-induced velocity is expected (a comparison between the two distributions is presented in Fig. 2); (2) since $\delta > h$, and a strong overlap between the cores of neighboring elements is ensured, the vorticity at any point is the contribution of many elements

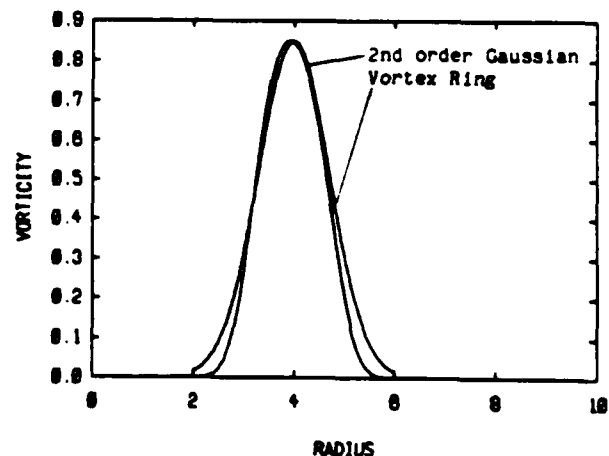


Figure 2. A comparison between the vorticity distribution within the core of the thin ring used in the computations of Fig. 1, i.e. a third order Gaussian described by Eq. (18), and that of Saffman ring, i.e. a second order Gaussian. In both cases, $\sigma/R = 0.25$.

along the ring axis (the vorticity of a single element and the total ring vorticity at any point is presented in Fig. 3, showing that while the

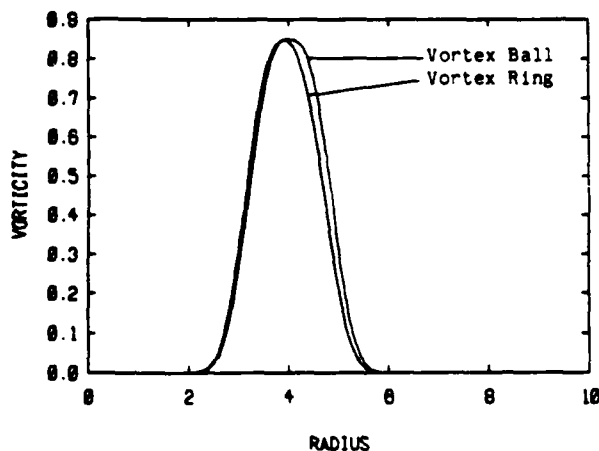


Figure 3. The vorticity distribution of a single vortex ball and the vorticity distribution of a vortex ring, both normalized with respect to their maxima $\sigma = \delta = 0.25 R$.

magnitude is strongly affected by neighboring elements, the core size is the same); and, (3) the analytical expression applies for $\sigma \ll R$, and hence best comparison is expected for $\sigma/R = 0.1$, while it deteriorates for thicker rings.

As the ring becomes thinner, i.e. larger R/σ , more elements are required to achieve an accurate discretization. This is expected, since by choosing $\delta = \sigma$ and $\delta = 8h$, where h is a factor larger than one, the number of elements $N = 2\pi R/(\delta h) = O(R/\sigma)$, which increases as σ decreases. Therefore, for a fixed core size σ , the number of elements required to compute the self-induced velocity due to curvature R grows as R increases.

II.4. STABILITY OF A THIN VORTEX RING

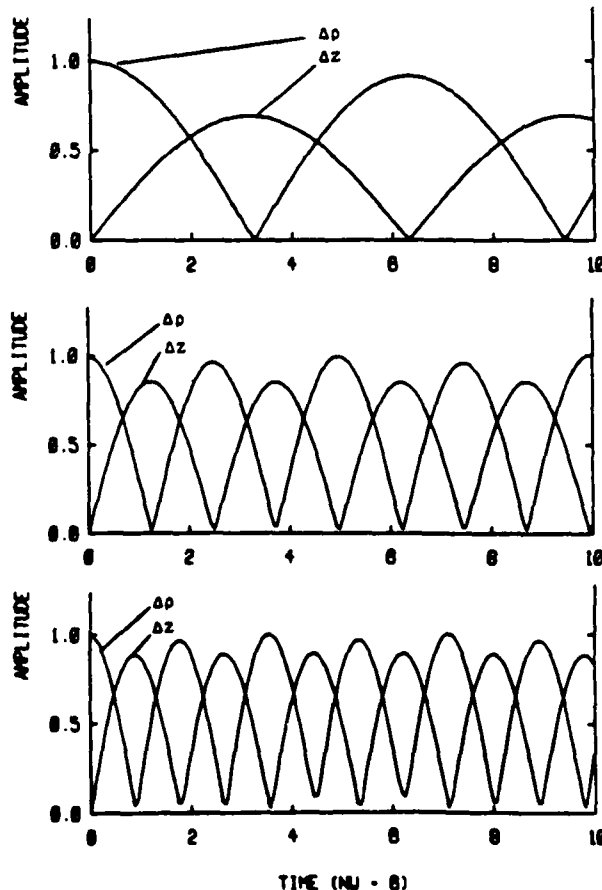
A more interesting problem, providing a test for the accuracy of the time-dependent computations, is the growth of small perturbations on the vortex ring. There is a rigorous asymptotic linear theory for the stability of vortex rings in two forms: (1) for a ring with a non-deformable core, performed by Widnall and Sullivan [14]; and (2) a more elaborate theory for a ring with a deformable core reported in Widnall et al. [15], Widnall [30] and Widnall and Tsai [31]. We will compare the results of the thin tube approximation to the first case, and results for the vortex torus to the second case.

To study the linear stability of thin vortex rings in the thin tube approximation, i.e. with almost non-deformable cores, a radial perturbation of amplitude $\epsilon/R = 0.02$ and a wavenumber n is imposed on the axis of the ring. The wavenumber is defined here as the number of waves that is fitted along the entire length of the ring axis,

thus the size of the perturbation varies in the azimuthal direction as $\Delta p = \epsilon \sin(2\pi n\theta)$. Originally, the ring lies in the $x-y$ plane, and the streamwise is the z -direction while $\rho = R$ for all vortex balls. We start with $n = 1$ and increase by an increment of one. The time step used is $\Delta t = 0.10$. Similar results were obtained for $\sigma/R = 0.1, 0.15, 0.2, 0.25$. In the following, only the first case is discussed in detail.

For $n < n_c$, where n_c is the wavenumber of a

neutrally stable mode that neither rotates around the ring axis nor grows, the waves rotate, or spin, around the ring axis at a frequency Ω that depends on n . As it rotates around the unperturbed axis of the ring, the instantaneous center of the ring draws an ellipse whose major axis is in the radial direction, ρ , and the minor axis is in the streamwise direction z . Thus, these are bending waves that move around the ring axis, hence the name helical waves (if the ring is opened to form a rectilinear vortex, the waves will look like a corkscrew spinning at frequency Ω). The sense of rotations of the waves is the same as that of ring vorticity. The frequency of rotation Ω starts out low at small n , grows to a maximum and then decreases again. The amplitude in the radial ρ -direction and streamwise z -direction are shown in Fig. 4 for $n = 2, 4, 6, 8, 10$ and 12 for



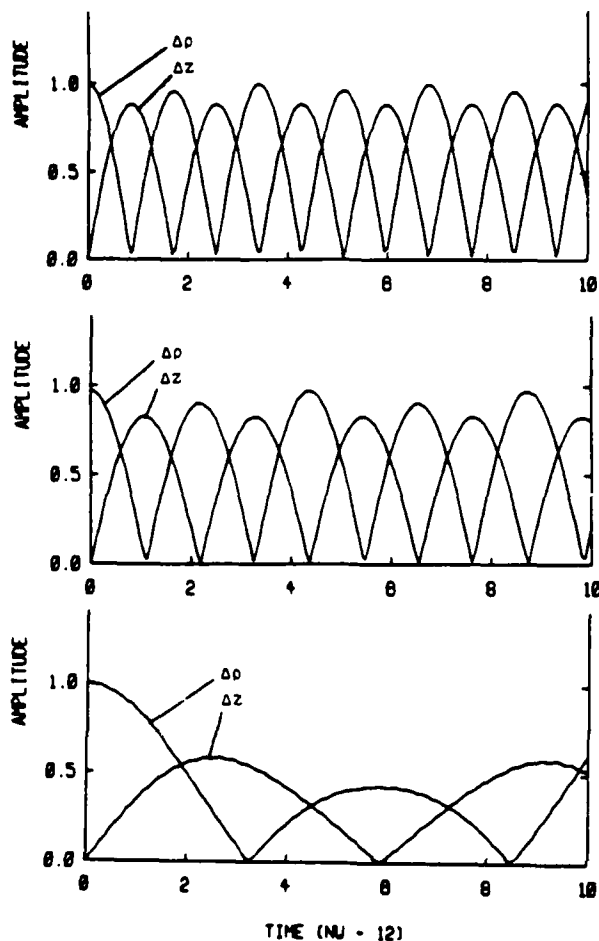


Figure 4. The amplitude of the perturbation in the radial ρ -direction and the streamwise z -direction for a vortex ring with $c/R = 0.1$, computed using the thin tube approximation. The wavenumber of the perturbation is $n = 2, 4, 6, 8, 10$ and 12 , arranged from the top figure. Both amplitudes are normalized with respect to the initial perturbation in the radial direction, $c/R 0.02$,

and time is normalized with respect to R^2/Γ . In this figure, the behavior of the modes $n < n^*$ is shown.

$c/R = 0.1$. Note that the radial perturbation produces a streamwise perturbation of almost the same magnitude. All these modes are characterized as being linearly stable since their amplitudes remain bounded.

At $n = n_n$, the waves neither grow nor rotate. For $c/R = 0.1$, at $n_n = 13$ the ring remains in its original plane without bending, as depicted by Fig. 5. The next mode, $n^* = 14$, the waves grow in the radial direction, and then in the streamwise direction so that the total amplitude grows exponentially in time, i.e. the ring becomes linearly unstable and streamwise vorticity is

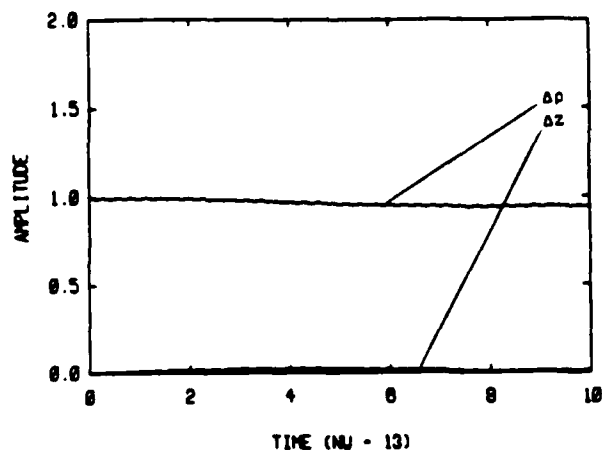


Figure 5. The amplitude of the perturbation in the radial and streamwise directions for the neutrally stable mode for the same ring as in Fig. 4.

produced. Moreover, no wave rotation is observed. The wave amplitudes are shown in Fig. 6 for $c/R = 0.1$.

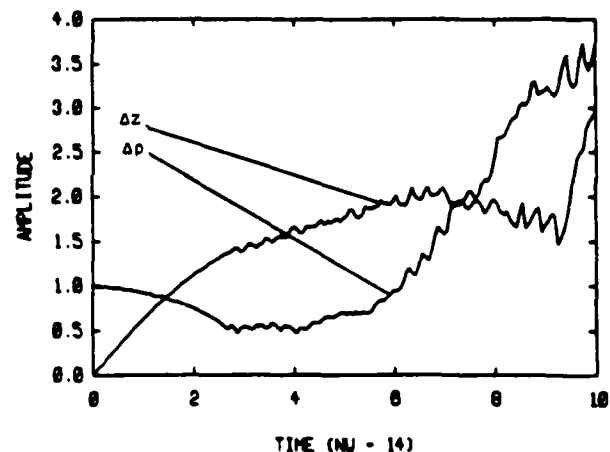


Figure 6. The amplitude of the perturbation in the radial and streamwise directions for the unstable mode n^* of the ring of Fig. 4.

As $n > n^*$, the ring is stabilized again and the eigenfunctions behave in a similar way to $n < n_n$. However, the major axis of the ellipse is now in the streamwise direction and the frequency of rotation increases indefinitely. Moreover, the sense of rotation is in the opposite to that of the ring vorticity. The wave amplitudes in the ρ and z directions are shown in Fig. 7 for $n = 15, 17$ and 19 .

Similar observations are made for $c/R = 0.15, 0.2$ and 0.25 . In all cases, the unstable mode n^* is a bifurcation in the eigenfunction that corresponds to $\Omega = 0$. In Fig. 8, the results of

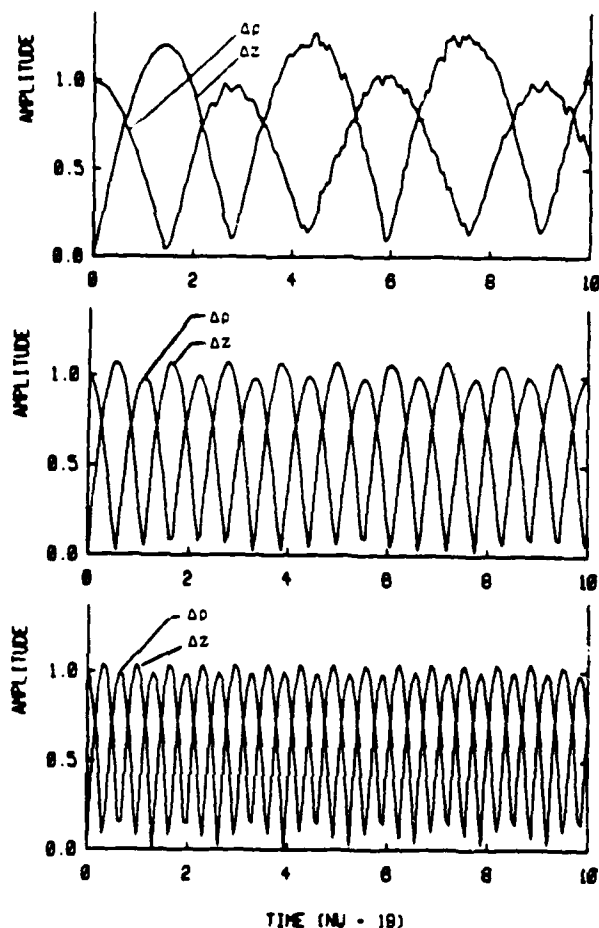


Figure 7. The amplitude of the perturbation in the radial and streamwise directions for the modes $n > n^*$ of the ring described in Figure 4. The wavenumber of the perturbation is $n = 15, 17$, and 19 , arranged from the top.

these computations are summarized in terms of Ω , the rotation frequency of the waves, v.s. the wave number $k = n\sigma/R$. In this figure, Ω is normalized with respect to Γ/R^2 . In all cases, the unstable mode $k^* = n^*\sigma/R = 1.25$ corresponds to a non-rotating mode, $\Omega = 0$. This is in agreement with the theoretical results of Widnall and Sullivan [14]. They observed, similar to what we see in the numerical results, that a mode becomes unstable when the self-induced rotation of the waves balances the rotation induced by the rest of the ring and the energy of the perturbation is utilized in stretching the wave amplitude.

In order to check on the accuracy of the computations, we varied the discretization parameter h by using more elements around the axis of the ring, $h = 2\pi/RN$. Figure 9 shows the growth of the amplitude of the perturbation with time using an increasing number of elements for $\sigma/R =$

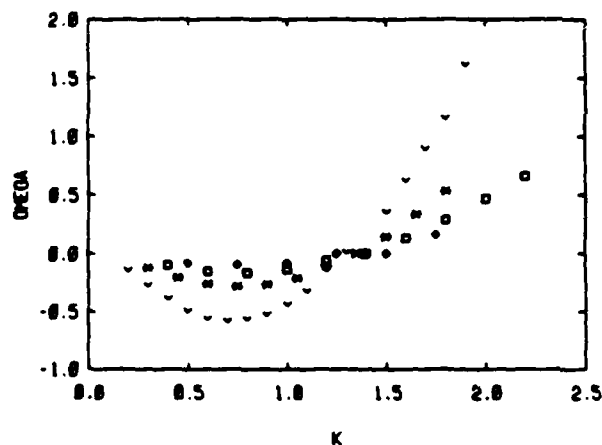


Figure 8. The computed results for the dispersion relation of a ring using the thin tube approximation. $\sigma/R=0.1 \rightarrow \circ$; $\sigma/R=0.15 \rightarrow \square$; $\sigma/R=0.2 \rightarrow \triangle$; $\sigma/R=0.25 \rightarrow \diamond$. The frequency of rotation of the mode Ω is normalized with respect to R^2/Γ while k is normalized with respect to R/σ .

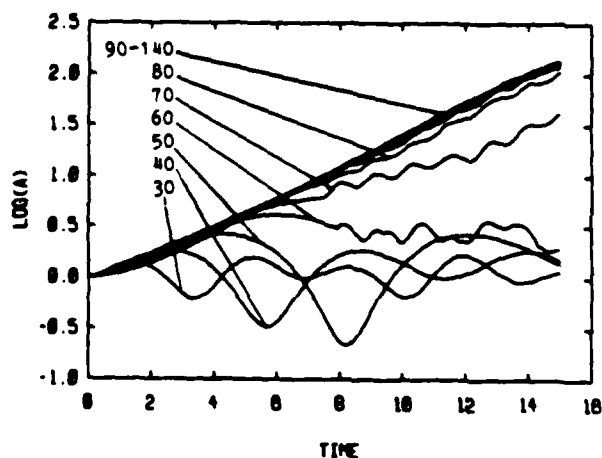


Figure 9. The growth of the unstable mode $n^* = 7$ for $\sigma/R = 0.1$, computed using $N = 30-140$, with increments $\Delta N = 10$.

0.2 and $n = n^* = 7$. $N = 30$ is the smallest number necessary to satisfy the condition $\delta \geq h$, however, we notice that $N = 90$ is necessary to compute the logarithmic growth rate accurately. It is the same number required to compute $\bar{V} = 3.1309$ accurately, as seen in Fig. 2. This is not surprising since the stability of the local waves depends strongly on the velocity (or strain field) induced by the ring on the perturbation. The linear growth rate, $\alpha_x = d(\log A)/dt = 0.1625$. The analytical value obtained by Widnall and Sullivan [14] for the same value of \bar{V} is $\alpha_x = 0.157$.

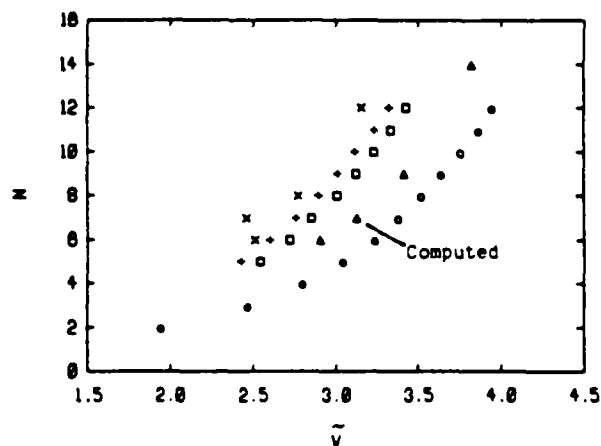


Figure 10. The computed wavenumber of the most unstable mode vs. the normalized self-induced velocity \bar{V} , compared with the results of the linear asymptotic theory for a non-deformable core approximation \circ , the results of the theory for a deformable core for a uniform vorticity distribution \square , and for a quadratic distribution \triangle , and the experimental results of Widnall et al. \times .

In Figure 10, we plot the critical wave number n^* against the self-induced velocity \bar{V} , used to characterize the ring, for the four cases. On the same plane we reproduce the results of Widnall et al. [15] and Widnall and Tsai [31] for the non-deformable core model, the deformable core model and their experimental results. The comparison is interesting and proves our early speculation that the numerical thin tube model allows small core deformation since the computational results are closer to the experimental data than those of the analytical solution of the non-deformable core model. However, it does not allow enough changes within the core to capture higher order radial variations within the core which support the short wave instability that is observed experimentally.

So far, it can be concluded that although the results of the thin tube approximation are in agreement with the analytical theory of a vortex ring with a non-deformable core, the model is not capable of describing the stability characteristics of a vortex ring with deformable finite core, as observed experimentally. Using vortex balls allows, however, small first order deformations in the vorticity core of the ring, as shown in Fig. 11, which move the predictions of the unstable modes closer to the experimental values than the analytical theory of non-deformable core but not as close as the results of the more elaborate theory of deformable cores. Thus we must proceed to a more detailed description of the vorticity core of the ring using several vortex balls to discretize the vorticity within the core, as we will show next.

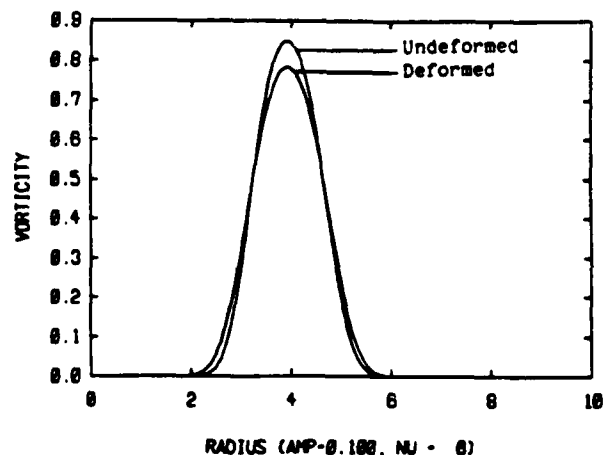


Figure 11. A comparison between the vorticity distribution within the vortex ring before deformation and after deformation of amplitude $\epsilon/R = 0.1$ and $n_w = 6$ for $\epsilon/R = 0.25$, computed at point of zero deformation.

11.5. STABILITY OF A VORTEX TORUS

To make the distinction between the two models of the vortex ring clear, this ring is called a vortex torus. In this representation, the core of the vortex torus is discretized into more than one vortex ball so that $\delta < a$. Thus, the vortex torus is formed of a number of vortex rings whose cores are smaller than the core of the torus. The initial vorticity $\omega_i(0)$ associated

with each vortex ball is computed from Eq. (12) by solving the corresponding system of linear equations, subject to the condition that the total circulation is the same. Since the torus is uniform in the azimuthal direction, it suffices to solve a number of equations equal to the number of balls used across one cross-section of the ring.

In the results presented here, nine balls were used across each section of the ring, one at the center and eight distributed along the circumference of a circle with radius $\rho = 0.74a$, arranged at 45° . This choice for the initial location of the centers of the vortex balls is used to minimize the difference between the total circulation of the vortex torus and the sum of the circulation of the vortex balls. The core radius of each ball was taken as $\delta = 0.8a$, and the distance between the centers of neighboring elements is $h = \delta/1.1$. Therefore, the number of elements used along the circumference of the torus depends on its radius. Figure 12 show the actual vorticity distribution and the numerical vorticity distribution produced by the vortex balls. The motion of these balls throughout the cross section of the torus allows a substantial deformation of its core at different sections. Thus, higher-order radial modes associated with the instability of vortex rings, which has been observed experimentally and analytically, can be captured.

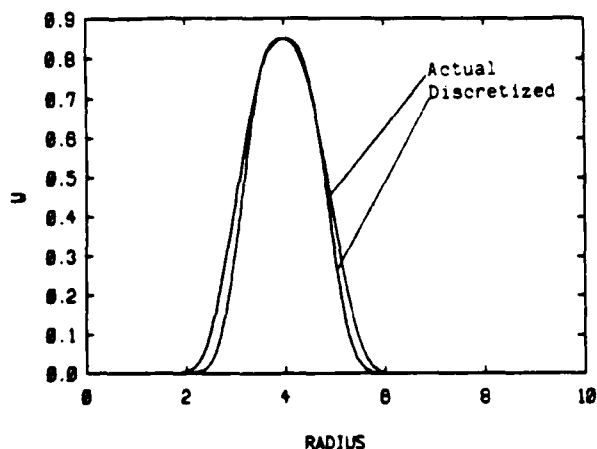


Figure 12. The actual and discretized vorticity distribution of a vortex torus using nine vortex balls within the core.

Computations were performed for four tori with $a/R = 0.15, 0.20, 0.25,$ and 0.35 . In all cases, the vorticity distribution is the same third-order Gaussian utilized before. The initial amplitude of the perturbation $\epsilon/R = 0.02$, and a number n of sinewaves were fitted along the torus to model the initial perturbation. The time step of integration $\Delta t = 0.1$, and the computations were performed for 1000, or 2000 time steps to observe the growth of the perturbation. The overall behavior of the vortex torus was the same in all cases. As an example, results for $a/R = 0.2$ are discussed next in detail.

Figure 13 shows two views of the torus after 1000 time steps, when perturbed with $n = 8, 9, 10,$ and 11 . In the first three cases, the core deforms, as seen by the redistribution of the individual rings within the torus, and the waves spin around the unperturbed axis of the ring. However, the perturbation stays bounded. In the last case, the perturbation grows in both the radial and the streamwise directions causing substantial non-uniform deformation around the ring axis, and the generation of streamwise vorticity. The amount of deformation in each case is seen from the total number of elements used at the last time step. In the first three cases, the number of elements remains constant at $N = 1080$ for 1000 steps. In the unstable case, the number of elements grows to 1262. Since from Helmholtz theorem, $\omega(t)/\omega(0) = \Delta l(t)/\Delta l(0)$, where Δl_i is the summation over Δx_i for all the vortex elements,

this stretch is accompanied by intensification of the vorticity within the ring at the same ratio of stretch.

Figure 14 shows two views for the torus in the unstable case every 200 computational time steps, starting at $t = 0$. It is clear that, at the unstable mode, waves do not rotate around the axis of the ring while their amplitudes grow,

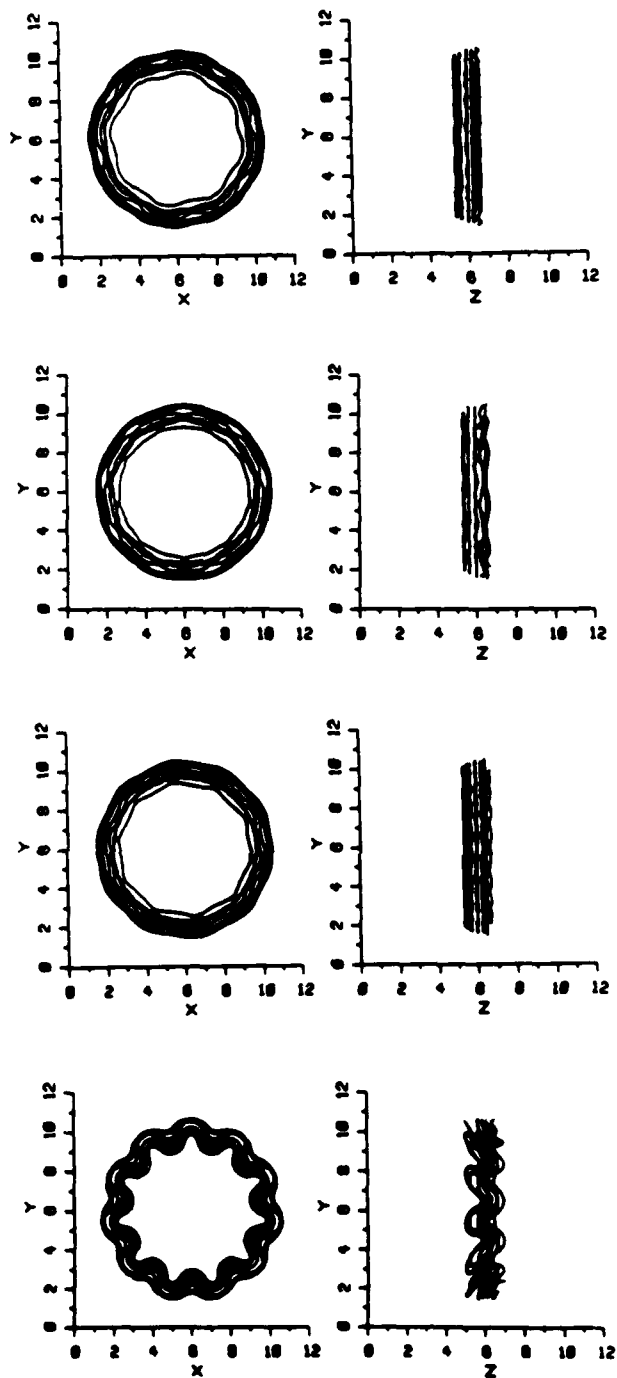


Figure 13. The form of the vortex torus, $a/R = 0.2$, after 1000 computational time steps with $\Delta t = 0.1$, starting with a perturbation of $\epsilon/R = 0.02$. The wavenumber of the perturbation is $n = 8, 9, 10,$ and 11 , starting from the top plot.

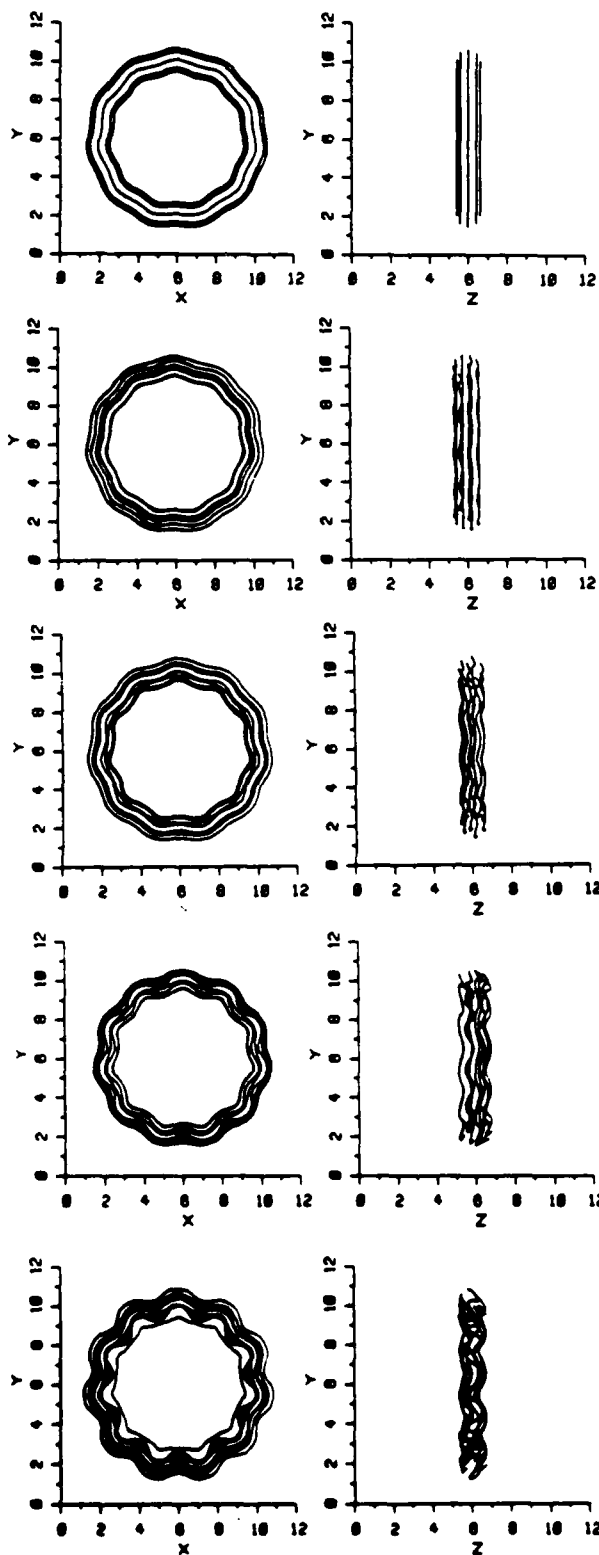


Figure 14. The growth of the perturbation on a vortex torus with $a/R = 0.2$, $c/R = 0.02$ and $n = 11$. The torus is discretized into 9 rings with 120 vortex balls along each ring. Results are shown every 200 time steps starting with $t = 0$. The plots show that this is an unstable mode in which the amplitude of the waves grow without rotation.

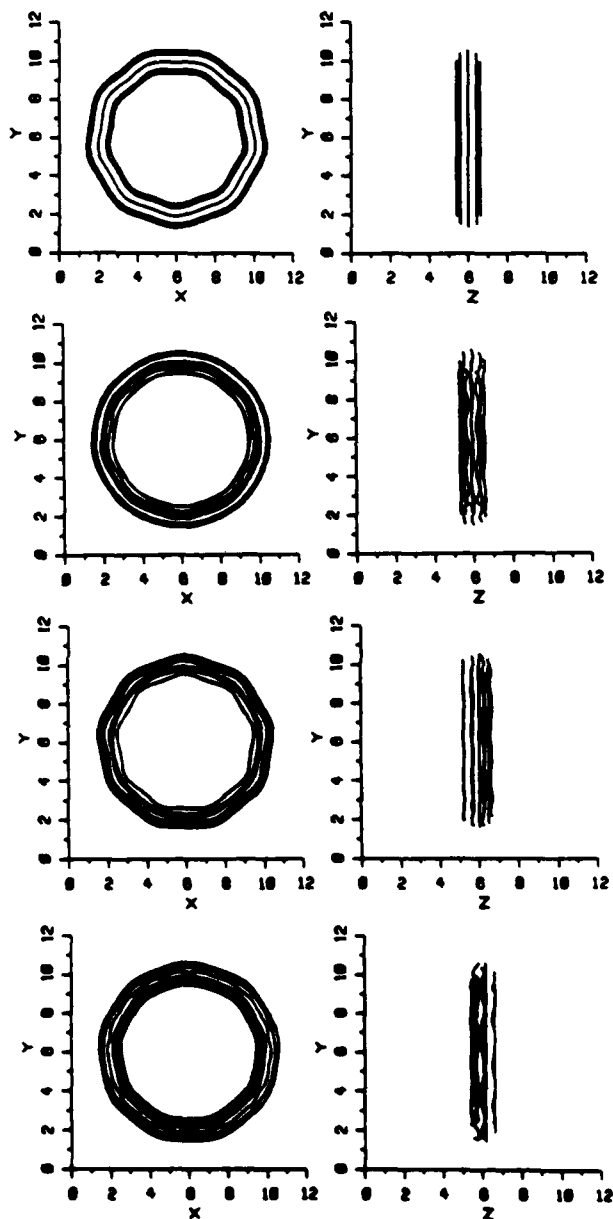


Figure 15. The same vortex ring as in Fig. 14 but with $n = 9$. The plots indicate that this is a stable mode without growth, while the waves rotate around the unperturbed center of the ring. The ring is plotted every 300 steps starting at $t = 0$.

similar to the results of the thin tube approximation and to the results of Widnall and Tsai [31]. Moreover, the core vorticity is redistributed into a number of sectors equal to the number of waves. The outer portion of each sector stretches forward in the streamwise direction while the inner part elongates backwards. On the other hand, results for $n = 9$, which is a stable mode, depicted every 300 steps in Fig. 15, show the rotations of the waves as peaks and valleys exchange their locations while the core vorticity remains uniform in the azimuthal direction.

The average amplitude of the perturbation around the circumference of a torus with $a/R = 0.15$ and 0.35 is shown in Figs. 16 and 17,

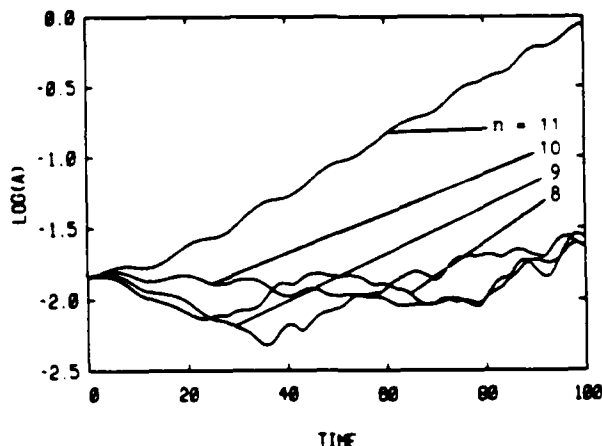


Figure 16. The growth of the perturbation with time for a torus with $a/R = 0.2$, perturbed with $n = 8, 9, 10$, and 11 .

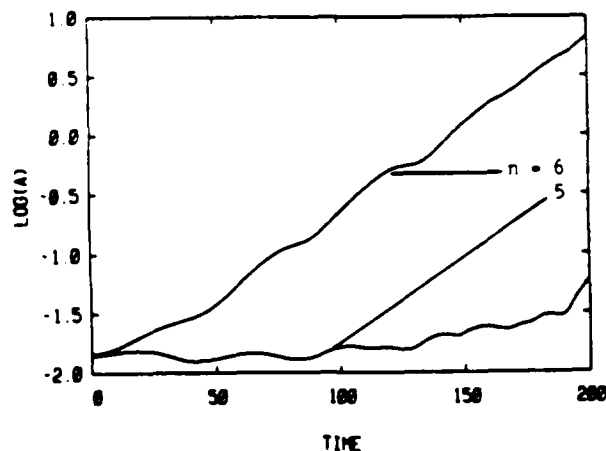


Figure 17. The growth of the perturbation with time for a torus with $a/R = 0.35$, perturbed with $n = 5, 6$.

respectively. The exponential growth of small perturbations at the early stages is seen at $n = 11$ and 6 for the two cases, respectively. Figure 18 summarizes the results for the four tori, $a/R = 0.15, 0.2, 0.25$ and 0.35 , showing a very good agreement with the experimental results of Widnall and Sullivan [14]. As before, the value

of V is used to characterize the ring in order to remove any confusion about the definition of the core and the vorticity distribution. The analytical results for a vortex torus with a non-uniform vorticity distribution within the core, the numerical results, and the experimental data are in close agreement, differences can be primarily attributed to the vorticity distribution within the core.

The form of the unstable torus with $a/R = 0.35$ at $n = 6$, is shown at time steps 1400-2000, every 200 steps in Fig. 19 (it was found that $n = 7$ is also an unstable mode for this torus). It is interesting to note that the core deformation is different at different azimuthal locations and that the inner and outer radii do not follow the same pattern (Yule [32]). The figures indicate that the inner and outer edges of the vorticity core of the torus may move in anti-phase and that variations at frequencies different than the perturbation frequency arise at late times. Thus, higher order radial modes form as part of the instability of vortex rings, in accordance with the conclusion of the analytical theory [15]. To quantify these frequencies, we study the energy spectra of two tori. In Figs. 20 and 21, the spectra for $a/R = 0.20$ at $t = 100$ and for $a/R = 0.35$ at $t = 200$ are shown. In the stable modes, only the perturbation frequency is present at very small amplitude. In the unstable modes, higher harmonics of the perturbation frequency, which had zero amplitudes at $t = 0$ are excited at substantial levels.

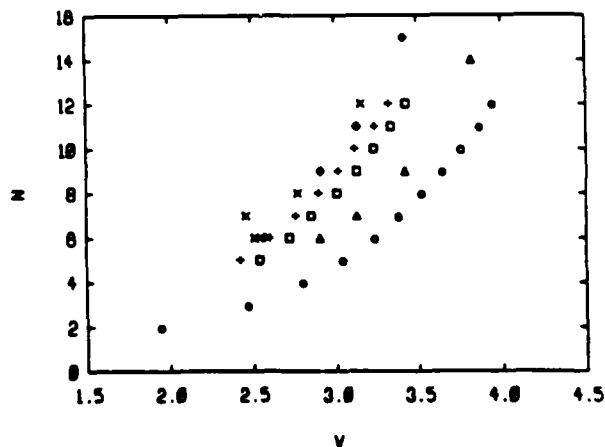


Figure 18. Comparison between the experimental data, x , of Widnall et al. [15] and of the numerical predictions, o , of the unstable modes of a vortex torus. The plots include data from Fig. 10.

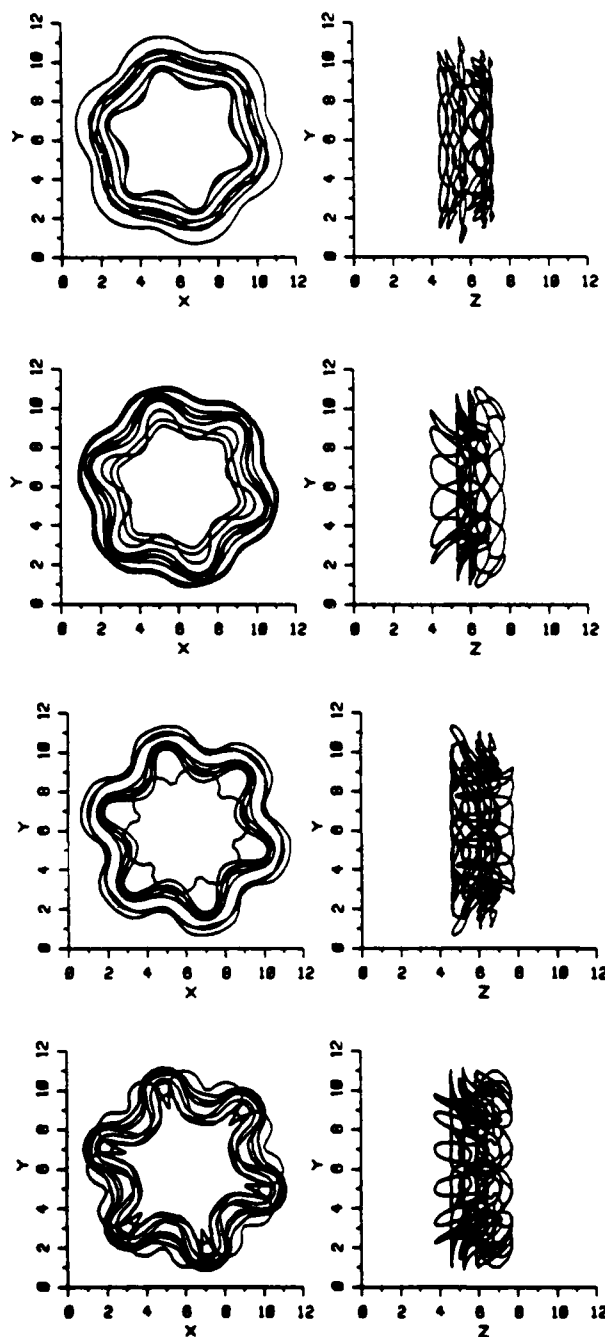


Figure 19. The evolution of the unstable mode of a vortex torus with $a/R = 0.35$, perturbed at $t = 0$ with $c/R = 0.02$ and $n = 6$. The torus is shown at time steps 1400-200, every 200. The total number of vortex elements at these plots is 810 (as at $t = 0$), 822, 870 and 1032, respectively.

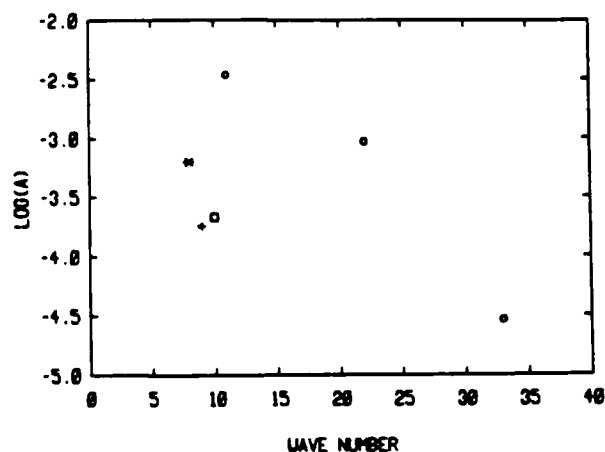


Figure 20. The frequency spectra for the energy of a torus with $a/R = 0.2$ measured at $t = 100$, for $n = 8 + *$; $n = 9 + \square$; $n = 10 + +$; and $n = 11 + o$. In the unstable mode, higher harmonics at 22 and 33 are excited.

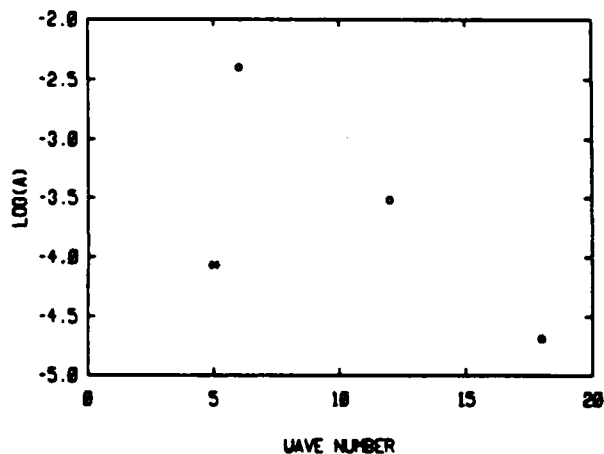


Figure 21. The frequency spectra for the energy of a torus with $a/R = 0.35$, measured at $t = 200$, for $n = 5 + *$ and $n = 6 + o$.

Results of this section indicate that the numerical simulation of vortex rings with finite and deformable cores, as represented by a number of vortex balls distributed within the ring core and along its axis, can accurately be used to compute the wavenumber of the unstable modes and their growth. The deformation of the ring into a number of sectors aligned with the unstable standing waves resembles strongly the experimental results. The generation of small scales, accompanied by higher frequencies in the energy spectrum, is due to vortex stretch and leads to the well-known turbulence cascade. Thus, the azimuthal instability of vortex ring may be one mechanism of transition to turbulence.

III AXISYMMETRIC SHEAR LAYER

The ultimate goal of this work is to study, using three dimensional vortex simulation, the evolution of a turbulent axisymmetric shear layer. Analytical and experimental studies of this configuration indicate that several types of instability can arise and influence the development of the flow field (e.g. Yule [32], Crow and Champagne [33] and Michalke and Hermann [34].) These instabilities include axisymmetric modes, such as the rollup and pairing of ring-like vortex eddies, and the jet-preferred mode, as well as azimuthal modes such as the type which was analyzed in the previous section. The interaction between these modes, which have not been fully understood, govern the flow, and in particular, the velocity fluctuations, entrainment, and mixing between the fluids on both sides of the layer. Chemical reactions, sound generation, combustion instability can be strongly affected by these interactions.

In this section, results for the evolution of an axisymmetric shear layer, subject to an axisymmetric perturbation, and using the three-dimensional vortex scheme developed in the previous section, are presented. The computations are restricted to a periodically excited layer, thus boundary conditions on both sides of the computational domain, i.e. the wavelength, are satisfied. This is accomplished by using image vortices on both sides of the domain and computing their field by summing over the induced velocity of these images. The first image of each vortex on both sides must be considered as a vortex ball with a finite core radius. Beyond that, images can be considered as vortex points with zero cores. The effect of the latter can be arranged as a summation over an infinite series for a two-parameter function. This function is computed, using a large number of terms in the series, and stored as a two-dimensional table of the two parameters. During the computations, an interpolation procedure is used to obtain the value of the function at intermediate points. Details will be published elsewhere.

Results are obtained for an axisymmetric shear layer with the following parameters: the thickness of the vorticity layer $L/D = 0.2$, wavelength of the perturbation $\lambda/D = 1.32$, and amplitude of perturbation $\epsilon/D = 0.04$, where $L = 2\sigma$ and σ is the standard deviation of the second-order Gaussian vorticity distribution within the layer and D is the mean diameter of the layer. The layer is discretized into 16 sections in the streamwise directions and 5 sections in the cross-stream direction, resulting in 80 vortex rings. Each ring is represented by 50 vortex balls along its axis. The vorticity of each vortex ball was obtained as before using $\delta/D = 0.0825$. Figure 22 shows a comparison between the actual and discretized vorticity distribution.

Figure 23 shows the location of the vortex elements in ρ - z plane, where ρ is the radial direction and z is the streamwise direction, and their streamwise velocity relative to the mean flow. In Fig. 24, vortex balls which were

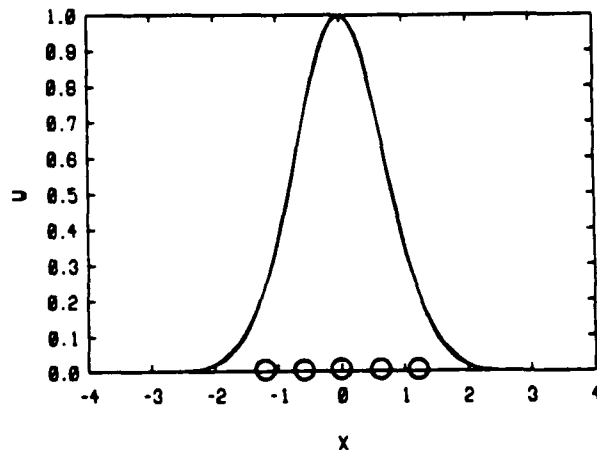


Figure 22. Actual and discretized vorticity within the shear layer. Five vortex balls are used at the indicated location.

neighbors in the z -direction at time $t = 0$ are connected using cubic spline curves to show the stretch that the flow experiences while vorticity is during the rollup phase. The vorticity field and the material lines are plotted every 20 computational time steps starting at $t = 0$. Although five layers of vortex elements were used to discretize the vorticity in the radial direction, the plots in Fig. 24 show only two layers, the central layer and the next layer to the outside. Plots of vortex elements locations in the radial plane and the ρ - z plane show that the elements remain on perfect circles while the radii of these circles increase or decrease as the vorticity layer rolls up.

Results in Fig. 23 indicate that the initial perturbation causes the layer to rollup, forming a large scale ring-like vortex eddy. As time progresses, more of the vorticity becomes concentrated around this eddy, and more irrotational fluid from both streams is entrained into its core. Due to the self-induced velocity of curved vortex lines, the eddy moves in the streamwise direction. However, within the duration of the computation, it maintains perfect azimuthal symmetry. Figure 24 shows that the central layer experiences the strongest stretch within the core as it endures several turns due to secondary instabilities, while the "braids", i.e. the two sleeves connecting neighboring cores, become thinner due to the strain field of the cores.

Since the layer maintains a perfect axisymmetric configuration during rollup, one can make a preliminary conclusion that the growth of the axisymmetric modes during the early stages of development suppresses the azimuthal instability modes of the evolving vortex-ring eddy. This is widely supported by the analytical linear theory of Michalke and Hermann [35] and by the experimental results of Vandsburger et al. [16], Roquemore et al. [17] and Namazian et al. [35]. The analytical study shows that the exponential

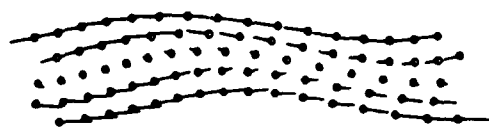


Figure 23



Figure 23

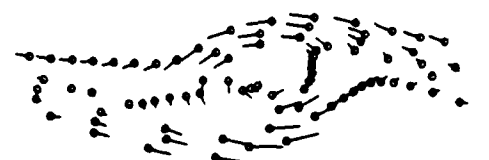


Figure 23



Figure 23

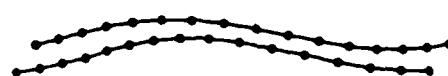


Figure 24



Figure 24



Figure 24



Figure 24

Figure 23. Rollup of an axisymmetric shear layer due to an axisymmetric perturbation. Vortex balls are represented by circles and their velocity relative to the mean velocity is depicted by a line vector starting at the center of the circle. Results are plotted every 20 time steps starting at $t = 2.0$. The solid line indicates the centerline of the layer.

Figure 24. Lines connecting neighboring vortex balls in the streamwise direction. The figure shows the central layer and the next layer to the outside. The solid line indicates the centerline of the layer.

growth rates of axisymmetric modes are higher than those of azimuthal modes. Moreover, in all the reported experimental results, including those of Yule [32] and Crow and Champagne [33], the layer starts by rolling up into a perfect vortex ring. At later stages, the rings become susceptible to the azimuthal instability discussed in the previous section and the flow loses the azimuthal coherence.

However, this is only a preliminary conclusion since, in the numerical solution, the flow started with a large axisymmetric perturbation and zero azimuthal perturbation. The amplitudes of the perturbations were selected to model most experimental situations, where azimuthal perturbations are inhibited at the onset of the layer by the nozzle. The higher growth rate of the axisymmetric mode could also be a property of the linear range, as shown by the analytical results. To support this result and to study the effect of the azimuthal modes on the growth of the axisymmetric modes, we are planning to run the same case for different ratios of the axisymmetric/azimuthal amplitudes. Another issue to be investigated is at what stage does the azimuthal modes start to grow and what effect does the strain field generated during pairing have on its development.

Apart from the displacement of the ring eddy in the streamwise direction due to the curvature of the vortex lines, this eddy resembles the eddy that forms during the rollup of the planar shear layer (Ghoniem et al. [36]). This similarity has been observed before in the two-dimensional calculations of Davis and Moore [37]. As Fig. 24 indicates, the streamwise strain field, associated with the non-linear stages of rollup, pulls the vortex elements apart so that the distance between the neighboring centers exceeds h by a large factor. In order to maintain the resolution at later times, the vorticity field must be redistributed between a different set of elements which are organized so that they can accommodate this strain field, as suggested by Ghoniem et al. [36] in the 2D vortex element method.

The stability of this ring eddy, which has an elliptical core, to azimuthal perturbations while it is moving in the strain field of its neighboring eddies is of central importance to the later stages of development of the layer. A numerical study of this problem is underway.

IV CONCLUSIONS

In this work, we have embarked on the task of applying three dimensional vortex methods for the numerical solution of the unsteady Navier-Stokes equations at high Reynolds number. The 3D vortex element method presented here combines the advantages of the vortex filament method of Leonard [8,11], and the vortex stick method of Chorin [23,23] in maintaining the connectivity of the vorticity field, thus satisfying the solenoidality condition. It utilizes the results of the convergence analysis of Beale and Majda [19,20] in selecting the core of the vortex elements. The scheme is Lagrangian, is capable of capturing the effect of plain strain as well as the vortex stretching along vortex lines by changing the number and strength of the vortex elements. It is readily extendable to flow fields with boundaries.

Results for the stability of a vortex ring with a finite core, which forms as an axisymmetric vorticity layer rolls up, show very good agreement with the analytical and experimental results. The results reveal: (1) the breakdown of the azimuthal coherence of the ring due to the growth of radial perturbations along and within the core; (2) the evolution of streamwise vorticity in the non-linear stages of instability in the form of elongated lobes of vorticity along wedges within the expanding core; and (3) the development of an energy cascade to small scales which accompanies the stretch of vorticity during the non-linear growth of instability. Similar configurations were captured in experimental studies on vortex rings and later stages of turbulent jets.

The scheme was used to investigate the initial stages of transition to turbulence in an excited axisymmetric mixing layer, and the results showed good agreement with the recent qualitative results of Vandsburger et al. [16] and Roquemore et al. [17]. Quantitative study will be performed to investigate the interaction between the axisymmetric and the azimuthal instability modes and their effect on the development of the flow.

ACKNOWLEDGEMENT

This work is supported by the Air Force Office of Scientific Research Grant AFOSR 84-0356, The National Science Foundation Grant CPE-840481 and the Department of Energy Contract DE-AC04-86AL16310. Computer support is provided by grants from NSF and the John von Neumann Computer Center.

REFERENCES

1. Van Dyke, M., An Album of Fluid Motion, Parabolic, 176 p., 1982.
2. Lugt, H.J., Vortex Flow in Nature and Technology, Wiley, 297 p., 1983.
3. Ho, C.-M., and Huerre, P., "Perturbed free shear layers", Ann. Rev. Fluid Mech., **16**, pp. 365-424 (1984).
4. Robert, R.A. and Roshko, A., "Effects of periodic forcing on mixing in turbulent shear layers and wakes, AIAA-85-0570.
5. Ghoniem, A.F. and Ng, K.K., "Numerical study of a forced shear layer", Phys. Fluids, 1987, in press, AIAA-86-0370.
6. Chorin, A.J., "Numerical study of slightly viscous flow," J. Fluid Mech., **57**, pp. 423-442 (1973).
7. Saffman, P.G. and Merion, D.I., "Difficulties with three-dimensional weak solutions for inviscid incompressible flow", Phys. Fluids, **29**, pp. 2373-2375 (1986).
8. Leonard, A., "Computing three dimensional incompressible flows with vortex elements", Ann. Rev. Fluid Mech., **17**, pp. 525-559 (1975).
9. Ashurst, W.T., "Numerical simulation of turbulent mixing layers via vortex dynamics, Proc. the 21st Sym. Turbulent Shear flow, p. 402, Springer-Verlag, 1979.
10. Ghoniem, A.F. and Sethian, J.A. "Effect of Reynolds number on the structure of recirculating flow", AIAA J. 1987, in press. AIAA-85-0146.
11. Leonard, A., "Vortex methods for flow simulation", J. Comput. Phys., **37**, pp. 289-335 (1980).
12. Saffman, P.G., and Baker, G.R., "Vortex interactions", Ann. Rev. Fluid Mech., **11**, pp. 95-122 (1979).
13. Saffman, P.G., "The velocity of viscous vortex rings", Stud. Appl. Math., **49**, pp. 371-380 (1970).
14. Widnall, S.E. and Sullivan, "On the stability of vortex rings", Proc. R. Soc. Lond., **A 332**, pp. 335-353 (1973).
15. Widnall, S.E., Bliss, D.B. and Tsai, C.-Y., "The instability of short waves on a vortex ring", J. Fluid Mech., **60**, pp. 35-47 (1974).
16. Vandsburger, M. Lewis, G., Seitzman, J.M., Allen, M.G., Bowman, C.T. and Hanson, R.K., "Flame-flow structure in an acoustically driven jet flame", Western States Section/The Combustion Institute, 1986 Fall meeting, Paper 86-19.
17. Roquemore, W.M., Bradley, R.P., Jackson, T.A., Kizirnis, S.W., Gross, L.P., Switzer, G.L., Trump, D.D., Sarka, B., Ballal, D.R., Lightman, A.J., Yaney, P.P. and Chen, T.H., "Development of Laser diagnostics for combustion research", Central States Section/The Combustion Institute, 1986 Spring Meeting.
18. Batchelor, G.K., An Introduction to Fluid Dynamics, Cambridge University Press, 615 p. 1967.
19. Beale, J.T. and Majda, A., "Vortex methods I: Convergence in three dimensions", Math. Comput., **39**, pp. 1-27 (1982).
20. Beale, J.T. and Majda, "Vortex methods II: Higher order accuracy in two and three dimensions, Math. Comput., **39**, pp. 29-52 (1982).
21. Truesdell, C., The Kinematics of Vorticity, Indiana University Press, 232 p., 1954.
22. Anderson, C. and Greengard, C., "On vortex methods", SIAM J. Numer. Anal., **22**, pp. 413-440 (1985).
23. Chorin, A.J., "Vortex models and boundary layer instability SIAM J. Sci. State. Comput., **1**, pp. 1-21 (1980).
24. Chorin, A.J., "Estimates of intermittency, spectra and blow-up in developed turbulence, Commun. Pure Appl. Math., **34**, pp. 853-866 (1981).
25. Chorin, A.J., "The evolution of a turbulent vortex", Commun. Math. Phys., **83**, pp. 517-535 (1982).
26. Leonard, A., "Numerical simulation of interacting, three dimensional vortex filaments", Proc. of the 4th Int. Conf. Numer. Meth. Fluid Dyn., pp. 245-50, Springer-Verlag (1975).
27. Ashurst, W.T. and Meiburg, E., "Three dimensional shear layers via vortex dynamics", Sandia National Laboratory report, SAND85-8777, 1985.
28. Greengard, C., Three Dimensional Vortex Methods, Ph.D. thesis, University of California, Berkeley, 1984.

29. Beale, J.T. and Majda, "Vortex methods II: Higher order accurate vortex methods with explicit velocity kernels", J. Comput. Phys., 58, pp. 189-208 (1985).
30. Widnall, S.E., "The structure and dynamics of vortex filaments," Ann. Rev. Fluid Mech., pp. 141-165 (1976).
31. Widnall, S.E. and Tsai, C.-Y., "The instability of the thin vortex ring of constant vorticity", Philos. Trans. R. Soc. Lond. Ser. A, 287, pp. 273-305 (1977).
32. Yule, A.J., "Large-scale structures in the mixing layer of a round jet", J. Fluid Mech., 89, pp. 413-432 (1978).
33. Crow, S.C. and Champagne, F.H., "Orderly structure in jet turbulence", J. Fluid Mech., 48, pp. 547-591 (1971).
34. Michalke, A. and Hermann, G., "On the inviscid instability of a circular jet with external flow", J. Fluid Mech., 114, pp. 343-359 (1982).
35. Namazian, M., Kelly, J., Schaefer, R., Johnston, S. and Long, M., "Flow and mixing structures in bluff-body stabilized gas flames", 1986 International Gas Research Conference, Toronto, Canada.
36. Ghoniem, A.F., Heidarinejad, G. and Krishnan, A., "Vortex element simulation of the rollup and mixing in a thermally-stratified shear layer", submitted for publication, J. Comput. Phys., 1987.
37. Davis, R.W. and Moore, E.F., "A numerical study of vortex merging in mixing layers", Phys. Fluids, 28, pp. 1626-1635 (1985).

TECHNICAL INFORMATION DIVISION
 AFSC
 190 12

END
DATE
FILM
4-88
DTIC